universität wien

DISSERTATION / DOCTORAL THESIS

Titel der Dissertation /Title of the Doctoral Thesis

„Noise Mechanisms in Heat-Assisted Magnetic Recording“

verfasst von / submitted by

Dipl.-Ing. Olivia Muthsam, BSc

angestrebter akademischer Grad / in partial fulfilment of the requirements for the degree of

Doktorin der Naturwissenschaften (Dr.rer.nat.)

Wien, 2019 / Vienna 2019

Studienkennzahl lt. Studienblatt / degree programme code as it appears on the student record sheet:	A 796 605 411
Dissertationsgebiet lt. Studienblatt / field of study as it appears on the student record sheet:	Physik
Betreut von / Supervisor:	Assoz. Prof. Dipl.-Ing. Dr. techn. Dieter Süss, Privatdoz

Acknowledgement

An dieser Stelle möchte ich mich zuerst bei meinem Betreuer Dieter Suess bedanken. Danke Dieter für die Ermöglichung meiner Dissertation, für die Bereitstellung der Finanzen, die Ermöglichung der vielen Konferenzen und deine gesamte Unterstützung während der Dissertation.

Ein großes Danke auch an dich, Christoph. Danke, dass du dir immer für mich Zeit genommen hast und jedem Verbesserungsvorschlag ein Lob vorausgeschickt hast. Du hast mir immer weitergeholfen und ich habe wirklich sehr viel von dir gelernt.

Danke auch der gesamten Arbeitsgruppe, in der ich mich sofort wohl gefühlt habe. Danke Amil, Basti, Christian, Christoph, Claas, Flo B., Flo S., Gregor, Herbert, Klaus, Markus, Paul, Peter, Pizzi, Sabri und Toni für die vielen guten Gespräche, für die anregenden Diskussionen und auch für das viele gemeinsame Lachen und den Spaß, den wir hatten. Besonderen Dank vor allem an euch, Gregor W. und Flo S., für die gute Zusammenarbeit und die Freundschaft, die im Laufe der Zeit entstanden ist.
Vielen Dank an die gesamte Physics of Functional Materials Gruppe für die freundliche Aufnahme und insbesondere Sabine Puchberger für die entstandene Freundschaft.

Meiner Familie möchte ich ein riesengroßes Danke aussprechen dafür, dass ihr immer für mich da wart und mich bei all meinen Entscheidungen unterstützt habt. Mama und Vicky, danke, dass ihr mich auf all meinen Wegen begleitet habt und in jeder Situation zu mir haltet. Papa, ich hoffe, du wärst stolz auf mich!

An meinen lieben Freund Gregor: Danke für deine Liebe, deine Unterstützung und dass du mein Ruhepol warst, wenn mir alles zu viel war.

Thank you to the Reviewers who have agreed to review my dissertation.

I would like to thank the Vienna Science and Technology Fund (WWTF) under grant

No. MA14-044, the Advanced Storage Research Consortium (ASRC), the Austrian Science Fund (FWF) under grant No. I2214-N20, and the Christian Doppler Laboratory – Amsen for the financial support.
The computational results presented in this work have been mainly achieved using the Vienna Scientific Cluster (VSC).

Erklärung zur Verfassung der Arbeit

Dipl.-Ing. Olivia Muthsam
Dr. E. Schrödingerstraße 6, 2000 Stockerau

Hiermit erkläre ich, dass ich diese Arbeit selbstständig verfasst habe, dass ich die verwendeten Quellen und Hilfsmittel vollständig angegeben habe und dass ich die Stellen der Arbeit - einschließlich Tabellen, Karten und Abbildungen -, die anderen Werken oder dem Internet im Wortlaut oder dem Sinn nach entnommen sind, auf jeden Fall unter Angabe der Quelle als Entlehnung kenntlich gemacht habe.

Ort, Datum	Unterschrift

Kurzfassung

Die Nachfrage nach Speichermedien steigt mit dem wachsenden Datenvolumen. In den letzten 50 Jahren ist die Speicherdichte von Festplatten exponentiell gewachsen. Heutzutage hat sich das Wachstum allerdings verlangsamt, da die verwendeten konventionellen Speichertechniken keine Speicherdichten im Bereich von mehreren Tb/in^2 erzeugen können. Die wärmeunterstützte magnetische Aufzeichnung (HAMR) [englisch: heat-assisted magnetic recording] ist eine Speichertechnik, die die Speicherdichten von Festplatten über das Limit der derzeit genutzten Speichermethoden hinaus verbessert. Die Schlüsseltechnologie bei HAMR besteht darin, einen thermischen Impuls in den Speicherprozess zu integrieren, um die Koerzitivfeldstärke von hochanisotropen Materialien zu senken und sie mit den verfügbaren Kopffeldern schreiben zu können. Der Hitzepuls stellt jedoch viele Herausforderungen dar. Ein großes Problem sind thermische Schreibfehler, die zu unerwünschtem Schreiben von benachbarten Körnern oder dem Zurückschalten von Körnern aufgrund einer zu langsamen Abkühlungsphase führen können. Das Ziel dieser Arbeit ist es, verschiedene Herausforderungen in HAMR zu untersuchen und geeignete Lösungen zur Reduzierung thermischer Schreibfehler zu finden.

Der wichtigste Parameter zur Bestimmung der Qualität der aufgezeichneten Bits ist das Signal-Rausch-Verhältnis (SNR) [englisch: signal-to-noise ratio]. Es gibt an, wie gut das ausgelesene Signal im Vergleich zum Hintergrundrauschen ist. Es ist von großem Interesse, den Einfluss verschiedener Material- und Schreibkopfparameter auf den SNR zu verstehen. Die umfassende Untersuchung in dieser Arbeit zeigt, dass die Dämpfungskonstante ein kritischer Parameter für die Verbesserung der Qualität von geschriebenen Bits in HAMR ist.

Eines der bisher unbeachteten Probleme bei HAMR ist die Tatsache, dass der aufgebrachte Hitzepuls zu einem Temperaturgradienten im Aufzeichnungsmaterial führt. Es wird untersucht, wie dieser Temperaturgradient die Aufzeichnungsleistung in Be-

zug auf die maximal mögliche Schaltwahrscheinlichkeit und die Breite des Übergangs zwischen den Bits beeinflusst. Darüber hinaus wird veranschaulicht, dass ein künstlicher Curie-Temperaturgradient innerhalb des Materials den Leistungsverlust durch den Temperaturgradienten ausgleichen kann.

Das größte Problem bei hartmagnetischen FePt-ähnlichen Körnern, die für den Einsatz in HAMR vorgesehen sind, ist die Tatsache, dass diese Körner trotz des angelegten Schreibfeldes nicht zuverlässig während vernünftiger Zeiten beschrieben werden können. Dies führt zu dem sogenannten DC-Rauschen, das die maximale Schaltwahrscheinlichkeit von Bits begrenzt. Dies bedeutet, dass die Informationen nicht zuverlässig geschrieben werden. Eine Struktur bestehend aus einer Schicht hartmagnetischem und einer Schicht weichmagnetischem Material mit erhöhter Curie-Temperatur ermöglicht eine Verbesserung der maximalen Schaltwahrscheinlichkeit auf 100%. Diese doppelschichtige Struktur führt jedoch zu hohem AC-Rauschen, was zu größeren Übergangsbereichen zwischen den Bits und damit einer begrenzten Speicherdichte führt. Die weichmagnetische Materialzusammensetzung einer Doppelschichtstruktur wird in dieser Arbeit optimiert, um sowohl AC- als auch DC-Rauschen zu reduzieren. Die Ergebnisse zeigen, dass beide Rauschquellen reduziert werden können sowie dass die optimale Materialzusammensetzung stark von der Dämpfungskonstante abhängig ist.

Der Hitzepuls führt zu einer weiteren Herausforderung bei HAMR. Durch das gekrümmte thermische Profil des Hitzepulses ist der Übergang zwischen den Bits stärker gekrümmt als bei den derzeit verwendeten Speichertechniken. Es wird erwartet, dass dies die Qualität des Rücklesesignals und damit den resultierenden SNR beeinflusst. Vor kurzem wurde ein Schreibkopfdesign mit vertauschten Polen vorgeschlagen, bei dem ein großer räumlicher Feldgradienten des Schreibkopfes der Schlüssel ist, um die Krümmung zwischen den Bits zu reduzieren. In dieser Arbeit wird der Schreibpol eines HAMR Schreibkopfes optimiert, um sowohl große Feldgradienten als auch große Felder im Bereich des Hitzepulses zu erzeugen. Dies geschieht durch Topologieoptimierung. Die Ergebnisse zeigen, dass die Steigerungen des Feldgradienten durch die Optimierung nicht ausreicht, um eine signifikante Reduzierung der Krümmung zu erreichen. Es lässt sich erneut nachweisen, dass die Dämpfungskonstante des Speichermaterials eine Schlüsselrolle bei der Reduzierung der Übergangskrümmung spielt.

Abstract

The demand for storage devices increases with the growing amount of data. Over the last 50 years, the areal density in magnetic hard disk drives (HDD) has experienced exponential growth. However, the growth rate has slowed down since conventional recording techniques that are used nowadays cannot produce areal storage densities (AD) in the range of several Tb/in^2. Heat-assisted magnetic recording (HAMR) is a recording technique that can improve the areal storage densities of hard disk drives beyond the density limits of conventional recording techniques. The key technology in HAMR is the inclusion of a heat pulse in the recording process to lower the coercivity of high-anisotropy materials and make them writeable with the available head fields. However, the heat pulse causes diverse challenges. A big problem are thermally written-in errors which can lead to unwanted writing of neighboring grains or back-switching of grains due to slow cooling. The aim of this work is to investigate various noise sources in HAMR that lead to thermally written-in errors and find suitable solutions to reduce them.

The main parameter to determine the quality of the recorded bits is the signal-to-noise ratio (SNR). It gives a measure on how good the read-back signal of a GMR read head is compared to the background noise. It is of great interest to understand the influence of various material and write head parameters on the SNR. The comprehensive investigation of this work shows that the damping constant of the material of the recording grains is a critical parameter to improve the quality of written bits in HAMR.

One of the problems in HAMR which has remained unobserved so far is the fact that the applied heat pulse leads to a temperature gradient within the recording material. It is investigated how this temperature gradient influences the recording performance in terms of the maximum possible switching probability and the width of the transition between bits. Moreover, it is illustrated that an artificial Curie

temperature gradient within the material can compensate the performance loss due to the temperature gradient.

The biggest problem with hard magnetic FePt-like grains, intended for the use in HAMR, is the fact that this type of grain cannot be reliably written during reasonable access times, despite the applied head pulse. This leads to the so-called DC noise, which limits the maximum switching probability of bits. An bilayer structure consisting of 50% hard and 50% soft magnetic material with graded Curie temperature allows to improve the maximum switching probability to 100%. However, this bilayer structure leads to high AC noise, which results in larger transition areas between bits and thus limits the areal density. In this work, the soft magnetic material composition of a bilayer structure is optimized in order to reduce both AC and DC noise. The results show, that both noise sources can be reduced and that the optimal material composition is strongly depending on the damping constant.

The heat pulse leads to another challenge in HAMR. Due to the curved thermal profile of the heat pulse, the transition between bits is significantly more curved than it is for conventional recording techniques. This is expected to reduce the quality of the read-back signal and thus the resulting SNR. Recently, a write head design with flipped write and return poles was proposed where a large spatial field gradient of the write head is the key to significantly reduce the transition curvature. In this work, the write pole of a heat-assisted magnetic recording head is optimized in order to produce large field gradients as well as large fields in the region of the heat pulse. This is done by topology optimization. The results show that the gradients of the optimized head design are not sufficient to lead to any significant improvement of the written track. It is again shown, that the damping constant of the recording material plays a key role for the curvature reduction.

Abbreviations

AD	areal storage density
ASRC	Advanced Storage Technology Consortium
BPM	bit-patterned media
ERTW	effective recording time window
ESM	exchange spring medium
FWHM	full width at half maximum
HAMR	heat-assisted magnetic recording
HDD	hard disk drive
HDMR	heated-dot magnetic recording
HM	hard magnetic material
HMS	head-to-media spacing
LLB	Landau-Lifshitz-Bloch
LLG	Landau-Lifshitz-Gilbert
LMR	longitudinal magnetic recording
MAMR	microwave-assisted magnetic recording
NFT	near field transducer
PDE	partial differential equation
PMR	perpendicular magnetic recording
SDD	solid state drive
SM	soft magnetic material
SMR	shingled magnetic recording
SUL	soft magnetic underlayer
SNR	signal-to-noise ratio
TDMR	two-dimensional magnetic recording

Contents

Chapter 1

Introduction

1.1 Background

The rapid growth of data results in the need of a continued increase in the capacity of storage devices. 2017, IBM released a study [1] that 90% of all data back then were created in the last two years. 2018, 2.5 quintillion bytes of data were created every day. It is expected that the total amount of data created reaches 44 ZB in 2020 [2] ($1\,\mathrm{ZB} = 1\,\mathrm{zettabyte} = 10^{21}\,\mathrm{bytes}$). Hard disk drives (HDDs) [3–6] are non-volatile magnetic storage devices which are commonly used as secondary storage devices in desktop computers, multiple user computers, digital video recorders and automotive vehicles. Secondary storage devices store the data until it is explicitly deleted in contrast to primary storage devices (RAM, Cache) that keep the data only for a short period of time while the computer is running. Hard disk drives consist of a rotating disk which are called platters and are coated with magnetic material. Via a moving actuator arm, a magnetic recording head is mounted to the HDD and is used to write and read the data. A picture of a HDD with the platters and the actuator arm with the recording head is shown in Figure 1.1.

With the increasing amount of data it is not efficient to just produce more storage devices since this would lead to more costs and a higher energy consumption. Hence, it is necessary to increase the areal storage density (AD) of the storage devices. Until 2010, the areal density of hard disk drives doubled almost every two years similar to Moore's law for integrated circuits, with a minimum compound annual growth rate (GGR) of $\sim 40\%$ per year [8, 9]. In almost 60 years the result is an impressive growth of 500 million times from the first IBM HDD with an AD of $2000\,\mathrm{bits/in^2}$ in 1956 [10] to a HDD introduced by Seagate in 2012 with an AD of $1.0\,\mathrm{Tb/in^2}$ [11] ($= 1$ Terabit per square inch $= 10^{12}$ bits per square inch). However, since 2010 the AD growth rate is saturating for conventional recording due to technical reasons.

Figure 1.1: Opened hard disk drive showing the platter and the actuator arm with the write and read head on the tip (orange area). Picture taken from [7].

Flash-based solid state drives (SSDs) [12, 13] are a big competition to HHDs when it comes to speed, power consumption and system performance but hard disk drives are the preferred solution when it comes to the price per Tb. Moreover, the growth rate of SSDs is very similar to that of HDDs and is also at a saturation point. In Figure 1.2, a comparison between the AD growth rate of hard disk drives and solid state drives is shown. In the graphic the milestones that led to higher areal densities for hard disk drives are indicated.

To keep hard disk drives competitive, new technologies and recording concepts have to be introduced. The most promising recording technology for further areal density growth is heat-assisted magnetic recording (HAMR) [3, 14–18]. According to the recording roadmap of the Advanced Storage Research Consortium (ASRC) [19] in Figure 1.3, areal densities up to $5\,\mathrm{Tb/in^2}$ can be reached for HAMR, in combination with bit-patterned media [20–22] even densities up to $10\,\mathrm{Tb/in^2}$ are predicted. Although, heat-assisted magnetic recording was already introduced 60 years ago [18], it is not commercially available yet due to several technical challenges. However, Seagate is already shipping test HDDs with HAMR techonolgy to clients [23]. The motivation of this work is to find suitable solutions for some challenges that come

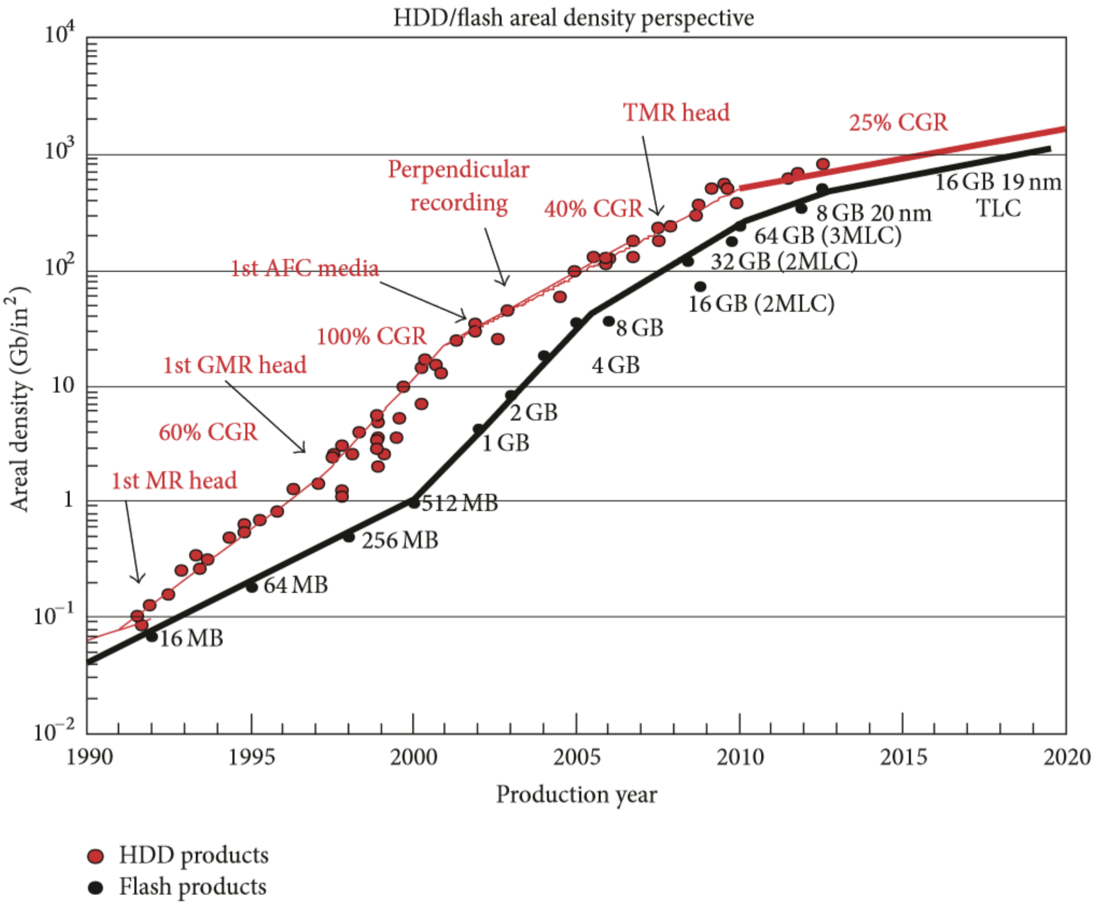

Figure 1.2: Development of areal density for hard disk drives and flash-based solid state drives (SSDs). CGR is the annual compound growth rate. Picture taken from [9].

with the technology of heat-assisted magnetic recording in order to keep HDDs competitive by further increasing the areal density.

1.1.1 Structure of the doctoral thesis

The structure of this thesis is as follows:

- **Chapter 2** gives a short introduction into the basics of magnetic recording and the magnetic recording components. Further, the magnetic recording trilemma is explained. To overcome it, it is necessary to introduce new recording concepts. Heat-assisted magnetic recording is presented as a technology to surmount this recording trilemma. Finally, challenges that occur with HAMR are described.

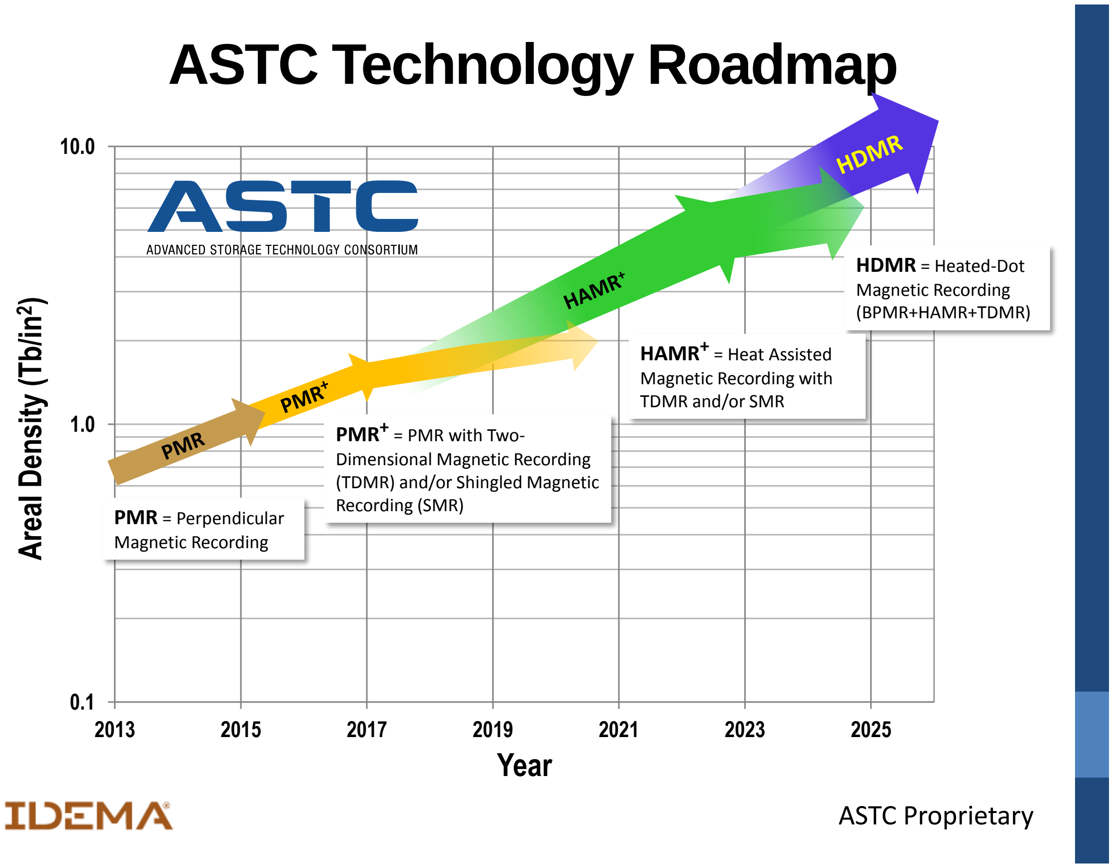

Figure 1.3: Recording technology roadmap according to the Advanced Storage Research Consortium with predicted areal density growth for heat-assisted magnetic recording. Picture taken from [19].

- In **Chapter 3** the simulation tools used in this work are described. Atomistic simulations, a macrospin model and two qualitative models to determine the switching probability of the recorded grains are explained. Moreover, it is stated which HAMR model is taken and how important parameters can be extracted from a phase diagram that shows the switching probability of recording grains.
- **Chapter 4** presents a study on how different write head and recording material parameters influence the signal-to-noise ratio (SNR). The SNR gives the power of the signal over the power of the noise and can be taken as a measure for the quality of written bits.
- **Chapter 5** investigates the influence of the temperature gradient in $z-$direction on the recording performance of a heat-assisted magnetic recording grain. It

further shows a way to compensate the loss of recording performance due to the temperature gradient by varying the Curie temperature within the material.

- **Chapter 6** introduces a way to reduce noise by optimizing a recording medium which consists of a hard and a soft magnetic layer. Different material parameters of the soft magnetic layer are varied and the material composition with the lowest AC and DC noise is chosen. Furthermore, the volume ratio between the hard and the soft magnetic layer is optimized. This is done for two different hard magnetic layers and the results are compared. Moreover, it is concluded how much the areal density can be increased by using the optimized structure.
- **Chapter 7** investigates a concept to reduce transition curvature which is enhanced due to the Gaussian shape of the heat pulse. A write head's topology is optimized in order to produce maximum fields and field gradients. With the resulting write heads it is studied if the transition curvature can be efficiently reduced.
- **Chapter 8** summarizes the doctoral thesis.

Chapter 2

Fundamentals in Magnetic Recording

In this chapter an introduction to magnetic recording is given. The essential concepts in magnetic recording are presented and an overview over the development in magnetic recording is given. Furthermore, the magnetic recording trilemma is explained and heat-assisted magnetic recording as a way to overcome this trilemma is introduced. Finally, the challenges that occur in HAMR are examined.

2.1 Magnetic Recording Basics

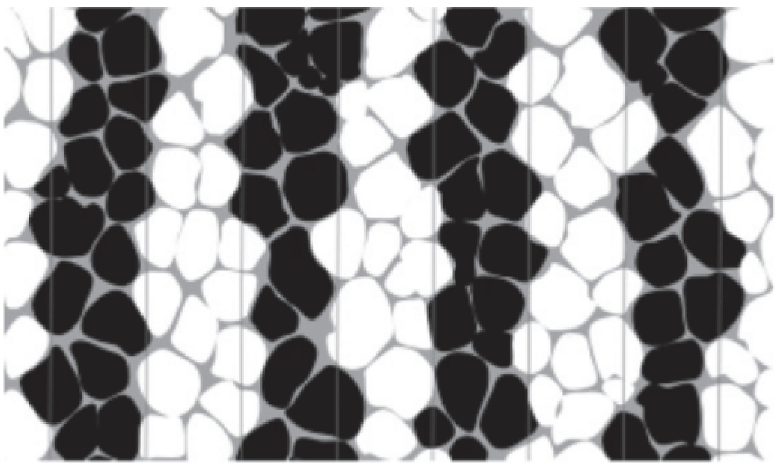

Figure 2.1: Schematic representation of bits at a granular recording medium in the two magnetization states (black and white) that consist of a number of grains. Picture taken from [3]

The main source of this section is [3], others are explicitly mentioned.

The first generation of hard disk drives was introduced by IBM in 1956 [10] and had an areal density of 2000 bits/in^2. The so-called IBM 305 RAMAC consisted of 50 disks with a diameter of 24 inch each. It weighted over one ton and was leased for $ 750 per month. The information was stored on the magnetic material of the rotating disks. The magnetic surface of HDDs is divided into small magnetic regions that are almost uniformly magnetized, see Figure 2.1. Each of these regions represents one bit which nowadays consists of 10 to 20 grains that have a diameter below 10 nm. The information is stored in two magnetic polarities that correspond to either a logical 0 or a logical 1. It is written to the magnetic recording medium with write heads and accessed again with read heads. In today's HDDs, recording heads provide both a writing and a reading component which are separated by a shield. Basically, write heads are electromagnets, yokes that are surrounded by a coil, and use the principle of induction to produce a write field that sets the magnetization direction of the grain. If the polarity of the current through the coil is reversed, the magnetization direction of the pole tip reverses as well. The reading part of the recording head is in principal a GMR sensor that uses the giant magneto-resistance effect [24, 25] to determine the direction of the magnetization of the bit below.

The first widely commercially used recording technique was longitudinal magnetic recording (LMR) [26]. In LMR, the grain's magnetization direction is parallel to the surface of the recording medium (see Figure 2.2). The single grains are aligned one by one with the poles next to each other. The direction of the applied field determines the magnetization direction of the grain. To avoid that the magnetizations of the grains are influencing each other, the grains are separated by non-magnetic material which limits the maximum reachable areal storage density. The main contribution in LMR to further increase the AD is the reduction of the size of the grains. However, the reduction of the grain size is restricted by the superparamagnetic limit [27, 28] which is explained in more detail in Section 2.2 and leads to the thermal instability of the magnetization of the medium. Thus, the storage density in longitudinal magnetic recording is restricted to 100 Gbits/in^2 [29].

In 1975, Iwasaki introduced perpendicular magnetic recording (PMR) [30]. It took 30 years until the first hard disk drives with perpendicular magnetic recording technology were shipped by Toshiba in 2005 [31]. In perpendicular magnetic recording, a thicker magnetic recording layer is used and the grains are magnetized perpendicular to the surface of the disc as seen in Figure 2.2 [32]. Compared to LMR the demagnetization field of the grains is lower and thus more grains are able to be stable in the same area. Furthermore, in PMR the magnetization of adjacent grains is not directly opposite. Hence, the non-magnetic transition regions between the grains can be significantly reduced compared to LMR. Another main difference between LMR and PMR is the use of a soft magnetic underlayer (SUL) [33, 34] in perpendicular magnetic recording. The SUL is regarded as a part of the write head since it provides magnetic flux return paths. Due to the SUL, magnetic fields and field gradients are increased compared to LMR heads with the same materials. Thus, the coercivity of the grains can be enhanced such that the grain size can be reduced while the grain stays thermally stable. However, the areal storage density is also limited for perpendicular recording due to the so-called magnetic recording trilemma [35–37].

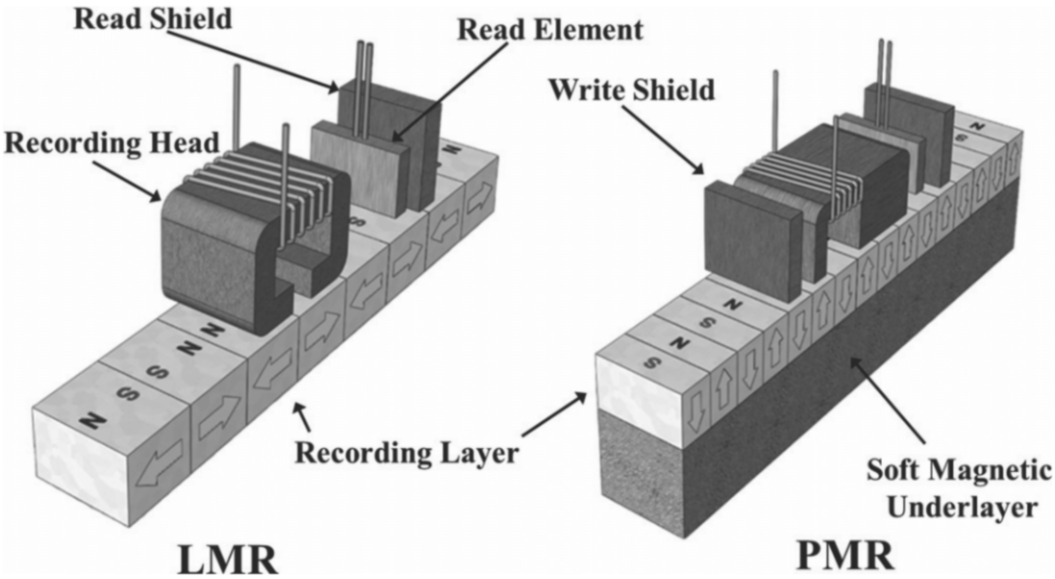

Figure 2.2: Comparison of longitudinal (left) and perpendicular (right) magnetic recording heads. Picture taken from [3]

2.2 Magnetic Recording Trilemma

In this section, the magnetic recording trilemma [35–39] explained in more detail. It is schematically depicted in Figure 2.3. In order to get higher areal densities, the size of each bit has to become smaller. The signal-to-noise ratio [40] which determines the quality of the signal in the read-back process is proportional to the number of grains in one bit [41, 42]. Thus, the number of grains per bit has to be nearly constant to

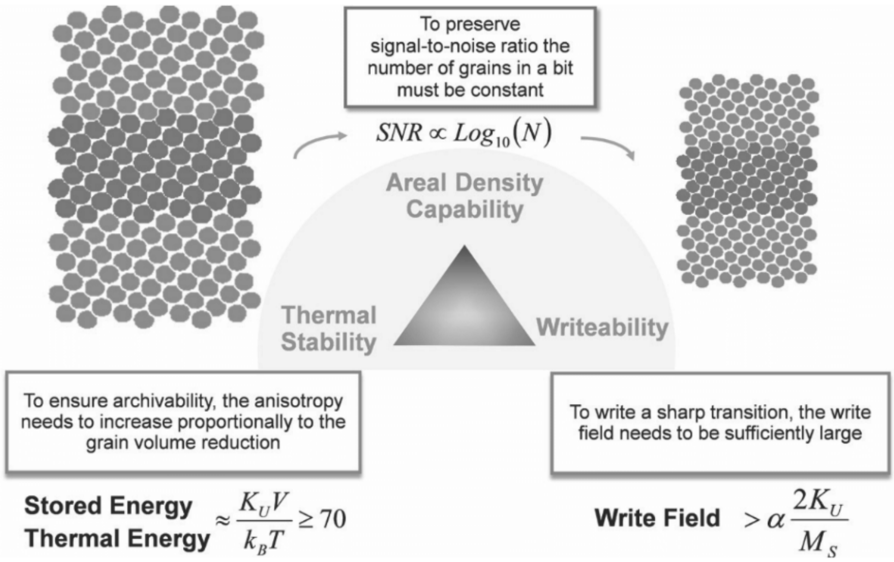

Figure 2.3: Schematic presentation of the magnetic recording trilemma. Picture taken from [3].

achieve similar SNR values which means that the size of each grain has to be reduced. The superparamagnetic limit [27,28] is a limitation in the reduction of the grain size. It describes the fact that very small ferromagnetic particles randomly loose their magnetization state even at temperatures clearly below the Curie temperature. The energy barrier E_b that has to be overcome to switch a grain with uniaxial anisotropy from one stable magnetization state to the other is given by

$$E_\mathrm{b} = k_\mathrm{u} V \tag{2.1}$$

where k_u is the uniaxial anisotropy constant and V is the grain's volume. With decreasing particle size, the energy barrier reduces due to the smaller grain volume and becomes comparable to the thermal energy

$$k_\mathrm{u} V \sim k_\mathrm{B} T \tag{2.2}$$

where k_B is the Boltzmann constant and T is the environment temperature. This means that thermal activation can occur even at room temperature ($T = 300\,\mathrm{K}$) which forces the magnetic moment of the grain to randomly flip with time without the presence of an external magnetic field. Thus, the magnetic order becomes unstable and the particles become superparamagnetic. In order to keep the magnetization of the grain thermally stable, the anisotropy constant has to be enhanced. A good reference value for a grain to be magnetically stable for 10 years is [3, 14].

$$\frac{k_{\mathrm{u}}V}{k_{\mathrm{B}}T} \geq 70. \tag{2.3}$$

Note, this value is not definite and is stated differently in different sources [28,36,43]. With the higher anisotropy of the grains writability becomes a problem. The write fields produced by the write heads are limited by the available head materials. The highest saturation polarization discovered in nature is $J_{\mathrm{s}} = 2.4\,\mathrm{T}$ [44]. Moreover, the decreasing size of bits demands for the write heads to become smaller in order to focus the field enough to write the desired grain only. However, smaller write heads produce smaller write fields lower than 1 T [45], such that the high-anisotropy grains cannot be written.

The magnetic recording trilemma limits the areal density that can be reached with perpendicular magnetic recording to about $1\,\mathrm{Tb/in}^2$. There are several ideas how to achieve higher areal densities like graded media [46–50], Shingled Magnetic Recording (SMR) [51–53], Two-dimensional Magnetic Recording (TDMR) [53–55], Bit-patterned media (BPM) [20–22], Microwave Assisted Magnetic Recording (MAMR) [56–59] and Heat-assisted Magnetic Recording (HAMR) [14–17]. However, there is broad agreement that the most promising candidate technology for the next generation of HDDs is HAMR.

2.3 Heat-assisted magnetic recording

Heat-assisted magnetic recording [3,14–18] is the most promising technology to overcome the recording trilemma. In HAMR, a heat pulse is added in the writing process and the medium is locally heated near or above the Curie temperature. This heating of the recording medium near or above the Curie temperature T_{C} leads to a continuous drop of the intrinsic magnetic properties such as coercivity H_{c}, magnetic anisotropy k_{u} and the saturation magnetization M_{s} [15]. With the reduced coercivity the switching field reduces and the grain can be written with the write fields provided by the recording head. After the grain is written, the medium is rapidly cooled and the information is permanently stored. The writing and cooling process happen on the same time scale of about 1 ns [14]. A schematic picture of the HAMR principle can be seen in Figure 2.4.

The big advantage of HAMR is that grains with high anisotropy can be used. Hence,

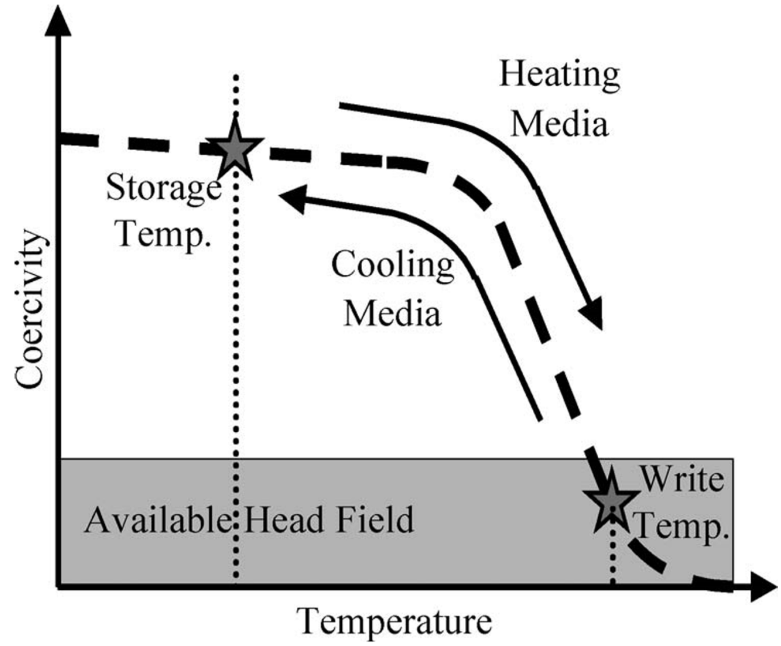

Figure 2.4: Schematic representation of the writing process in heat-assisted magnetic recording. Picture taken from [14].

the grain size can be reduced while the grains stay thermally stable. Another advantage of HAMR is that high effective write field gradients can be achieved without special requirements on the write head. The write field gradient can be written as [3, 14, 60]

$$\frac{dH_{\text{write}}}{dx} \sim \frac{dH_{\text{ext}}}{dx} - \frac{dH_k}{dT}\frac{dT}{dx} \tag{2.4}$$

where $\mathrm{d}H_k/\mathrm{d}T$ is the temperature dependence of the anisotropy field H_k just below the Curie temperature and $\mathrm{d}T/\mathrm{d}x$ is the thermal gradient at the freezing temperature in the down-track direction. The freezing temperature is the temperature below which the coercivity is so high that the grain cannot be written with the available write field. dH_{ext}/dx is the gradient of the external field in down-track direction. In contrast to inductive head designs the write field gradients with HAMR heads can be 3 to 20 times larger because $dH_k/dT \cdot dT/dx >> |dH_{\text{ext}}|/dx$. These high effective write field gradients lead to sharp transitions between bits such that higher down-track recording densities can be achieved. HAMR was proposed almost 60 years ago by Burns *et al* [18]. Despite a lot of research that has been done in HAMR, hard disk drives that use HAMR are still not commercially available yet but Seagate is currently shipping test HDDs with HAMR technology to clients [23]. The reason why HAMR HDDs are still not commercially available is that there are different challenges in HAMR and novel components had to be developed [3,17,61,62]. A few of these challenges are described in the further course.

2.3.1 Challenges in HAMR

Light Delivery System

In HAMR, laser light is used to enable the heating of the recording medium. One challenge in HAMR was the production of an efficient light delivery system that focuses the light well below the diffraction limit [14,63]

$$d = \frac{0.51\lambda}{n}. \tag{2.5}$$

λ is the wavelength of the light and n the index of refraction of the lens material. With conventional far field optics it is not possible to focus the heat spot to a spot size below 60 nm and simultaneously get enough power to reliably heat the recording medium [16]. However, for HAMR spot sizes below 20 nm are needed. Thus, so-called near field transducers (NFT) [16,63–65] are used to focus the light to sub-20 nm spots with the sufficient power. Near field transducers are made out of plasmonic material like gold or aluminum and use antennas and apertures to focus the light. Usually, a diode laser with $\lambda \sim 800$ nm is used [66,67]. In this area, the research has made huge progress and nowadays there exist near field transducers that efficiently delivery the light to the recording medium [68–70].

HAMR Head

The next challenge is the integration of the NFT to the write head [14, 71]. The integrated HAMR head has to fulfill several requirements. The write pole of the head has to be close to the NFT to provide a sufficiently high head field and high field gradients at the position of the heat spot and the head has to fly at head to media spacings (HMS) below 10 nm [14]. Furthermore, it has to be small, reliable and producible in mass at low cost. Commonly in literature, the laser is attached on a submount that is fixed to the top surface of the head [3, 72, 73].
Generally, there are three possible ways to define the dimension of the bit. It is possible to either

(a) focus the heat spot and have a non-local field,

(b) focus the field and have a non-local heat spot or

(c) focus both the field and the heat spot.

Typically, possibility (a) is chosen where the write field defines the magnetization direction and the heat spot defines the bit dimension [67]. The write head can then be larger and thus, a higher head field can be achieved. The high field gradients and sharp transitions between bits can be achieved by optimizing the soft magnetic underlayer. The head materials need to have high saturation polarization J_s to produce high head fields. FeCo is such a material with $J_\mathrm{s} = 2.4\,\mathrm{T}$ [44].

HAMR Medium

To achieve higher areal storage densities, not only the recording technique is crucial but also the choice of the recording material. Another challenge in HAMR is to find suitable low-noise high anisotropy magnetic media with grain sizes below $5-6\,\mathrm{nm}$ [3, 14, 17, 43]. High magnetocrystalline anisotropy over $3.5\,\mathrm{MJ/m^3}$, a grain size distribution below 10%, a Curie temperature distribution about 2% and a grain-aspect ratio h/D greater than 1.5 (where h is the height and D the diameter of the grain) are desired [43, 74]. The recording material has to combine a good recording performance with a good mechanical performance [17]. For this purpose, FePt based materials are the most promising [75–77]. In the production process of high anisotropy $L1_0$ phase media, elevated temperatures are needed to order the atoms in the right way. However, this makes it hard to form grains which are slim and tall since the grains tend to become spherical at elevated temperatures [17].
To protect the recording medium from damage caused by the elevated temperature, special lubricants and overcoats are needed. This means that the head disk interface has to be robust. To enable the recording layer to cool quickly after the writing process, a heat sink is additionally needed [78–80].

Bit-patterned Media (BPM) and Heated-dot Magnetic Recording (HDMR)

The materials used for recording at the moment are granular media [76, 77, 82]. As explained in Section 2.2, 10 to 20 grains that are weakly exchange coupled and separated by non-magnetic boundary materials, compose one bit, see Figure 2.5(left). These grains are different in shape, size and arrangement. The energy barrier of

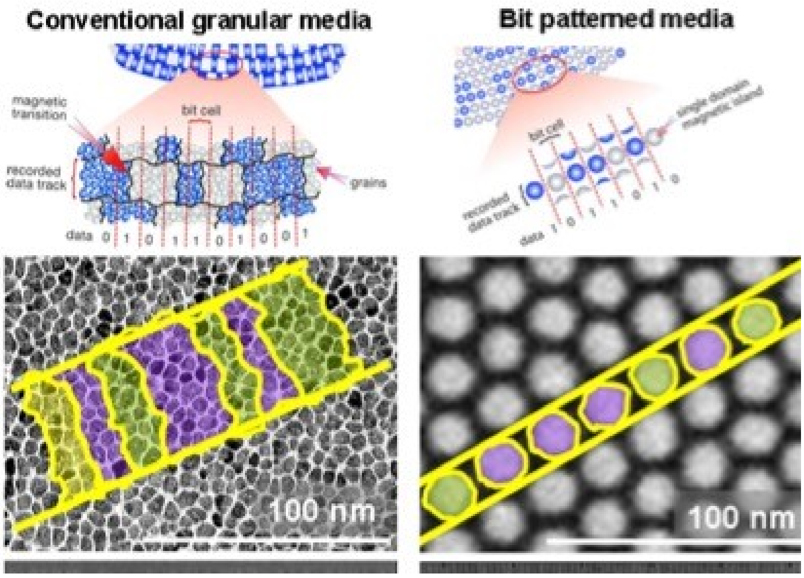

Figure 2.5: Comparison of (left) granular recording medium and (right) bit-patterned media. (Top) Illustration of the recording systems on the disk. (Bottom) Schematic representation of the bits in both media structures. Picture taken from [81]

granular media, which has to be overcome to switch the bit, is proportional to the volume of the grains. Hence the areal density is limited by the superparamagnetic limit of the single grains [28]. An alternative to granular recording material is bit-patterned media [20–22,83]. In bit-patterned media, the grains are strongly exchange coupled and then patterned into magnetic islands with the help of nanolithography [84,85]. Every magnetic island is one bit of information. In this material, the energy barrier is proportional to the volume of the whole bit. Since now the volume of the island can be as small as the volume of one single grain in granular media, higher storage densities can be achieved with bit-patterned media. The combination of HAMR with bit-patterned media is called heated-dot magnetic recording (HDMR) [43]. It is expected that HDMR can extend the areal density of HDDs beyond 10 Tb/in^2 [86]. Although the production of bit-patterned media is sophisticated and it is not possible to use bit-patterned media commercially yet, research in HAMR combined with bit-patterned media is an ongoing topic [87].

Thermally Induced Recording Errors

In HAMR, thermally written-in errors are a serious problem [60,88,89]. These include unwanted writing of neighboring grains due to accidentally heating the neighboring grains or a back-switching of the grains after they have been written due to too slow cooling. This leads to high AC and DC noise which limit the distance between neighboring grains and the maximum switching probability of grains, respectively. This thermal noise due to the heating of the material lowers the signal-to-noise ratio since the SNR gives the power of the signal over the power of the noise. Different mechanisms to study and reduce thermally written-in errors and the noise in HAMR media have been achieved with the help of computer simulations [40, 90]. In this work, approaches to determine the influence of different material and write head parameters on the SNR (see Chapter 4) and to optimize the recording medium in order to reduce AC and DC noise are demonstrated (see Chapter 6).
Another thermally induced problem in HAMR is the curvature of transitions between bits in state-of-the-art granular media. Curved transitions occur also in perpendicular magnetic recording [35, 91, 92]. In HAMR, the curved thermal profile of the heat pulse amplifies this transition curvature. Since this transition curvature is expected to limit the signal quality in the read-back process it is of great interest to reduce the transition curvature. Different approaches to reduce transition curvature have been proposed [93, 94]. In Chapter 7 these approaches are presented and further studies on transition curvature reduction that have been achieved during the course of this work are presented.

Chapter 3

Computer Simulations

Computer simulations are an important tool to investigate physical phenomena or test out new materials and devices without performing costly experiments. It is thus necessary that the computer simulations are reliable and efficient and provide approximations at very high accuracies. There are a variety of approaches on different length and time scales to model magnetism phenomena with the help of computer simulations, ranging from the detailed ab initio calculations [95] to the more general description with Maxwell's equations. In this work, the switching probability of recording grains during HAMR is computed with the help of atomistic simulations, a macrospin simulation tool and with two models that describe the switching behavior qualitatively. These models depend on each other as indicated in Figure 3.1, meaning that some models need input parameters that are determined from other models. In the following, an overview over the various models to simulate the HAMR process is given. Further, the model parameters for heat-assisted magnetic recording are introduced and ways to determine important properties like the maximum switching probability, the transition jitter and the signal-to-noise ratio are described.

3.1 Atomistic Simulations

The main source of this chapter is the publication by Evans *et al* [96], others are explicitly mentioned.

A lot of simulations in magnetism today are performed using micromagnetic modelling. However, often it is necessary to consider the detailed atomic structure of the materials and the changes on the atomistic level in the simulations. This is for example the case for sub-nanometer spatial variations in magnetization that are caused by high temperature, atomic level ordering or atomic surface and interface effects. In the atomistic simulations each atom is considered to possess a magnetic

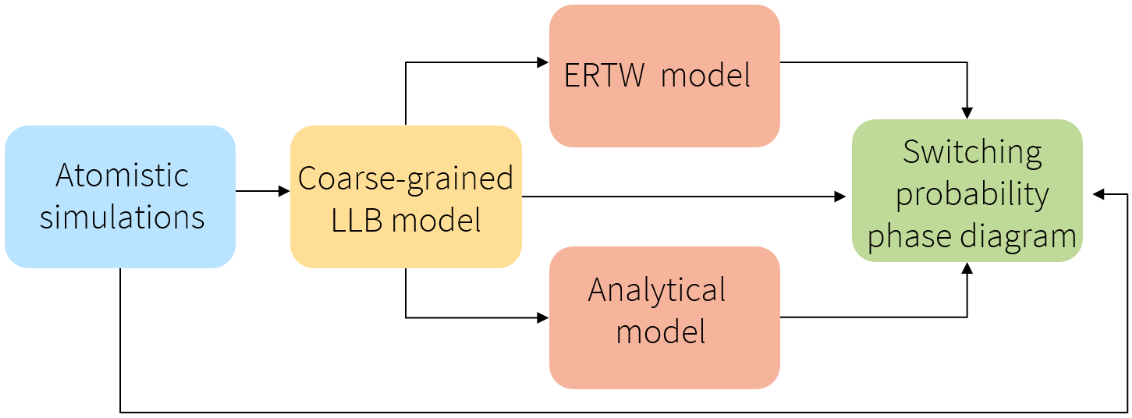

Figure 3.1: Overview over the different models to simulate the switching probability of recording grains during HAMR. The dependence of the different models on each other are indicated by the arrows. The input parameters for the models are determined by the previous models that they depend on.

moment. Atomistic models originate from the Ising model from 1925 which only considers spin-up and spin-down states and can be generalized by the Heisenberg model. In the following the classical Heisenberg spin model and the related energy contributions are explained. Further, the Landau-Lifshitz-Gilbert (LLG) equation that describes the time-dependent magnetization behavior and Langevin dynamics with which temperature-dependence can be added to the LLG equation are introduced.

3.1.1 Classical Spin Hamiltonian

The origin of atomistic models is the Ising model where only spin-up and spin-down states are considered. A generalization of the Ising model that allows the spins to move free in the 3-dimensional space is the Heisenberg spin model. The energetic behavior of the magnetic system in the Heisenberg model is described by a spin Hamiltonian. The spin Hamiltonian describes the magnetic interaction between the spins of the electrons of the atoms. Typically, the energy contributions that are considered in the spin Hamiltonian are the exchange energy $\mathcal{H}_{\mathrm{exc}}$, the Zeeman energy $\mathcal{H}_{\mathrm{zee}}$, and the anisotropy energy $\mathcal{H}_{\mathrm{ani}}$. With those, the spin Hamiltonian is given by

$$\mathcal{H} = \mathcal{H}_{\mathrm{exc}} + \mathcal{H}_{\mathrm{zee}} + \mathcal{H}_{\mathrm{ani}} \tag{3.1}$$

There are further energy contributions like the demagnetization energy which are not considered in this work. Below all three considered energy contributions are explained in more detail.

Exchange Energy

The dominant part in the Heisenberg spin Hamiltonian in the temperature range $300 - 1300\,\mathrm{K}$ is the exchange energy [96]. It has the effect that it is energetically more favorable for localized spins to be aligned parallel instead of antiparallel. The exchange energy has an electrostatic origin, it is of the order of $1 - 2\,\mathrm{eV}$ and is thus more than 1000 times larger than the next largest contribution. The exchange energy for a system of interacting moments is given by

$$\mathcal{H}_{\mathrm{exc}} = -\sum_{i \neq j} J_{ij} \boldsymbol{S}_i \cdot \boldsymbol{S}_j \tag{3.2}$$

where J_{ij} is the exchange interaction between the atomistic sites i and j, $\boldsymbol{S}_i$ is a unit vector denoting the local spin moment direction of atom i and $\boldsymbol{S}_j$ is the spin moment direction of a neighboring atom. $\boldsymbol{S}_i = \mu_{\mathrm{s}}/|\mu_{\mathrm{s}}|$, where μ_{s} is the atomic moment. For the exchange interaction J_{ij}, it is important to consider the correct sign. $J_{ij} > 0$ describes ferromagnetic materials whereas $J_{ij} < 0$ describes antiferromagnetic materials. In this work, an isotropic exchange interaction is used meaning that the exchange energy of two spins is only depending on their relative orientation. The exchange interaction is strongly depending on the distance. Thus, often only nearest neighbor exchange interactions are considered which reduces the computational effort and allows for larger system sizes.

Zeeman Energy

The energy of a ferromagnet is highly depending on the interaction between the system with an external field $\boldsymbol{H}_{\mathrm{appl}}$. The spins tend to align in the direction of the applied field. The energy contribution corresponding to this interaction is called Zeeman energy. It is given by

$$\mathcal{H}_{\mathrm{zee}} = -\sum_{i} \mu_{\mathrm{s}} \boldsymbol{S}_i \cdot \boldsymbol{H}_{\mathrm{appl}} \tag{3.3}$$

$\boldsymbol{S}_i$ is again a unit vector that gives the local spin moment direction of atom i and μ_{s} is the atomic spin moment.

Anisotropy Energy

Magnetic anisotropy is a contribution in which alignment of the spins along one or multiple axes, the so-called easy axes is preferred. The simplest form of anisotropy is uniaxial anisotropy where the magnetic moments prefer to align along one single axis. In this work only uniaxial anisotropy is considered. Uniaxial anisotropy results from the structure of the underlying crystal. Anisotropy is an effect that is only bounded to the local magnetic moments. It is given by

$$\mathcal{H}_{\mathrm{ani}}^{\mathrm{uni}} = -k_{\mathrm{u}} \sum_i (\boldsymbol{S}_i \cdot \boldsymbol{e})^2 \tag{3.4}$$

where k_u is the anisotropy energy per atom and $\boldsymbol{e}$ is the direction vector of the single easy axis.

3.1.2 Landau-Lifshitz-Gilbert (LLG) Equation

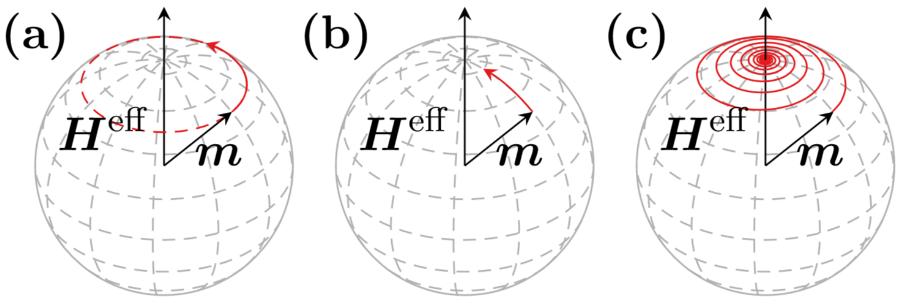

Figure 3.2: Schematic presentation of the contributions to the magnetization dynamics of the Landau-Lifshitz-Gilbert equation. In (a) the precessional motion around the effective field is depicted. In (b) the magnetization relaxation towards the effective field can be seen. (c) shows the combined precession and damping that are described by the LLG equation. Picture taken from [97].

A common way to describe time-dependent magnetization dynamics is the Landau-Lifshitz-Gilbert equation which is a nonlinear partial differential equation [96,98,99]. 1935, Landau and Lifshitz first introduced a basic dynamics equation for the magnetization based on a ferromagnetic resonance experiment [100]. This equation by

Landau and Lifshitz (LL equation) is given by

$$\frac{\partial \boldsymbol{m}}{\partial t} = -\gamma\,[\underbrace{\boldsymbol{m} \times \boldsymbol{H}_{\text{eff}}}_{\text{precessional motion}} + \underbrace{\lambda \boldsymbol{m} \times (\boldsymbol{m} \times \boldsymbol{H}_{\text{eff}})}_{\text{damping}}] \tag{3.5}$$

where γ is the gyromagnetic ratio and $\boldsymbol{m} = \boldsymbol{M}/M_{\text{s}}$ is a unit vector that describes the direction of the magnetization of the sample with $\boldsymbol{M}$ being the magnetization vector and M_{s} being the saturation magnetization. $\boldsymbol{H}_{\text{eff}}$ is the effective applied field that acts on the sample and λ is a phenomenological damping constant that depends on the material. The first term of the Landau-Lifshitz equation describes the precessional motion of the magnetization due to the interaction with the applied field (see Figure 3.2(a)). It can be derived from the Heisenberg equation of motion in the classical limit [98, 99, 101]. The second term characterizes the relaxation of the magnetization where the magnetization gradually rotates towards the external field (Figure 3.2(b)). The strength with which the magnetization is coupled to the external field is determined by the dimensionless damping parameter λ. In the original Landau-Lifshitz equation, the relaxation function was assumed to be linear. However, Gilbert replaced it with an equivalent damping term in 1955 yielding the Landau-Lifshitz-Gilbert equation [102]. In Figure 3.2(c), the combined precessional and dissipative motion that are described by the LL equation are shown. Since both terms of the LL equation contain a cross product, both terms are perpendicular to the magnetization.

The LLG equation was initially introduced for macroscopic magnetization dynamics where λ includes both intrinsic and extrinsic contributions. In contrast to this, the damping constant in the atomistic LLG equation only includes the local intrinsic contributions [96]. Thus, the microscopic damping parameter in the atomistic LLG equation is called α to distinguish it from the macroscopic damping parameter λ. With this, the atomistic LLG equation is given by

$$\frac{\partial \boldsymbol{S}_i}{\partial t} = -\frac{\gamma}{(1+\alpha^2)}[\boldsymbol{S}_i \times \boldsymbol{H}^i_{\text{eff}} + \alpha \boldsymbol{S}_i \times (\boldsymbol{S}_i \times \boldsymbol{H}^i_{\text{eff}})] \tag{3.6}$$

where α is the microscopic damping constant, γ is the gyromagnetic ratio, $\boldsymbol{S}_i$ is a unit vector that gives the direction of the magnetic spin moment on site i and $\boldsymbol{H}^i_{\text{eff}}$ is the effective field which is the net magnetic field acting on spin i. Note, that compared to eq. (3.5), in eq. (3.6) the damping term proposed by Gilbert is used, which leads (in the atomistic case with damping constant α) to the scaling factor

$1/(1+\alpha^2)$ [103]. The atomistic LLG equation describes the magnetization dynamics of an atomistic spin moment i in an effective field $\boldsymbol{H}^i_{\text{eff}}$. The effective field can be determined by

$$\boldsymbol{H}^i_{\text{eff}} = -\frac{1}{\mu_{\text{s}}}\frac{\partial \mathcal{H}}{\partial \boldsymbol{S}_i} \tag{3.7}$$

where μ_{s} is the local spin moment and $\mathcal{H}$ is the spin Hamiltonian of the system (see Section 3.1.1).
Note, that the LLG equation is only valid at zero temperature. Both, the damping constant and the saturation magnetization are constant and not temperature dependent.

3.1.3 Langevin Dynamics

As mentioned before, the classic LLG equation is only applicable at a temperature of 0 K. The absolute value of the magnetization is fixed, independently from the temperature. However, thermal effects lead to thermodynamic fluctuations of the spins. At high temperatures, these fluctuations have a stronger impact on the magnetization dynamics than the exchange interaction, leading to ferromagnetic-paramagnetic phase transitions. A way to include the thermal effects into the LLG equation are the Langevin dynamics, introduced by Brown [104]. In the Langevin dynamics [105–107], the effects of temperature are modeled as Gaussian white noise. A stochastic process ξ has white noise properties if

$$\langle \xi(t) \rangle = 0 \tag{3.8}$$

$$\langle \xi(t), \xi(t') \rangle = 2D\delta(t-t'), \tag{3.9}$$

meaning that the mean value is zero and the process is delta correlated [106]. If higher temperatures are assumed, the width of the Gaussian distribution increases which leads to stronger fluctuations. The thermal field on spin i at each time t is given by

$$\boldsymbol{H}^i_{\text{th}} = \boldsymbol{\Gamma}(t)\sqrt{\frac{2\alpha k_{\text{B}} T}{\gamma \mu_{\text{S}} \Delta t}} \tag{3.10}$$

where k_{B} is the Boltzmann constant, T is the system temperature, α is the Gilbert damping, γ is the absolute value of the gyromagnetic ratio, μ_{S} is the magnitude of the atomic magnetic moment and Δt is the integration time step. $\mathbf{\Gamma}(t)$ here is the Gaussian distribution in three dimensions with a mean value of zero that represents the thermodynamic fluctuations. Each spin has a different thermal field for each time step t. The combination of the atomistic LLG with the Langevin dynamics gives the effective field on spin i

$$\boldsymbol{H}_{\text{eff}}^{i} = -\frac{1}{\mu_{\text{S}}}\frac{\partial \mathcal{H}}{\partial \boldsymbol{S}_i} + \boldsymbol{H}_{\text{th}}^{i}. \tag{3.11}$$

Equation (3.6) together with eq. (3.11) is the stochastic Landau-Lifshitz-Gilbert equation.

3.1.4 Realization with VAMPIRE

The atomistic simulation software used in this work is VAMPIRE which was developed by Evans *et al* [96]. [96] is the main source of this section, others are explicitly mentioned.

Time Integration

The stochastic LLG equation (3.6) is a stochastic differential equation since the influence of temperature is treated with an uncorrelated Gaussian white noise [96, 108]. To numerically compute the dynamics of a system, appropriate time integration methods for stochastic differential equations are needed [106,108,109]. There is only a limited number of solvers that are applicable to stochastic differential equations, like the Heun method and other explicit midpoint schemes. The time integration method provided by VAMPIRE that is used in this work is the so-called Heun method. It is a second order Runge-Kutta scheme and consistent with the Stratonovich calculus [110,111]. The Heun method consists of a predictor and a corrector step. After both the predictor and the corrector step it is necessary to renormalize the length of the magnetization in order to preserve it. This ensures the stability of the numerical scheme and the convergence to the Stratonovich solution [96].
Assume a general Langevin equation

$$\frac{dx}{dt} = A(x,t) + B(x,t)\xi(t) \tag{3.12}$$

with the stochastic process ξ which has white noise properties as in (3.8) and (3.9). The predictor step of the Heun scheme is the given by [106, 112]

$$x_{j+1}^{[P]} = x_j + A(x_j, t_j)\Delta t + B(x_j, t_j)\Delta W. \tag{3.13}$$

W is a Wiener process [112, 113] with

$$\langle W \rangle \propto \sqrt{\Delta t} \tag{3.14}$$

Since the length of the magnetization is not preserved in the predictor step, it has to be renormalized. The intermediate spin positions are changed after the predictor step, so the effective field has to be re-evaluated which gives the revised effective field $\boldsymbol{H}_{\text{eff}}^{i'}$ [96]. The corrector step is then given by [112]

$$x_{j+1} = \frac{1}{2}x_j + \frac{1}{2}[x_{j+1}^{[P]} + A(x_{j+1}^{[P]}, t_{j+1})\Delta t + B(x_{j+1}^{[P]}, t_{j+1})\Delta W]. \tag{3.15}$$

This step is calculated for every spin. Lastly, the length of the magnetization is once more renormalized.

Input Parameters

In the following, the most important input parameters for VAMPIRE are stated in Table 3.1.

Parameter	Symbol	Unit
Atomic magnetic moment	μ_{s}	$\mu_{\text{B}} = 9.2740 \times 10^{-24}$ J/link
Exchange energy	J_{ij}	J/link
Anisotropy constant	k_{u}	J/atom
Damping constant	α	—
Applied field	$\boldsymbol{H}$	A/m
Temperature	T	K
Unit cell size	a	Å

Table 3.1: Key input parameters for VAMPIRE [96].

3.2 Coarse-grained LLB Model

Atomistic simulations are an accurate tool that consider the underlying crystal structure of the grain accurately. However, they are very time consuming and thus only applicable for small system sizes of some tens of nanometers. For structures on the micrometer scale, the Landau-Lifshitz-Bloch (LLB) equation can be used to model the dynamic magnetization behaviour. In contrast to the atomistic LLG equation, it summarizes the spins within a nanoparticle to just one magnetic moment. In this work, a coarse-grained model based on the LLB equation developed by Vogler *et al* [114] is used for simulation. First, the general Landau-Lifshitz-Bloch model is introduced. After that, it is explained how temperature dependent input parameters to the LLB model can be derived from atomistic simulations.

3.2.1 Landau-Lifshitz-Bloch (LLB) Equation

The main source of this section is [114], others are explicitly mentioned.

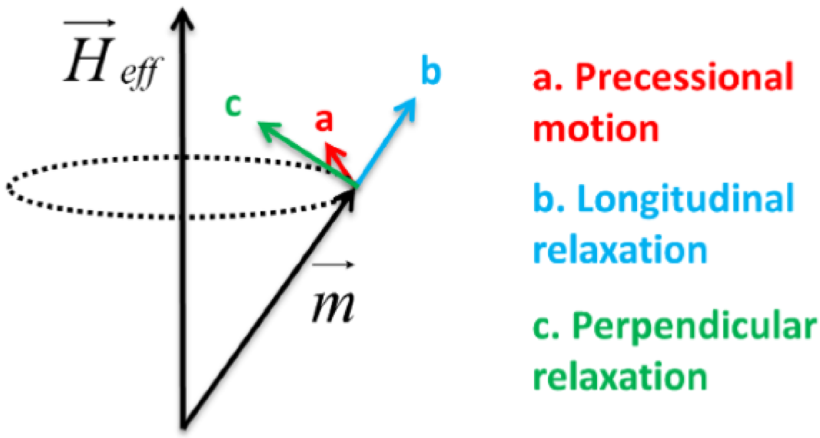

Figure 3.3: Schematic presentation of the contributions to the magnetization dynamics of the Landau-Lifshitz-Bloch equation with the precession, the longitudinal and the perpendicular magnetization relaxation. Picture taken from [115]

The Landau-Lifshitz-Gilbert equation in combination with Langevin dynamics is a good way to describe dynamic magnetization behavior at an atomistic length scale [96]. However, since each atom has to be described by one spin it is very time consuming. A macroscopic equation of motion that is valid for the whole temperature range is the Landau-Lifshitz-Bloch equation [114, 116]. It was derived directly from the Fokker-Planck equation by Garanin [117] and connects the Landau-Lifshitz equation for low temperatures and the Bloch equation for high temperatures. The LLB equation contains both transverse and longitudinal magnetization relaxation and allows for the absolute value of the magnetization to change with temperature. The transverse and longitudinal relaxation are schematically displayed in Figure 3.3. The classical LLB equation has the form

$$\begin{aligned}\frac{d\boldsymbol{m}}{dt} &= -\mu_0\gamma'(\boldsymbol{m}\times\boldsymbol{H}_{\text{eff}}) \\ &- \frac{\lambda_\perp\mu_0\gamma'}{m^2}\{\boldsymbol{m}\times[\boldsymbol{m}\times(\boldsymbol{H}_{\text{eff}}+\xi_\perp)]\} \\ &+ \frac{\lambda_{||}\mu_0\gamma'}{m^2}\boldsymbol{m}(\boldsymbol{m}\cdot\boldsymbol{H}_{\text{eff}})+\xi_{||}\end{aligned} \tag{3.16}$$

where γ' is the reduced electron gyromagnetic ratio [$\gamma' = |\gamma_e|/(1+\alpha^2)$, with $|\gamma_e| = 1.760859708 \times 10^{11}\,(\text{Ts})^{-1}$ with the intrinsic damping constant α of the atomistic LLG equation eq. (3.6)], μ_0 is the vacuum permeability and $\boldsymbol{m} = \boldsymbol{M}/M_0$ is the reduced magnetization. M_0 is the saturation magnetization at zero temperature. The dot product between the magnetic field and the magnetization in the third term in eq. (3.16) shows that it is parallel to the magnetization. $\xi_\perp$ and $\xi_{||}$ consist of white noise random numbers. $\lambda_\perp$ and $\lambda_{||}$ denote the dimensionless perpendicular and the transverse damping parameters, respectively. In contrast to the LLG equation, in the LLB equation both damping constants are temperature dependent and given by

$$\lambda_\perp = \begin{cases}\alpha(1-\frac{T}{T_{\text{C}}}) & T < T_{\text{C}}, \\ \lambda_{||} & T \geq T_{\text{C}},\end{cases} \qquad \lambda_{||} = \alpha\frac{2T}{3T_{\text{C}}}. \tag{3.17}$$

T_{C} is the Curie temperature. A thermal field ξ_η with $\eta = ||$ and $\eta = \perp$ is introduced for the longitudinal and perpendicular case. ξ_η consists of white noise random numbers with zero mean and variance

$$\langle \xi_{\eta,i}(t,\boldsymbol{r})\xi_{\eta,j}(t',\boldsymbol{r}')\rangle = 2D_\eta\delta_{ij}\delta(\boldsymbol{r}-\boldsymbol{r}')\delta(t-t') \tag{3.18}$$

where the diffusion constants D_η result from the fluctuation-dissipation theorem

$$D_\perp = \frac{(\lambda_\perp-\lambda_{||})k_{\text{B}}T}{\gamma'\mu_0^2 M_0 V\lambda_\perp^2}$$

$$D_{||} = \frac{\lambda_{||}\gamma' k_\mathrm{B} T}{M_0 V}. \tag{3.19}$$

The effective field in the LLB equation contains the same terms as the LLG equation but with temperature dependent constants. The anisotropy field $\boldsymbol{H}_\mathrm{ani}$ has the form

$$\boldsymbol{H}_\mathrm{ani} = \frac{1}{\chi_\perp}(m_x \boldsymbol{e}_x + m_y \boldsymbol{e}_y) \tag{3.20}$$

if the easy axis is assumed to be in $z-$direction. The perpendicular susceptibility $\chi_\perp$ is temperature dependent and contains the temperature dependent anisotropy constant K_1 and the temperature dependent magnetization $\boldsymbol{M}$. Additionally, $\boldsymbol{H}_\mathrm{eff}$ in the LLB equation contains an internal exchange field $\boldsymbol{H}_\mathrm{J}$ that controls the length of the magnetization. It is given by

$$\boldsymbol{H}_\mathrm{J} = \begin{cases} \frac{1}{2\tilde{\chi}_{||}}(1 - \frac{m^2}{m_e^2})\boldsymbol{m} & T \leq T_\mathrm{C}, \\ -\frac{1}{\tilde{\chi}_{||}}(1 + \frac{3}{5}\frac{T_\mathrm{C}}{T-T_\mathrm{C}} m^2)\boldsymbol{m} & T > T_\mathrm{C}, \end{cases}. \tag{3.21}$$

Concluding, the effective field of the LLB equation reads as [118]

$$\boldsymbol{H}_\mathrm{eff} = \boldsymbol{H}_\mathrm{exc} + \boldsymbol{H}_\mathrm{zee} + \boldsymbol{H}_\mathrm{ani} + \boldsymbol{H}_\mathrm{J}. \tag{3.22}$$

m_e is the zero-field equilibrium magnetization and $\tilde{\chi}_{||}$ the longitudinal susceptibility at zero-field condition. Both parameters are temperature dependent. Furthermore, k_B is the Boltzmann constant, T_C the Curie temperature and μ_0 is the vacuum permeability.

To integrate the LLB equation at arbitrary temperatures, the temperature dependence of m_e, $\tilde{\chi}_{||}$ and $\tilde{\chi}_\perp$ has to be known. For this purpose, LLG simulations with an atomistic spatial discretization of the underlying ferromagnetic particle can be used as well as a mean-field ansatz [114].

3.2.2 Calculation of Temperature Dependent Material Functions

All informations in this section are taken from [114].

Computation of $m_e(T)$

To calculate the zero-field equilibrium magnetization $m_e(T)$, simulations with the atomistic simulation program VAMPIRE [96] need to be performed. In the simu-

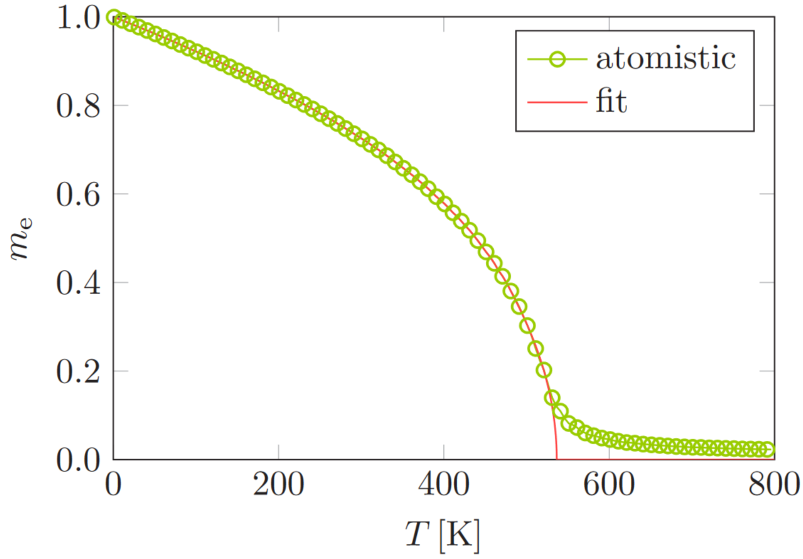

Figure 3.4: Zero-field equilibrium magnetization m_e over the temperature for a hard magnetic material. The simulations were performed with the atomistic simulation tool VAMPIRE [96]. Picture taken from [114].

lations the temperature is varied from 0 K to temperatures clearly above the Curie temperature ($\sim$ 1000 K). At each temperature, 128 trajectories are simulated with a duration of a few tens of nanoseconds without the presence of an external field. It is necessary to adjust the time step Δt according to the material parameters, especially the damping constant. For example, a reduction of the damping constant from $\alpha = 0.1$ to $\alpha = 0.02$ requires the time step to be changed from $\Delta t = 10^{-15}$ s to $\Delta t = 10^{-16}$ s. The resulting magnetization curve $< |m(T)| >$ averaged over the 128 trajectories show in Figure 3.4 is then fitted with

$$f(T) = c\sqrt{\frac{T_\mathrm{C} - T}{T_\mathrm{C}}} \tag{3.23}$$

to determine $m_e(T)$, where the Curie temperature T_C and the parameter c are the fitting parameters. This procedure has to be repeated for every material layer of the recording grain.

Computation of $\tilde{\chi}_\perp$ and $\tilde{\chi}_{||}$

The same simulations as above can be used to calculate the longitudinal and transverse susceptibility with respect to the easy axis of the grain. VAMPIRE has the

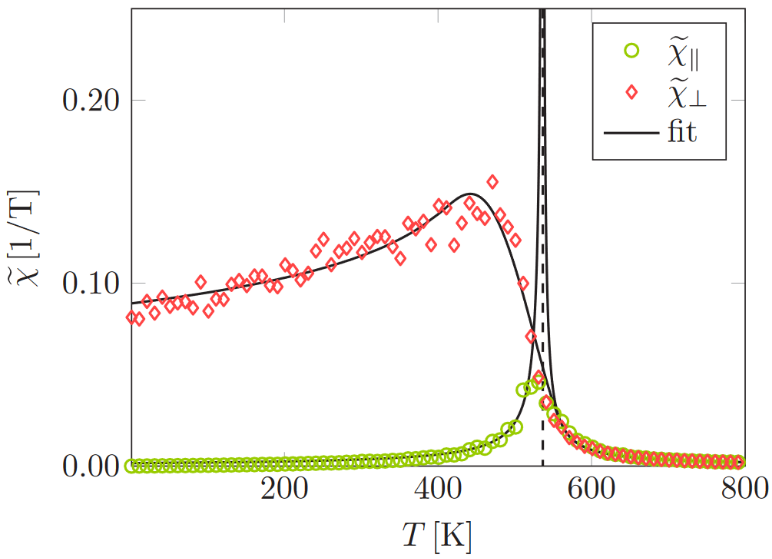

Figure 3.5: Transverse and parallel susceptibility over temperature for hard magnetic materials. The simulations are obtained with VAMPIRE [96]. The dashed black line indicates the Curie temperature. Picture taken from [114].

option to get all components of the susceptibility as output parameters from the simulations. It is defined as [96]

$$\chi_\alpha = \frac{\sum_i \mu_i}{k_\mathrm{B} T}\left(\langle m_\alpha^2\rangle - \langle m_\alpha\rangle^2\right) \tag{3.24}$$

with $\alpha = x, y, z, m$, m_α being the directional components of the magnetization in x, y and z as well as the longitudinal susceptibility χ_m. $\langle\cdot\rangle$ denotes the mean value. μ_i is the atomistic spin moment of spin i, k_B is the Boltzman constant and T is the temperature.

For hard magnetic materials, the behaviour of the components is different below and above the Curie temperature as seen in Figure 3.5. Below T_C, $\tilde{\chi}_\perp$ and $\tilde{\chi}_{||}$ behave differently, whereas they become equal above T_C because the grain becomes paramagnetic. The fitting curves of the components of the susceptibility are given by

$$\tilde{\chi}_{||} = \begin{cases} \frac{c_1}{T_\mathrm{C}-T} & T < T_\mathrm{C} \\ \frac{c_2}{T-T_\mathrm{C}} & T > T_\mathrm{C} \end{cases} \tag{3.25}$$

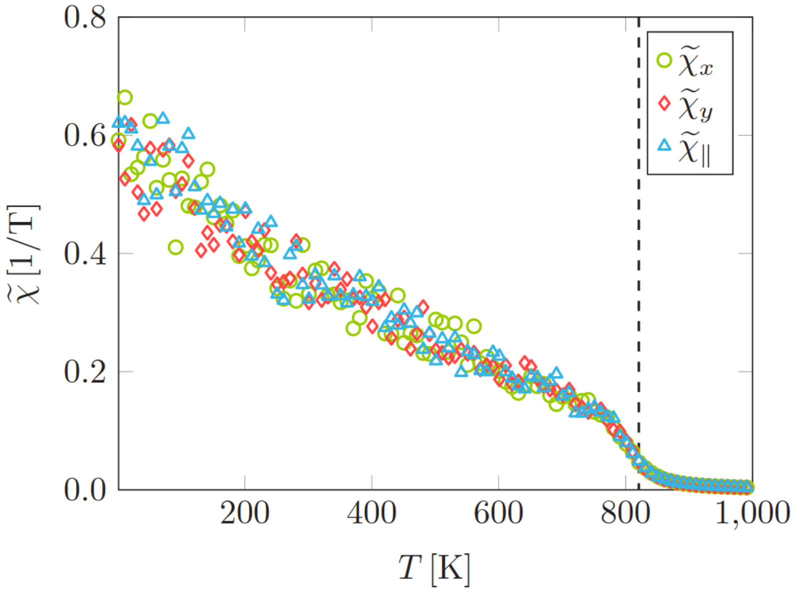

Figure 3.6: Susceptibility over temperature for soft magnetic materials. The simulations were performed with VAMPIRE. The dashed black line indicates T_C. Picture taken from [114].

and

$$\tilde{\chi}_\perp = \begin{cases} c_3 m_e^{c_4} & T << T_\mathrm{C} \\ \frac{c_5}{T - T_\mathrm{C}} & T > T_\mathrm{C}. \end{cases} \tag{3.26}$$

with the fitting parameters $c_1 - c_5$. The intermediate temperature range in which $\tilde{\chi}_\perp$ is not defined is fitted with a polynomial of fourth order.
For soft magnetic materials with small or no uniaxial anisotropy, a different approach has to be chosen since the grain may be superparamagnetic without the presence of an external field. Thus, as seen in Figure 3.6, all components of the susceptibility $\tilde{\chi}$ correspond quite well to each other. (The $z-$direction is the direction of the easy axis.) Since a perfect soft magnetic grain (not true for $K_1 > 0$) aligns very fast with the external field, the perpendicular susceptibility $\tilde{\chi}_\perp$ has to be set to infinity (in practical usage: very large compared to $\tilde{\chi}_{||}$).
$\tilde{\chi}_{||}$ cannot be extracted from the fluctuations of the magnetization's $z-$component as for the hard magnetic case. In eq. (3.21), $\tilde{\chi}_{||}$ ensures that the magnitude of the magnetization in the LLB equation remains in proximity to m_e. For the soft magnetic case, the parallel susceptibility can be derived from the variance of the magnetization

magnitude by

$$\tilde{\chi}_m = b \cdot \mathrm{Var}(|\boldsymbol{m}|) = b \cdot (\langle |\boldsymbol{m}|^2 \rangle - \langle |\boldsymbol{m}| \rangle^2) \tag{3.27}$$

This is done because $\mathrm{Var}(|\boldsymbol{m}|)$ shows a similar behavior to $\tilde{\chi}_{||}$ in the case of the hard magnetic material. The fluctuation of the magnetization is smaller than the fluctuation of the single components. Thus, the proportionality factor b is needed to scale the variance of the magnetization properly. The resulting χ_m is then fitted with eq. (3.25), which yields the parallel susceptibility $\chi_{||}$.

3.2.3 Model example: Switching probability phase diagram

One application of the coarse-grained LLB model is the computation of a so-called switching probability phase diagram. In a switching probability phase diagram, the probability of the magnetization of a grain to switch in the desired write direction is given depending on the position of the grain in a granular medium. The Gaussian heat pulse that is applied to the grain is given by

$$T(x, y, t) = T_{\mathrm{peak}}(y) \cdot e^{-\frac{x^2}{2\sigma^2}} + T_{\mathrm{min}} \tag{3.28}$$

with

$$\sigma = \frac{\mathrm{FWHM}}{\sqrt{8\ln(2)}}. \tag{3.29}$$

x is the down-track position, FWHM is the full width at half maximum and T_{min} is the ambient temperature. With

$$T_{\mathrm{peak}}(y) = (T_{\mathrm{write}} - T_{\mathrm{min}})e^{-\frac{y^2}{2\sigma^2}} + T_{\mathrm{min}}. \tag{3.30}$$

the off-track position y can be converted into a unique maximum applied temperature T_{peak} if T_{write} is fixed, and vice versa. In this form, the phase diagram contains even more information, since the maximum temperature of the heat pulse T_{write} in the center can be chose arbitrarily. The write head with the integrated heating system moves over a granular recording medium with velocity v and exerts a certain temperature to the grain corresponding to its position relative to the heating system. The grain is first heated up and then heated near or above the Curie temperature of the material (in the center of the bit). The writing process happens when the grain is cooling down. The direction in which the write field points during the cooling process determines the direction of the magnetization of the grain. Although the magnetization of the grain can only point in two different directions (↓ or ↑), there are also transition areas in which the probability of the magnetization to point in ↓ − or ↑ −direction is about 50%. Detailed information about the underlying mechanisms of the switching process is given in Section 3.4. With the coarse-grained LLB model, a phase diagram can be computed and in the further course be used for extracting important parameters from it (see Section 3.5.2) or to simulate a HAMR writing process on a granular recording medium (see Section 3.5.3). One example of a switching probability phase diagram computed with the coarse-grained LLB model is displayed in Figure 3.7.

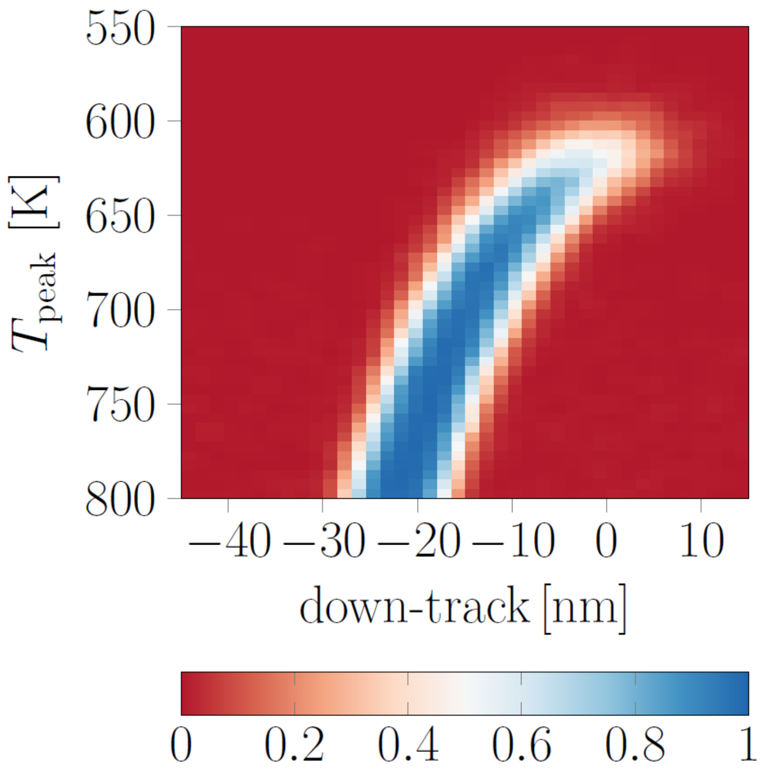

Figure 3.7: Switching probability phase diagram of a FePt-like hard magnetic grain computed with the coarse-grained LLB model.

3.3 Analytical Model of Phase Diagram

The computation of a locally resolved switching probability phase diagram is very time consuming with both the atomistic simulations and also the coarse-grained LLB model. To systematically investigate the influence of different parameters on the shape of a phase diagram and the signal-to-noise ratio, a more simple way to determine a phase diagram has to be introduced. For this reason Slanovc *et al* [119] developed a model which makes it computationally less costly to compute a switching probability phase diagram. The main source of this section is [119], others are explicitly mentioned.
In the model, different input parameters are used to determine the shape of the switching probability phase diagram. The model input parameters are

- down-track jitter σ_{down} in nm,
- off-track (T_{peak}) jitter σ_{off} in K,
- maximum switching probability P_{max},
- half maximum temperature F_{50} in K,
- bit length b in nm,
- curvature c in nm/K^2,
- position in $T_{\text{peak}}-$direction p_2 in K, and
- position in down-track direction p_3 in nm.

Note, the half maximum temperature F_{50} is not related to the full width at half maximum (FWHM) but denotes the temperature at which the switching probability of the grain is 50%. These eight parameters fully determine the shape of the phaseplot which can be seen in Figure 3.8. A model function $P(d, T_{\text{peak}})$ that gives the switching probability as a function of the down-track position d and the peak temperature T_{peak} is defined. Two help functions h_1 and h_2 which depend on the upper parameters are used for this purpose.
First the off-track and the down-track jitter are determined by fitting the switching probability curves at a fixed down-track position or a fixed peak temperature,

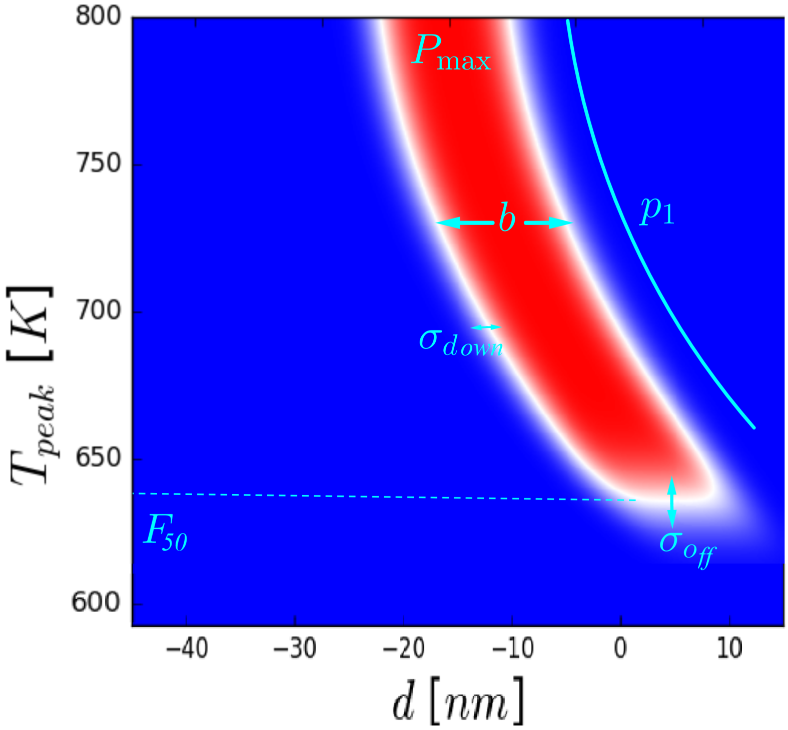

Figure 3.8: Visualization of the different input parameters that are used in the mathematical model of a phaseplot developed by Slanovc *et al* [119]. Picture taken from [119].

respectively, with a cummulative Gaussian distribution function

$$\Phi(x, \mu, \sigma) = \frac{1}{2}\left(1 + \text{erf}\left(\frac{x-\mu}{\sqrt{2}\sigma}\right)\right) \tag{3.31}$$

with

$$\lim_{x\to-\infty} \Phi(x) = 0, \lim_{x\to\infty} \Phi(x) = 1, \Phi(\mu) = \frac{1}{2} \tag{3.32}$$

where the slope σ gives the jitter. The procedure is explained in more detail in Section 3.5.2. h_1 is then defined by

$$h_1(d, T_{\text{peak}}) := \sqrt{P_{\text{max}}} \cdot \Phi(d, 0, \sigma_{\text{down}}) \cdot \Phi(T_{\text{peak}}, F_{50}, \sigma_{\text{off}}) \tag{3.33}$$

The graph of h_1 is plotted in Figure 3.9(a). $\sqrt{P_{\text{max}}}$ gives the maximum function value with

$$\lim_{d\to\infty, T_{\text{peak}}} h_1(d, T_{\text{peak}}) = \sqrt{P_{\text{max}}}. \tag{3.34}$$

Since the switching probability of the grain should decrease after a certain writing distance in down-track direction, a mirrored and shifted function h_1 has to be multiplied. This gives the second help function h_2 (see Figure 3.9(b))

$$h_2(d, T_{\text{peak}}) := h_1(d, T_{\text{peak}}) \cdot h_1(b - d, T_{\text{peak}}) \tag{3.35}$$

The maximum function value is P_{max}. However, P_{max} might never be reached since it only holds in the limit $b, T_{\text{peak}} \to \infty$. Until now, the model does not account for the curved shape of a realistic switching probability phase diagram. Thus h_2 has to be transformed into parabolic shape by

$$P(d, T_{\text{peak}}) := h_2(d - (c(T_{\text{peak}} - p_2)^2 - p_3), T_{\text{peak}}) \tag{3.36}$$

The final phaseplot can be seen in Figure 3.9(c). To get the desired more or less realistic basic parameters, a phaseplot derived from the LLB model is needed and the parameters are fitted with a least square fit. The resulting values are given in the relevant sections since they depend on the used material and write head parameters.

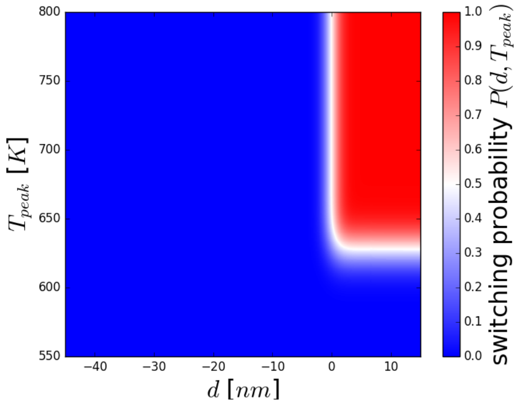

(a)

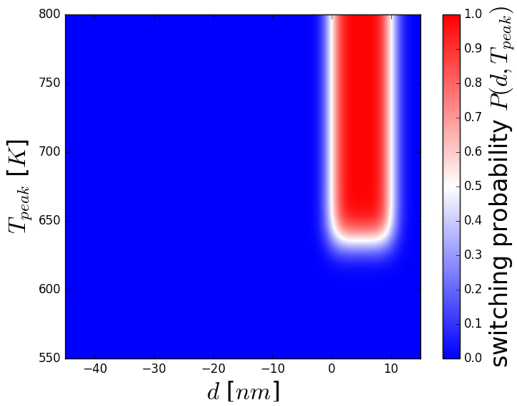

(b)

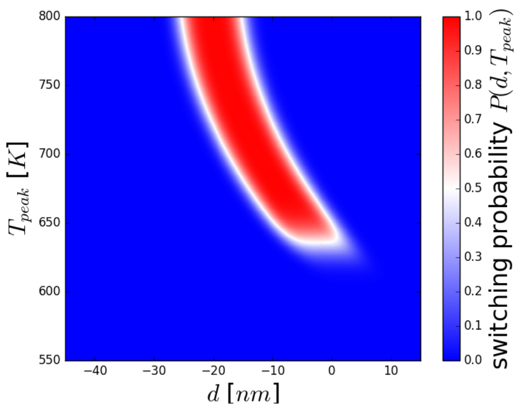

(c)

Figure 3.9: In (a) and (b) the graphs of the help functions h_1 and h_2 can be seen, respectively. In (c) the final curved model phaseplot is displayed. Picture taken from [119].

3.4 ERTW Model

The last model to compute the switching probability of a grain during HAMR is the effective recording time window (ERTW) model developed by Vogler *et al* [90]. Zhu and Li [40, 120] showed that there is a correlation between the noise power and the recording time window. The effective recording time window (ERTW) is defined by [90]

$$\mathrm{ERTW}_{\downarrow} = [t(T_{\mathrm{freeze}}), t(T_{\mathrm{C}})] \cap [t_{\downarrow,\mathrm{start}}, t_{\downarrow,\mathrm{final}}]. \tag{3.37}$$

The first term on the right hand side gives the time window in which the grains can be written in HAMR, namely in the temperature range between the Curie temperature T_{C} and the freezing temperature T_{freeze}. Above the Curie temperature, the particles get paramagnetic and the information is lost. At the freezing temperature the coercivity decreases below the given field strength such that the grains cannot be written any longer. To calculate the ERTW, the freezing temperature has to be estimated. For this reason, hysteresis loops are simulated for various temperatures. At each fixed temperature, 128 easy-axis loops are computed and H_{c} is extracted. Then, the temperature dependence of the coercive field $\mathrm{d}H_{\mathrm{c}}/\mathrm{d}T$ is determined. If the coercive field at a fixed temperature is lower than the write field, the temperature is a possible write temperature. Note, that to consider varying field magnitudes, the freezing temperature must be adjusted accordingly since it increases for decreasing field and vice versa.
The second term of eq. (3.37) gives the time window in which the field points in the desired write direction, which in the following is regarded as pointing downwards without loss of generality. A schematic depiction of the definition of the effective recording time window is shown in Figure 3.10. With the ERTW, the switching probability of a recording grain can be computed via [90]

$$p = \min\left(\frac{\mathrm{ERTW}_{\downarrow}}{\Theta_{\mathrm{ERTW}}}, 1\right)\left[1 - \min\left(\frac{\mathrm{ERTW}_{\uparrow}}{\Theta_{\mathrm{ERTW}}}, 1\right)\right]. \tag{3.38}$$

The first term gives the probability that a bit is written in write direction. Since the probability cannot exceed 1, the minimum between 1 and $\mathrm{ERTW}_{\downarrow}/\Theta_{\mathrm{ERTW}}$ is taken. Θ_{ERTW} is a threshold of the ERTW that gives the time that must be exceeded in order to be able to switch the grain in $\downarrow$ −direction with a probability of 100%. It depends mainly on the material of the recording grains and the field strength. It can

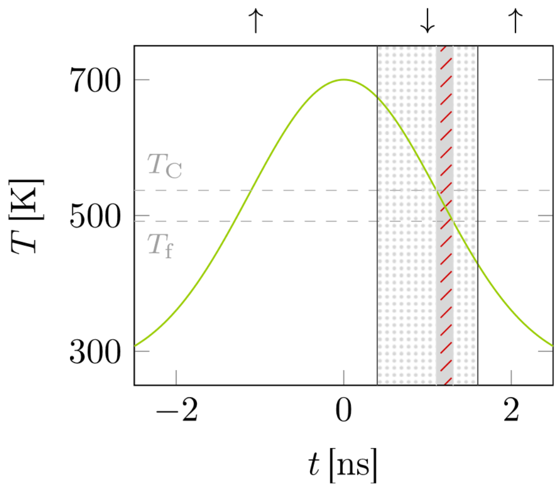

Figure 3.10: Depiction of the definition of the ERTW. The solid line in green shows the temperature pulse. T_C denotes the Curie temperature and T_f is the freezing temperature. The dotted area indicates the time window in which the external field points in write direction (↓). The grey solid area illustrates the times window in which the grain can be written. $ERTW_\downarrow$ is then defined as the overlap of the former two, shown with the red striped area. Picture taken from [90].

be determined as a fitting parameter to reproduce the results of the coarse-grained LLB model (Section 3.2) and is related to the mean switching time. The second term is the probability that a grain is not overwritten after it was already aligned in write direction. Together, p describes the joint probability to switch a bit in write direction and to not revert it afterwards. In Figure 3.11, a switching probability phase diagram is computed with the ERTW model for pure hard magnetic material. Note, that different material parameters are used in this switching probability phase diagram than in Figure 3.7. To explain the underlying mechanisms more extensively, four representative points in the switching probability phase diagram are investigated in more detailed.

For simplification, the recording temperature window is defined by

$$\tau_{\text{rec}} = t(T_C) - t(T_{\text{freeze}}) \tag{3.39}$$

and the recording field window in ↓ −direction by

$$\tau_\downarrow = t_{\downarrow,\text{final}} - t_{\downarrow,\text{start}} \tag{3.40}$$

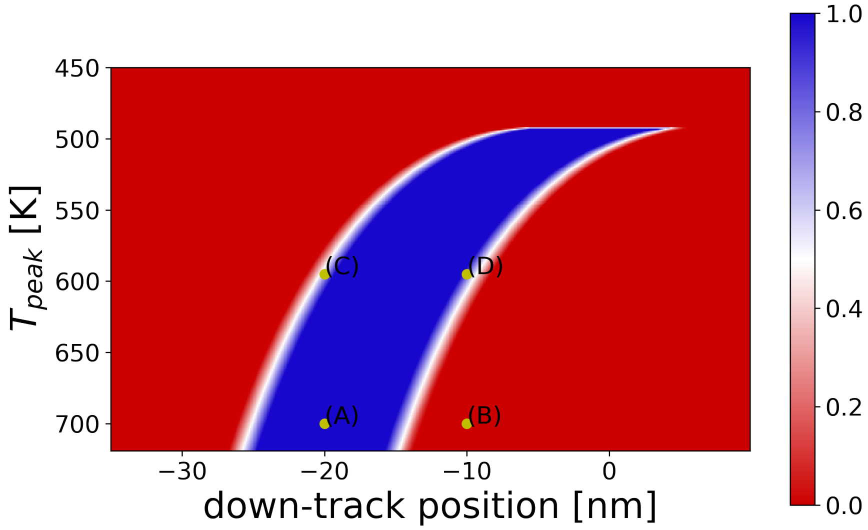

Figure 3.11: Switching probability phase diagram of pure hard magnetic material computed with the ERTW model. A detailed analysis of the ERTW corresponding to the marked yellow points (A)-(D) is depicted in Figure 3.12.

First, point (A) is considered. Here, the peak temperature is $T_{\text{peak}} = 700\,\text{K}$ and the down-track position is $x = -20\,\text{nm}$. As seen in Figure 3.12(A), the head field points in write (↓) direction during the whole time span $\tau_{\text{rec}} = 0.32\,\text{ns}$. Thus, ERTW↓$= \tau_{\text{rec}}$. With definition 3.38, the switching probability for point (A) is 100% with the ERTW model.

For point (B) with $T_{\text{peak}} = 700\,\text{K}$ and $x = -10\,\text{nm}$, there is no overlap of $\tau_{\text{rec}} = 0.32\,\text{ns}$ and $\tau_{\downarrow}$ (see Figure 3.12(B)). The field does not point in write direction while the grain can be written. Thus, the switching probability for point (B) is 0% according to the ERTW model.

In Figure 3.12(C), the ERTW for point (C) with $T_{\text{peak}} = 600\,\text{K}$ and $x = -20\,\text{nm}$ is displayed. The recording temperature window is $\tau_{\text{rec}} = 0.44\,\text{nm}$. During most of τ_{rec}, the head field points in ↑ −direction such that the magnetization of the grain is aligned antiparallel to the write direction. The effective recording time window is with $\text{ERTW}_{\downarrow} = 0.18\,\text{ns}$ smaller than $\Theta_{\text{ERTW}} = 0.2$ such that the grain does not switch with a probability of 100%. Thus, the switching probability of the grain at point (C) is with 64.7% clearly below 100% switching.

The last point is (D) with $T_{\text{peak}} = 600\,\text{K}$ and $x = -10\,\text{nm}$. Here, the head field

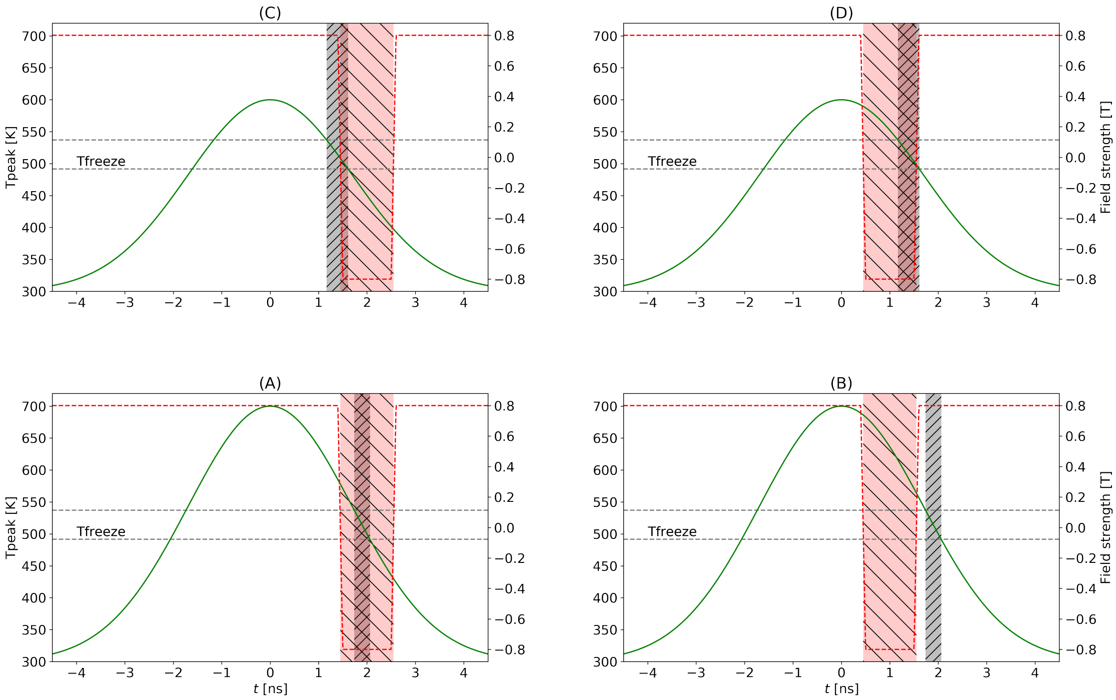

Figure 3.12: Illustrations of the ERTW for the marked points (A)-(D) in the phase diagram displayed in Figure 3.11. (A) $T_{\text{peak}} = 700\,\text{K}$ and $x = -20\,\text{nm}$, (B) $T_{\text{peak}} = 700\,\text{K}$ and $x = -10\,\text{nm}$, (C) $T_{\text{peak}} = 600\,\text{K}$ and $x = -20\,\text{nm}$ and (D) $T_{\text{peak}} = 600\,\text{K}$ and $x = -10\,\text{nm}$. The temperature pulse is shown in green and the field pulse is depicted in red. The grey area shows the time window τ_{rec} in which the grain can be written due to an appropriate temperature and the red area indicates the time window $\tau_{\downarrow}$ in which the head field points in write direction. The head velocity is assumed to be $v = 10\,\text{m/s}$.

points in writing direction during most of τ_{rec}, yielding to $\text{ERTW}_{\downarrow} = 0.36\,\text{ns}$. The field then switches into $\uparrow$ −direction and leads to $\text{ERTW}_{\uparrow} = 0.08\,\text{ns}$. This small effective recording time window $\text{ERTW}_{\uparrow}$ is enough to prevent the grain at point (D) from complete (100%) switching. The magnetization is able to reverse again to $\uparrow$ −direction, giving a switching probability in $\downarrow$ −direction of 85.3%.
With the ERTW it is possible to gain insight into basic noise mechanisms of heat-assisted magnetic recording. Figure 3.13 gives a comparison between switching probability phase diagrams calculated with the LLB model and the ERTW model.

3.5 HAMR Model

In the following, it is described how a HAMR process is simulated in the atomistic simulations as well as with the coarse-grained LLB model. All write head and material parameters are just generally introduced. The actual values of these parameters are specified in the respective chapter.
In the simulations, a cylindrical recording grain is considered with height h and diameter d. It can be interpreted as one grain of a state-of-the-art granular recording medium or one island of a patterned media design for ultra high density. A simple cubic crystal structure is used. The effective lattice parameter a and the exchange interaction J_{ij} are adjusted in order to lead to the experimentally obtained saturation magnetization and Curie temperature. [121, 122]. This results in a lattice parameter $a = 0.24\,\text{nm}$. In the simulations, only nearest neighbor exchange interactions between the atoms are included. A continuous laser pulse with Gaussian shape and the full width at half maximum FWHM is assumed in all simulations. The temperature profile of the heat pulse is given by

$$T(x,y,t) = (T_{\text{write}} - T_{\text{min}})e^{-\frac{(x-vt)^2+y^2}{2\sigma^2}} + T_{\text{min}} \tag{3.41}$$

$$= T_{\text{peak}}(y) \cdot e^{-\frac{(x-vt)^2}{2\sigma^2}} + T_{\text{min}} \tag{3.42}$$

with

$$\sigma = \frac{\text{FWHM}}{\sqrt{8\ln(2)}} \tag{3.43}$$

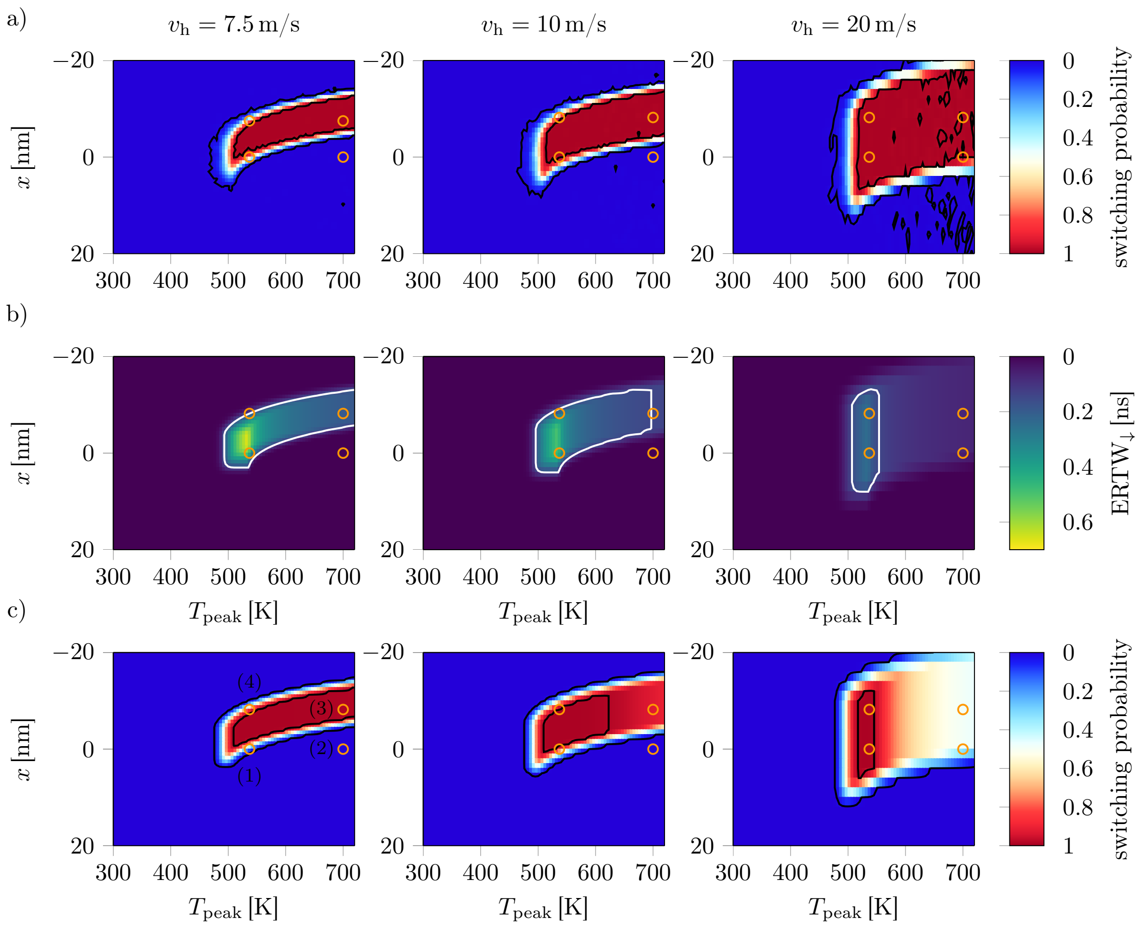

Figure 3.13: (a) Switching probability phase diagrams of pure hard magnetic grains for different head velocities v_h computed with the coarse-grained LLB model (see Section 3.2). (b) The effective recording time window $\mathrm{ERTW}_\downarrow$ for the same material is calculated. In (c) the switching probability is computed with eq. (3.38) based on the ERTW. The black contour lines in (a) and (c) indicate the transition between areas with switching probability less than 0.8% (red) and areas with switching probability higher than 99% (blue). The white contour lines in (b) show the lines with $\mathrm{ERTW}_\downarrow = \Theta_{\mathrm{ERTW}} = 0.15\,\mathrm{ns}$. Picture taken from [90].

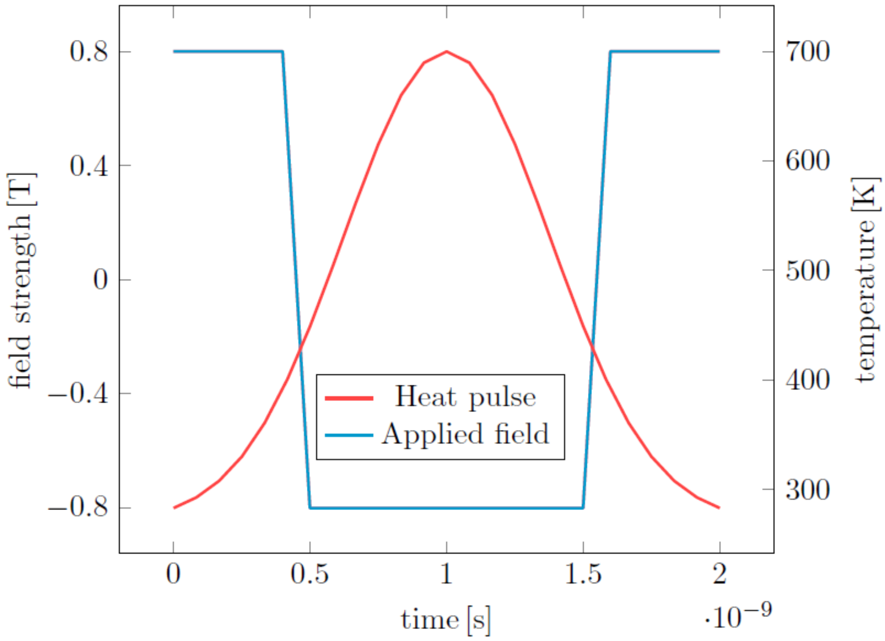

Figure 3.14: Schematic representation of a trapezoidal field and a Gaussian heat pulse for the HAMR simulations at down-track position $x = 0\,\mathrm{nm}$.

and

$$T_{\text{peak}}(y) = (T_{\text{write}} - T_{\text{min}})e^{-\frac{y^2}{2\sigma^2}} + T_{\text{min}}. \tag{3.44}$$

v is the speed of the write head. $x_0 = vt$ denotes the down-track position of the write head with respect to the center of the bit. x and y label the down-track and the off-track position of the grain, respectively. In the simulations both the down-track position x and the off-track position y are mutable. The origin of the heat pulse is at $x = 0\,\mathrm{nm}$ and $y = 0\,\mathrm{nm}$. The final temperature of all simulations is T_{min}. The applied field is modeled as a trapezoidal field with a special write frequency and a field rise and decay time of 0.1 ns. The field strength is assumed to be $+0.8\,\mathrm{T}$ and $-0.8\,\mathrm{T}$ in $z-$direction. The schematic position between the heat pulse and the trapezoidal field at down-track position $x = 0\,\mathrm{nm}$ can be seen in Figure 3.14. Initially, the magnetization of each grain points in $+z$-direction. The trapezoidal field tries to switch the magnetization of the grain from $+z$-direction to $-z$-direction. At the end of every simulation, it is evaluated if the bit has switched or not.

The values of the parameters used in the simulations are stated separately in each section.

3.5.1 Determination of the Phase Diagram

With the results of the HAMR simulations, the switching probability of the grain depending on the down-track position x and the off-track position y is calculated and a locally resolved switching probability phase diagrams can be determined (see also Section 3.2.3). In each phase point, i.e. for each $(x, y)-$combination 128 HAMR simulations are performed and the switching probability of these simulation trajectories is computed.
Solving the equation

$$T_{\text{peak}}(y) = (T_{\text{write}} - T_{\text{min}})e^{-\frac{y^2}{2\sigma^2}} + T_{\text{min}}. \tag{3.45}$$

(see eq. (3.42)) for y and fixing the write temperature T_{write}, gives an equation where one can compute an unique off-track position y for every peak temperature T_{peak}. Thus, the switching probability can also be given as a function of the down-track position x and the peak temperature T_{peak} that corresponds to y as shown in Figure 3.15. This model phase diagram is computed with the atomistic simulation program VAMPIRE [96].

3.5.2 Determination of Jitter and P_{max}

Both the off-track and the down-track jitter can be extracted from the switching probability phase diagram. The transition in off-track direction at a specific down-track position can be obtained by making a vertical cut in the phase diagram. For example, the off-track transition at down-track position $x = 0\,\text{nm}$ is marked by the dashed vertical line at $x = 0\,\text{nm}$ in Figure 3.15. On the other hand, the down-track transition is marked by a cut in the horizontal direction at a specific off-track position which is depicted by the corresponding peak temperature. For a peak temperature $T_{\text{peak}} = 700\,\text{K}$, the switching probability curve in off-track direction at down-track position $x = 0\,\text{nm}$ and the transition curve in down-track direction at off-track position $y = 0\,\text{nm}$ ($T_{\text{peak}} = T_{\text{write}}$) can be seen in Figure 3.16 (a) and (b). In order to compute the jitter of the material configurations, the switching probability curves are fitted with a Gaussian cumulative distribution function

$$\Phi_{\mu,\sigma^2} = \frac{1}{2}\left(1 + \text{erf}\left(\frac{x-\mu}{\sqrt{2\sigma^2}}\right)\right) \cdot p \tag{3.46}$$

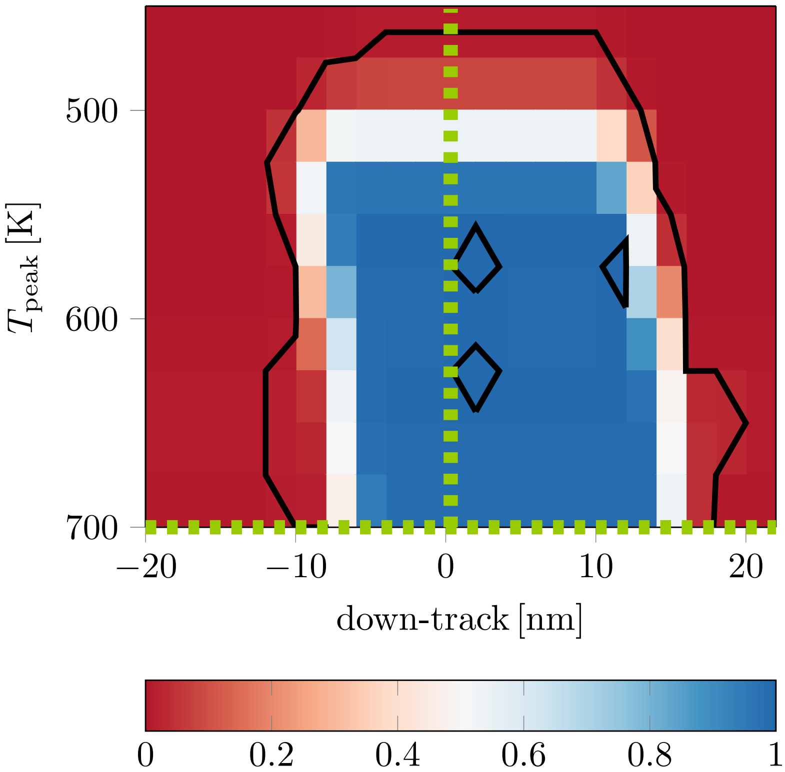

Figure 3.15: Switching probability phase diagram of a pure FePt-like hard magnetic grain taken from Chapter 6. The dashed lines mark the switching probability curves shown in Figure 3.16.

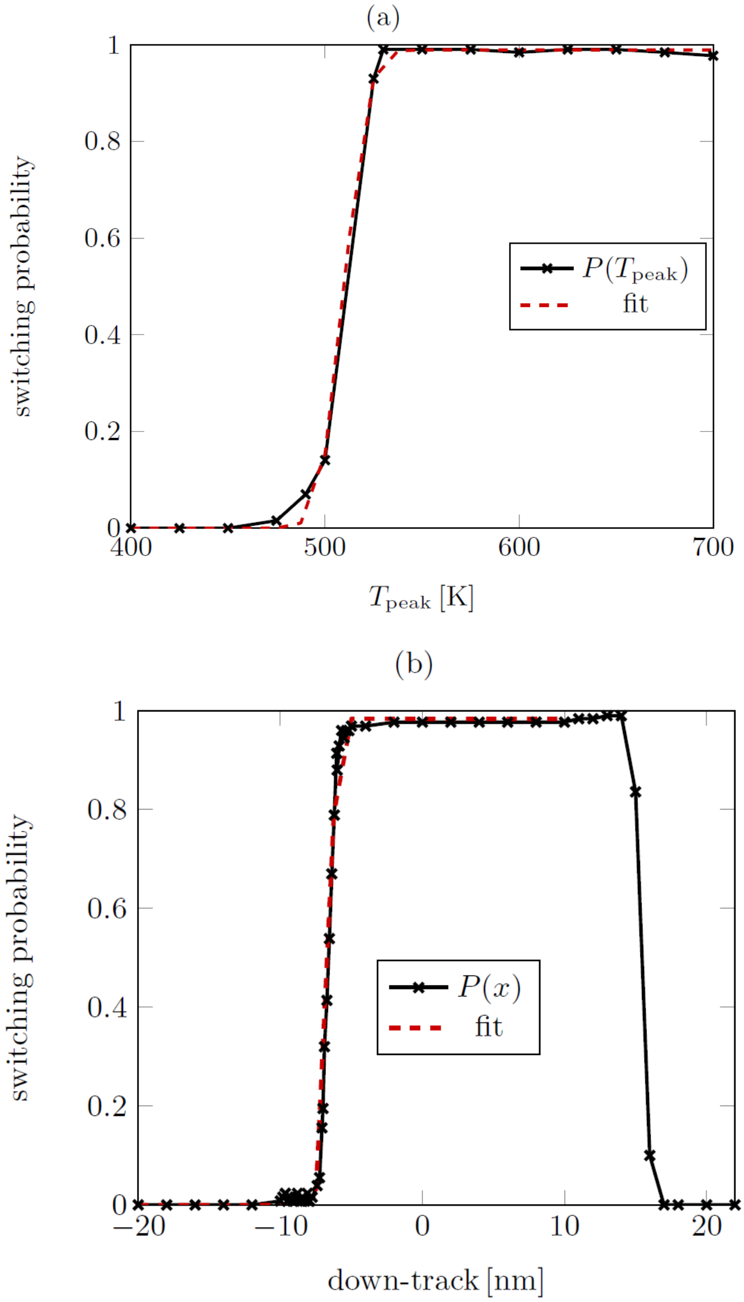

Figure 3.16: Switching probability curves of an FePt-like hard magnetic grain taken from Chapter 6. (a) $P(T_{\mathrm{peak}})$ which corresponds to off-track switching probability curve for a fixed down-track position $x = 0\,\mathrm{nm}$. (b) Down-track switching probability curve $P(x)$ for a fixed off-track position $y = 0\,\mathrm{nm}$ and the peak temperature $T_{\mathrm{peak}} = 700\,\mathrm{K}$.

with

$$\operatorname{erf}(x) = \frac{2}{\sqrt{\pi}} \int_0^x e^{-\tau^2} d\tau, \tag{3.47}$$

where the mean value μ, the standard deviation σ and the mean maximum switching probability $p \in [0, 1]$ are the fitting parameters. The standard deviation σ, which determines the steepness of the transition function, is a measure for the transition jitter and thus for the achievable maximum areal density of a recording medium. The fitting parameter p is a measure for the average switching probability at the bit center. Often, only the down-track jitter σ_{down} is of interest and the off-track jitter σ_{off} is neglected. Note, that the calculated down-track jitter values σ_{down} do not fully describe the write jitter. The so-called $a-$parameter is given by

$$a = \sqrt{\sigma_{\text{down}}^2 + \sigma_{\text{g}}^2} \tag{3.48}$$

where σ_{g} is a grain-size-dependent jitter contribution [123]. The write jitter can then be calculated by

$$\sigma_{\text{write}} \approx a\sqrt{\frac{S}{W}} \tag{3.49}$$

where W is the reader width and $S = D + B$ is the grain size, i.e. the sum of the grain diameter D and the nonmagnetic boundary B [3, 119].

3.5.3 Determination of the Signal-to-noise Ratio (SNR)

In magnetic recording, the quality of a written bit sequence can be described by the signal-to-noise ratio [40]. The SNR$= P_{\text{signal}}/P_{\text{noise}}$, gives the power of the signal over the power of the background noise. The media SNR depends on various parameters. There holds [3]

$$\text{SNR} \propto \left(\frac{b}{a}\right)^2 \left(\frac{T_{50}}{b}\right) \left(\frac{W}{S}\right) \tag{3.50}$$

where b is the bit length, a is the $a-$parameter, T_{50} denotes the read-back pulse width, W is the reader width and S labels the grain size ($S = D + B$, where D is the diameter of the grain and B is the nonmagnetic boundary). B is a fixed size (1 nm) which means that the grain size S depends only on the grain diameter D. The transition parameter a defined above (see Section 3.5.2) comes from the down-track jitter and a grain size dependent jitter contribution σ_{g}. σ_{g} is given by

$$\sigma_{\mathrm{g}} = \frac{S}{\sqrt{12}} \tag{3.51}$$

with the grain size S as defined above.
In this work, the following procedure is used to determine the SNR. The information for the determination process of the SNR is mainly taken from [119], others are explicitly mentioned.

Writing

First, the information has to be written onto the granular media. To do this, the received switching probability phase diagram from Section 3.5.1 is mapped onto granular recording media. The switching probability of each cylindrical recording grain is determined from the phase diagram according to the position of the grain. A spatially varying temperature within the single grains is neglected such that the whole grain is exposed to the same Gaussian pulse. The stray field is only considered by adding a T_{C} variation and not directly taken into account [119].
50 different initially randomly magnetized granular media with different grain structure are considered. The bit series that is written to the media is the following

$$(-1\ +1\ +1)\ -1\ -1\ -1\ -1\ -1\ +1\ +1\ +1\ -1\ -1\ +1\ -1\ -1\ -1\ +1$$
$$-1\ +1\ -1\ +1\ +1\ +1\ +1\ -1\ +1\ +1\ -1\ +1\ -1\ -1\ +1\ +1\,(-1\ -1\ -1).$$

-1 and $+1$ indicate bits that are pointing in $-z-$ and $+z-$direction, respectively. The bits in the brackets are used for padding. The desired bit series is given by the 31 bits in between. The magnetization direction of every grain is determined by a random number generator, according to the switching probability in the phase diagram. A uniformly distributed pseudo random number $r \in [0, 1)$ is created. If the switching probability $p > r$ then the magnetization is aligned according to the direction of the applied field. Otherwise, the magnetization of the grain remains unchanged. This process is repeated for polarity change of the magnetic field from the left of the medium to the right to simulate a real writing process. In Figure 3.17, both the randomly initialized and the written medium are displayed. The total dimensions of the medium are 500 nm×60 nm with a thickness of 8 nm.

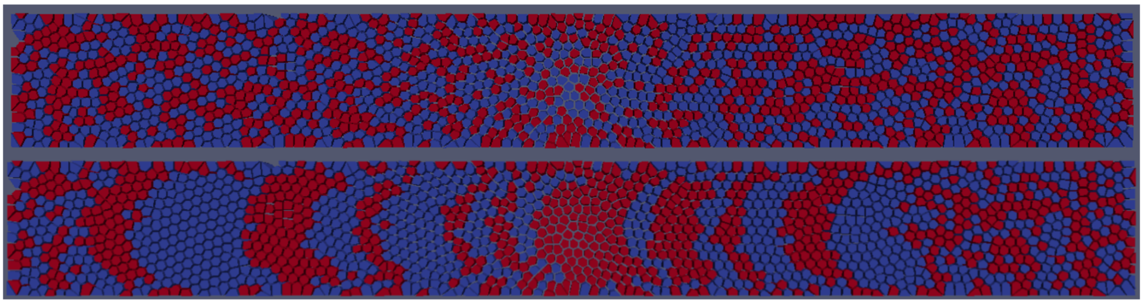

Figure 3.17: (Top): Randomly initialized granular recording medium. The grains have a diameter of 4 nm and the non-magnetic gap between the grains is 1 nm. Red and blue grains are pointing in $+z-$ and $-z-$direction, respectively. (Bottom): Granular medium after the simulated writing process. Picture taken from [119].

Reading

The reader is modeled with the help of a sensitivity function H as in [124–126]. In the reciprocity principle used in this work, the sensitivity function corresponds to the magnetic field produced by a test coil at the read head and can be determined from simulations with an finite element code. In Figure 3.18(a), the contour plot of the sensitivity function for a reader width of 30.13 nm and a reader resolution of 13.26 nm can be seen. With the reciprocity principle, the integral

$$V(x, y, z) = c_1 \int H(x + x', y, z) \cdot M(x, y, z) \; dx \, dy \, dz \tag{3.52}$$

over the sensitivity function and the magnetization M of the medium with a reader dependent constant c_1 gives the voltage of the reader. Due to the strong uniaxial anisotropy of the grains, the integral simplifies to an areal integral

$$V = \tilde{c_1} \int H_z(x + x', y) \cdot M_z(x, y) \; dx \, dy \tag{3.53}$$

where the constant $\tilde{c_1}$ does not influence the SNR value. It can thus be computed via a discrete sum over the data points multiplied with $+1, -1$ and 0 depending on whether the point is inside a grain with magnetization in $-z-$direction or $+z-$direction or whether there is a grain boundary. The sensitivity function is moved across the medium in steps of 0.5 nm in down-track direction. The result is a read-back signal of the whole written bit information. One example is shown in Figure 3.18(b).

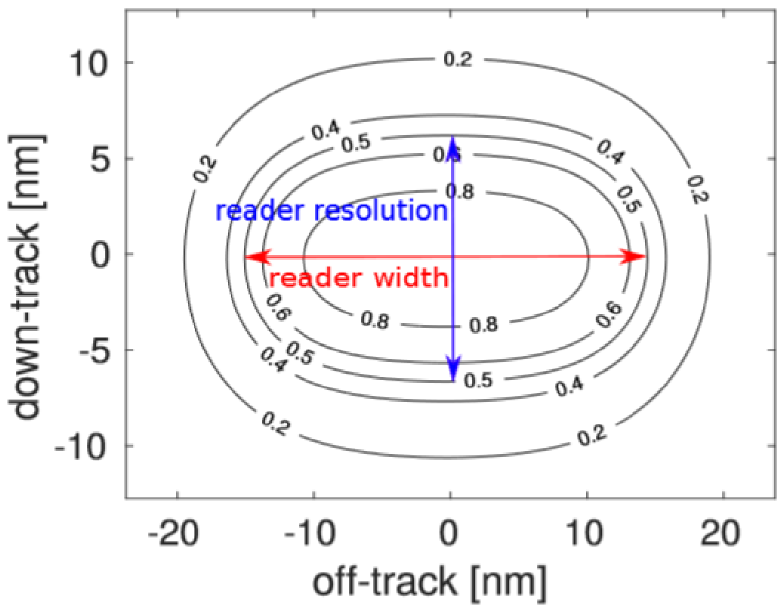

(a)

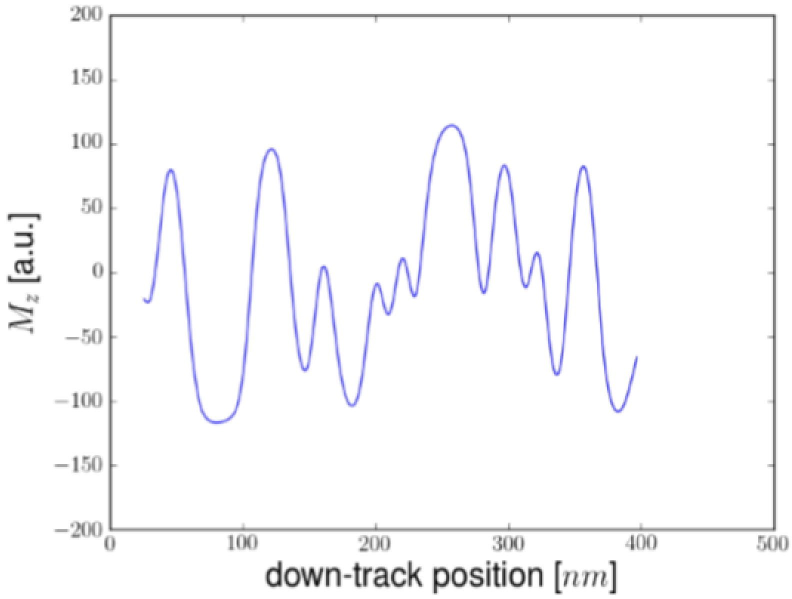

(b)

Figure 3.18: (a) Contour plot of a sensitivity function. The data point resolution in off-track and down-track direction is 0.5 nm. The reader width and reader resolution are the width between the points with 50% sensitivity in off-track and down-track direction, respectively. (b) Read-back signal determined with the sensitivity function in (a) for the written medium in Figure 3.17. Picture taken from [119].

SNR Calculation

To calculate the SNR, the read-back signal $R(x)$ where x is the down-track position is determined from 50 media with different grain structures that are initially randomly magnetized. One example of the 50 read-back signals can be seen in Figure 3.19. Generally, from the read-back signal of a bit pattern beween the down-track positions x_{start} and x_{end}, the signal power (SP) is calculated from the expectation value $\mathbb{E}$ of $R(x)$ by [40]

$$\text{SP} = \frac{1}{b} \int_{x_{\text{start}}}^{x_{\text{end}}} \mathbb{E}[R(x)]^2 dx \tag{3.54}$$

where b is the bit length.
The noise power (NP) is given by the variance of the read-back signal

$$\text{NP} = \frac{1}{b} \int_{x_{\text{start}}}^{x_{\text{end}}} \mathbb{V}[R(x)] dx \tag{3.55}$$

where $\mathbb{V}[R(x)]$ is the variance of the read-back signal. The SNR can then be determined via

$$\text{SNR} = \frac{\text{SP}}{\text{NP}}. \tag{3.56}$$

In this work, the SNR is calculated with a SNR calculator provided by SEAGATE [127]. The resulting SNR value is given in dB (SNR_{dB}). Principally, there holds $\text{SNR}_{\text{dB}} = 10 \log_{10}(\text{SNR})$. In the further course, the SNR_{dB} is simply called SNR unless it is explicitly noted differently.

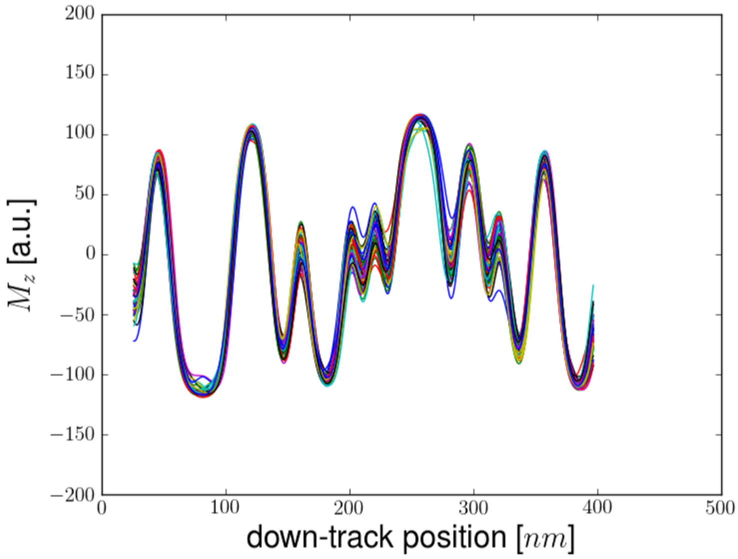

Figure 3.19: Read-back signal of a bit pattern written with the same phase diagram on 50 different granular media. The curves are used for the SNR calculation of the signal. Picture taken from [119].

Chapter 4

Influence of Recording Parameters on the Signal-to-noise Ratio

Parts of this chapter have been previously published in [128] and have been reproduced with permission of the coauthors and in accordance with the publisher's policy. Content that was not generated by the author of this thesis is explicitly denoted.

4.1 Introduction

As mentioned in Section 3.5.3, the signal-to-noise ratio is a good indicator for the quality of written bits in magnetic recording. High SNR values are required to provide a good signal and thus allow to reliably read the written information. A priori it is not clear which write head parameters and which material parameters have the strongest influence on the SNR. In this work, two sets of material and write head parameters are considered. The first set of parameters, shown in Table 4.2, is taken from former studies on heat-assisted magnetic recording [60, 89]. It is referred to as *parameter set 1*. The second set of parameters is a collection of recording parameters according to the Advanced Storage Research Consortium [19] and is shown in Table 4.1. The ASRC is a collaboration of different research groups and companies to research and develop future directions on new key technologies like HAMR or bit-patterned media [19]. These parameters are in the further course called *ASRC parameters*. Calculating the SNR for these two parameter sets for grains with diameter $d = 5\,\mathrm{nm}$ shows a difference of the SNR values of about $8.25\,\mathrm{dB}$. Thus, it is of great interest to understand the role of each parameter. In this section, the influence of the different parameters on the SNR is investigated. The *ASRC parameters* (in Table 4.1) are assumed to be the initial parameters. First, just single parameters are changed to get a better understanding of which of them are important or not, with regard to the SNR. Since the simulations show that an enhancement of the damping constant α

improves the SNR significantly, further simulations with varying α for two different grain diameters $d = 5$ nm and $d = 7$ nm are performed.

material					write head		
Curie temp. T_C [K]	Damping α	Uniaxial anisotropy k_u [J/atom]	J_{ij} [J/link]	μ_s [μ_B]	v [m/s]	field duration (fd) [ns]	FWHM [nm]
693.5	0.02	9.124×10^{-23}	6.72×10^{-21}	1.6	15	0.57	60

Table 4.1: Material and write head parameters of an FePt-like hard magnetic granular recording medium accoring to the Advanced Storage Research Consortium [19].

material					write head		
Curie temp. T_C [K]	Damping α	Uniaxial anisotropy k_u [J/atom]	J_{ij} [J/link]	μ_s [μ_B]	v [m/s]	field duration (fd) [ns]	FWHM [nm]
536.6	0.1	9.12×10^{-23}	5.17×10^{-21}	1.7	20	1.0	20

Table 4.2: Material and write head parameters of an FePt-like hard magnetic granular recording medium that were used in former works [60, 89, 129].

4.2 Modeling Parameters

The initial write head and material parameters in this section are the *ASRC parameters* which can be seen in Table 4.1. The model from Section 3.3 is taken to investigate the influence of the different parameters on the switching probability of recording grains. The reader width is 30.13 nm and the reader resolution in down-track direction is 13.26 nm. Both, the reader width and resolution are assumed to be constant in the simulations. Slanovc *et al* showed that the maximum switching probability $P_{\max}$ and the down-track jitter σ_{down} are the input parameters with the strongest influence on the SNR [119]. Additionally, the bit length b also has a strong influence on the SNR. In the further course of this section, an equation to include the bit length to the SNR calculations is shown. Thus, the bit length can be assumed constant during the SNR determination. The transition curvature c did not show strong influence on the SNR for the used reader model and the off-track jitter σ_{off} as well as the half maximum temperature F_{50} are neglectable since the reader width is with 30.13 nm smaller than the track width with 44.34 nm and thus does not sense the off-track jitter and F_{50}. p_2 and p_3 only shift the bit pattern and can thus be fixed for comparability. With these considerations, it is reasonable to fix the input parameters, except for the maximum switching probability $P_{\max}$ and the down-track jitter σ_{down}. The fixed input parameters are determined by a least square fit from a switching probability phase diagram computed with a coarse-grained LLB model [114] for pure hard magnetic grains with material parameters given in Table 4.1. The fitting parameters are summarized in Table 4.3 for grain diameters $d = 5$ nm and $d = 7$ nm. Throughout this section, the fitting parameters are kept constant to be able to compare the results with each other. Only the bit length is adjusted in the course of the work. The σ_{down} and $P_{\max}$ values for each material compositions are determined from atomistic simulations with VAMPIRE with the procedure explained in Section 3.5.2.

	grain size	
	5 nm	7 nm
σ_{off} [K]	22.5	14.4
$P_{\max}$	0.995	0.997
F_{50} [K]	602	628
b [nm]	10.2	10.2
c [10^{-4} nm/K^2]	3.88	4.89
p_2 [K]	839	830
p_3 [nm]	27.5	25.8

Table 4.3: Reference parameters that are evaluated via least square fit of the simulated phase diagrams for grain sizes 5 nm and 7 nm. Details of the parameters can be found in [119]. σ_{down} and $P_{\max}$ are variable and determined for each combination of material and write head parameters.

4.3 Results

4.3.1 Influence of Write Head Parameters

First, the SNR is determined for the *ASRC parameters*. The track width in the simulations is 44.34 nm. As displayed in Table 4.3, a bit length $b = 10.2$ nm is assumed in the SNR calculation since this is the bit length resulting from the *ASRC parameters*. However, when changing the write head parameters, it is necessary to take into account the change of the bit length b due to

$$b = v \cdot (\text{fd} + \text{rdt}). \tag{4.1}$$

where v is the head velocity, fd is the field duration and rdt$= 0.1\,$ns is the field rise and decay time. For that reason, the bit length for *parameter set 1* is 22 nm. Slanovc *et al* [119] already studied the influence of the bit length on the SNR. To write a bit pattern with a larger bit length ($b > 12\,$nm) the simulations of new granular media are required. This is computationally very expensive. Thus, a different approach is needed to qualitatively investigate the influence of the bit length. For the SNR with $\text{SNR}_\text{dB} = 10\log_{10}(\text{SNR})$, there holds [3]

$$\text{SNR} \propto \left(\frac{b}{a}\right)^2 \left(\frac{T_{50}}{b}\right)\left(\frac{W}{S}\right) \tag{4.2}$$

with the bit length b and the read-back pulse width T_{50} which is proportional to the reader resolution in down-track direction. To determine the read-back pulse with T_{50}, the reader response of an isolated transition is differentiated and the pulse width at 50% amplitude of the differentiated signal gives T_{50} [127]. The ratio T_{50}/b is called user bit density and is usually kept constant [3]. Further, the reader width W and the grain size S are constant. Since the aim is to qualitatively describe the SNR for a bit length b_2 from SNR calculations with a bit length b_1, the $a-$parameter a is also assumed to be constant. The SNR_dB for a different bit length b_2 can then be calculated by

$$\begin{aligned} &\text{SNR}_\text{dB}(b_2) - \text{SNR}_\text{dB}(b_1) \\ &= 10\log_{10}(\text{SNR}(b_2)) - 10\log_{10}(\text{SNR}(b_1)) \\ &= 10\log_{10}(b_2^2) - 10\log_{10}(b_1^2) = 20\log_{10}\left(\frac{b_2}{b_1}\right) \end{aligned} \tag{4.3}$$

since all other parameters are the same for both bit lengths. Thus, one can compute the SNR_dB value for a varied bit length b_2 via the SNR_dB of the bit length b_1 by

$$\text{SNR}_\text{dB}(b_2) = \text{SNR}_\text{dB}(b_1) + 20\log_{10}\left(\frac{b_2}{b_1}\right). \tag{4.4}$$

In Figure 4.1, the good qualitative agreement between the actual SNR values computed with the model from Section 3.3 for a grain with diameters $d = 5\,$nm and

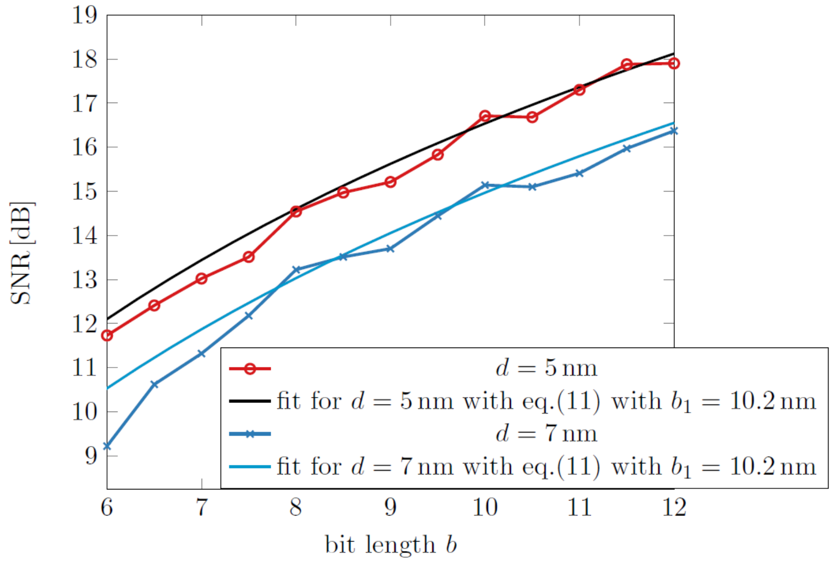

Figure 4.1: SNR over bit length for grains with diameters $d = 5\,\mathrm{nm}$ and $d = 7\,\mathrm{nm}$. The solid curves are computed by eq. (4.4) for a fixed initial bit length $b_1 = 10.2\,\mathrm{nm}$. The SNR values over the bit length are taken from Slanovc *et al* [119].

$d = 7\,\mathrm{nm}$ taken from Slanovc *et al* [119] and eq. (4.4) for a varying bit length b_2 and $b_1 = 10.2\,\mathrm{nm}$ can be seen. The write head parameters that are changed are the field duration, the full width at half maximum and the head velocity. To see if in the case of a change of the field duration and the head velocity, an increase of the SNR results from the change of the write parameter or only from the change of the bit length, two parameter variations are simulated for these parameters. In one variation, the respective parameter (head velocity or field duration) is changed and with it also the bit length. In the other variation both the head velocity and the field duration are changed in a way such that the bit length is kept constant. The $P(x)-$curves are calculated with VAMPIRE at $T_{\mathrm{peak}} = 760\,\mathrm{K}$ and P_{max} and σ_{down} are computed according to Section 3.5.2. The SNR is then determined. The results are shown in Table 4.4. It can be seen that the change of the write head parameters do not improve the SNR if the bit length is kept constant but slightly reduce the SNR. However, if the bit length is enlarged, the SNR is enhanced too. If the write head parameters are all set to that of *parameter set 1* and are compared to the *ASRC parameters*, the difference between the SNR values is about 6.14 dB which is entirely due to the variation of the bit length.

Varied parameter	Original parameter	b [nm]	$P_{\max}$	σ_{down} [nm]	SNR [dB]
—	ASRC	10.2	0.974	0.95	17.51
fd = 1 ns	fd= 0.57 ns	16.5	0.974	0.986	21.62
fd = 1 ns, $v = 10$ m/s	fd= 0.57 ns, $v = 15$ m/s	10.2	0.963	0.703	17.35
FWHM=20 nm	FWHM=60 nm	10.2	0.927	0.732	15.92
$v = 20$ m/s	$v = 15$ m/s	11.6	0.953	1.155	17.38
$v = 20$ m/s, fd= 0.4 ns	$v = 15$ m/s, fd= 0.57 ns	10.2	0.938	0.902	16.15
Parameter set 1, ASRC material	—	22	0.914	0.763	22.04

Table 4.4: Resulting $P_{\max}$, σ_{down} and SNR values from parameter variations of the write head. The original parameters in column 2 are given by the ASRC (see Table 4.1). In each simulation one value is varied as indicated by the varied value in column 1. b denotes the bit length, fd the field duration, v the head velocity and FWHM the full width at half maximum.

4.3.2 Influence of Material Parameters

As a next step, the simulations with changing material parameters are performed. Here, the bit length is 10.2 nm for all variations, the track width is again 44.34 nm. First, a material with the *ASRC parameters* is considered. In all further simulations, one parameter is changed to the values of *parameter set 1* as indicated in Table 4.5. The $P(x)-$curves are again calculated at $T_{\text{peak}} = 760\,\text{K}$, except for those cases where a different peak temperature is specified in the table. In these cases the Curie temperature is different due to the relation

$$J_{ij} = \frac{3k_{\text{B}}T_{\text{C}}}{\epsilon z}, \tag{4.5}$$

where k_{B} is the Boltzmann constant, z is the number of nearest neighbors and ϵ is a correction factor from the mean-field expression which is approximately 0.86 [96]. The curves are fitted according to Section 3.5.2 and the SNR is determined as in Section 3.5.3. The resulting fitting and SNR values are shown in Table 4.5. It is visible that for most material parameters the changed value increases the SNR about $0.5-1.0$ dB. The highest SNR increase by about 2.26 dB can be achieved for a change of the damping constant from $\alpha = 0.02$ to $\alpha = 0.1$. When comparing the new ASRC material to the *parameter set 1*, it shows that the SNR increases by about 2.3 dB which suggests that the SNR increase is caused solely by the change of the damping constant.

Varied parameter	Original parameter	b [nm]	$P_{\max}$	σ_{down} [nm]	SNR [dB]
—	ASRC	10.2	0.974	0.95	17.51
$h = 10\,\text{nm}$	$h = 8\,\text{nm}$	10.2	0.988	0.92	18.42
$\mu = 1.7\,\mu_\text{B}$	$\mu = 1.6\,\mu_\text{B}$	10.2	0.984	1.01	17.96
$\alpha = 0.1$	$\alpha = 0.02$	10.2	1.0	0.688	19.77
$J_{ij} = 5.18 \times 10^{-21}$ J/link, $T_{\text{peak}} = 600\,\text{K}$	$J_{ij} = 6.72 \times 10^{-21}$ J/link, $T_{\text{peak}} = 760\,\text{K}$	10.2	0.986	1.05	18.0
Parameter set 1, $T_{\text{peak}} = 600\,\text{K}$	—	10.2	1.0	0.67	19.81

Table 4.5: Resulting $P_{\max}$, σ_{down} and SNR values from several material parameter variations. The original parameters in column 2 are given by the ASRC (see Table 4.1). In each simulation one value is varied as indicated by the varied value in column 1. b denotes the bit length, h the height of the grain and μ the atomistic spin moment. α denotes the damping constant and J_{ij} the exchange interaction.

4.3.3 SNR Dependency on Damping

Based on the findings of Section 4.3.2, the influence of the damping constant on the signal-to-noise ratio is studied more systematically. The damping constant is varied from $\alpha = 0.01$ to $\alpha = 0.5$ for two different grain sizes $d = 5\,\text{nm}$ and $d = 7\,\text{nm}$. All other parameters are taken from Table 4.1. The bit length in the simulations is 10.2 nm and the track width is 44.34 nm. The down-track switching probability curves are computed with VAMPIRE [96] at $T_{\text{peak}} = 760\,\text{K}$ and fitted according to Section 3.5.2. In Figure 4.2 the SNR over the damping constants for both grain sizes is visible. Note that the SNR is proportional to the number of grains, meaning that the number of grains per bit has to be kept constant to determine a nearly constant SNR [42]. However, since the dimensions of the granular media used for the writing and reading process are fixed, less grains form one bit for $d = 7\,\text{nm}$. Thus, the SNR values for the larger grain size are generally smaller than for the smaller grains.

The results show that changing the damping constant from $\alpha = 0.01$ to $\alpha = 0.02$ already increases the SNR by 3.66 dB for 5 nm-grains. For $d = 7\,\text{nm}$, the SNR gain is 1.65 dB. For 5 nm-grains, damping constants $\alpha \geq 0.1$ lead to the best results with a total improvement of 6 dB compared to $\alpha = 0.01$. Surprisingly, enhancing the damping constant beyond 0.1 does not show any further improvement, the SNR saturates. This behavior is the same for the 7 nm-grains. However, the total betterment of the SNR is only 2.24 for the larger grains. The SNR saturation results from the fact that $P_{\max} = 1$ for $\alpha \geq 0.1$. Simultaneously, the down-track jitter σ_{down} varies only little for $\alpha \geq 0.1$ (see Table 4.6) such that it does not alter the SNR. The correlation between the SNR and the maximum switching probability $P_{\max}$ is shown in Figure 4.3.

It shows that the fitted SNR curve reproduces the $P_{\max}$ data very well.
By further studying the switching dynamics of a 5 nm-grain, one can show that the assumed pulse duration of the heat pulse and the applied field strength are crucial for the saturation of the SNR. In Figure 4.4, it is displayed how the duration of the heat pulse influences the maximum switching probability and with it the SNR. During the duration of the heat pulse the field is considered to constantly point in $-z$-direction. The results demonstrate that $P_{\max}$ does not saturate for small pulse durations. If longer pulse durations ≥ 0.5 ns are assumed, a $P_{\max}$ saturation can be seen. A similar effect can be seen for a change of the field strength when the pulse duration is assumed to be 0.5 ns (see Figure 4.5). For a small head field with a strength of 0.5 T, $P_{\max}$ shows no saturation whereas it does for larger head fields. From the simulations with varying duration of the heat pulse and field strength, it can also be seen that the SNR can be improved for smaller damping constants if the duration of the heat pulse is increased due to a smaller head velocity or the field strength is enhanced.

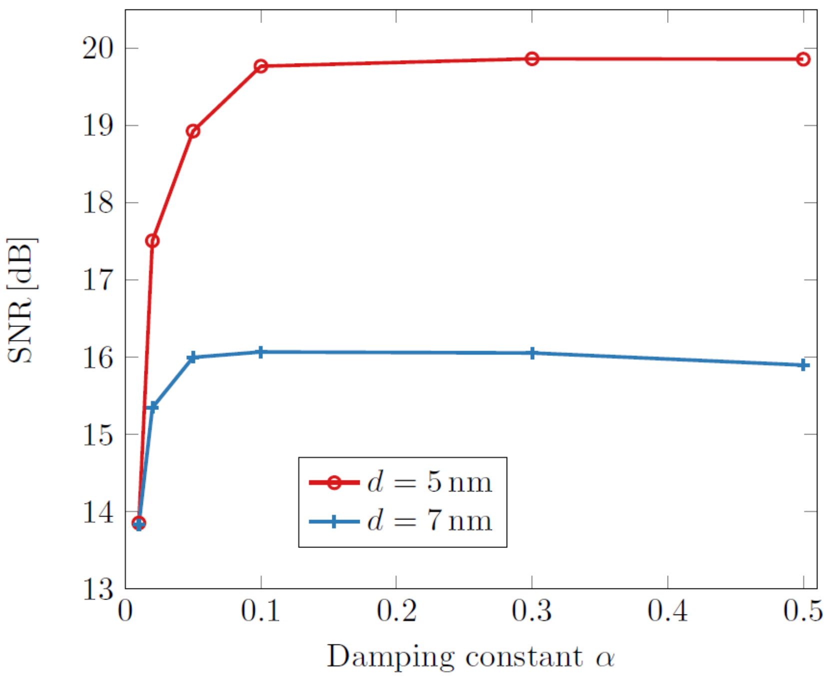

Figure 4.2: Resulting SNR for various damping constants α for grains with two different diameters $d = 5$ nm and $d = 7$ nm.

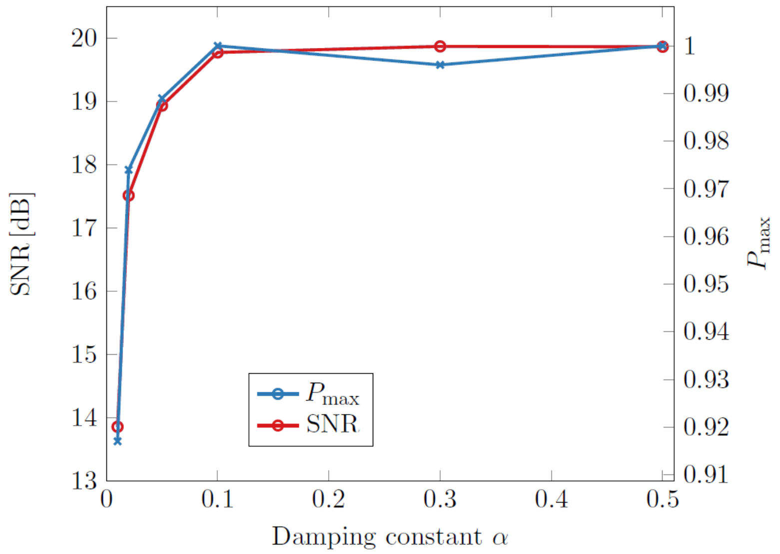

Figure 4.3: SNR and $P_{\max}$ depending on the damping constant α for a grain size with a diameter of 5 nm.

4.4 Combination damping and bit length

In Table 4.7, the comparison between the SNR of the *ASRC parameters* and *parameter set 1* is displayed for grains with diameters $d = 5\,\text{nm}$ and $d = 7\,\text{nm}$. It is visible that for $d = 5\,\text{nm}$ the SNR is about 8.25 dB larger for *parameter set 1* than for the *ASRC parameters* and for $d = 7\,\text{nm}$ it is $\sim 7.4\,\text{dB}$ larger. The question is, if the damping and bit length variation can fully explain this deviation.
Increasing the damping constant from $\alpha = 0.02$ to $\alpha = 0.1$, yields about +2.26 dB for $d = 5\,\text{nm}$ and +0.72 dB for $d = 7\,\text{nm}$. Additionally, with the calculations from

	5 nm		7 nm	
α	σ_{down} [nm]	$P_{\max}$	σ_{down} [nm]	$P_{\max}$
0.01	2.0	0.917	1.13	0.955
0.02	0.9475	0.974	0.83	0.99
0.05	0.7	0.989	0.549	1.0
0.1	0.688	1.0	0.442	1.0
0.3	0.495	1.0	0.48	1.0
0.5	0.64	1.0	0.636	1.0

Table 4.6: Resulting down-track jitter parameters and mean maximum switching probability values for pure hard magnetic material with different damping constants α.

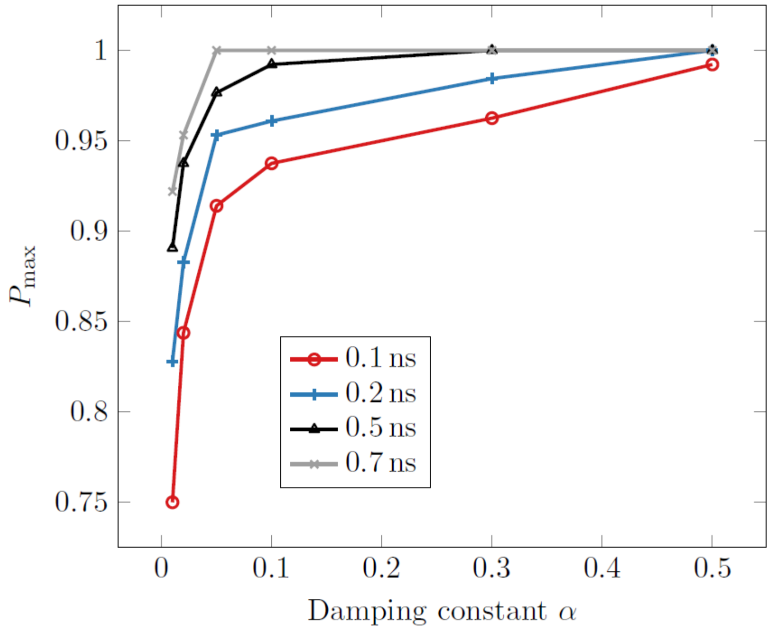

Figure 4.4: Maximum switching probability $P_{\max}$ over damping α for different pulse lengths of the heat pulse. A field strength of $-0.8\,\mathrm{T}$ for grains with diameter $d = 5\,\mathrm{nm}$ is assumed.

Section 4.3.1, one can show that by changing the bit length from $b_1 = 10\,\mathrm{nm}$ to $b_2 = 22\,\mathrm{nm}$ there holds

$$\mathrm{SNR}_{\mathrm{dB}}(b_2) = \mathrm{SNR}_{\mathrm{dB}}(b_1) + 6.85\,\mathrm{dB}. \tag{4.6}$$

Combined, this shows that the difference in the SNR can be attributed entirely to the damping and the bit length enhancement. The other write head and material parameters that were changed in the simulations have only minor influence on the SNR compared to the damping constant and the bit length which corresponds to the results achieved before.

4.5 Conclusion

To conclude, it was investigated how different write and material parameters influence the signal-to-noise ratio. With this knowledge, recording materials that achieve higher SNRs can be designed. The overall goal was to explain the decrease of the SNR by about 8.25 dB and 7.4 dB for grains with diameters $d = 5\,\mathrm{nm}$ and

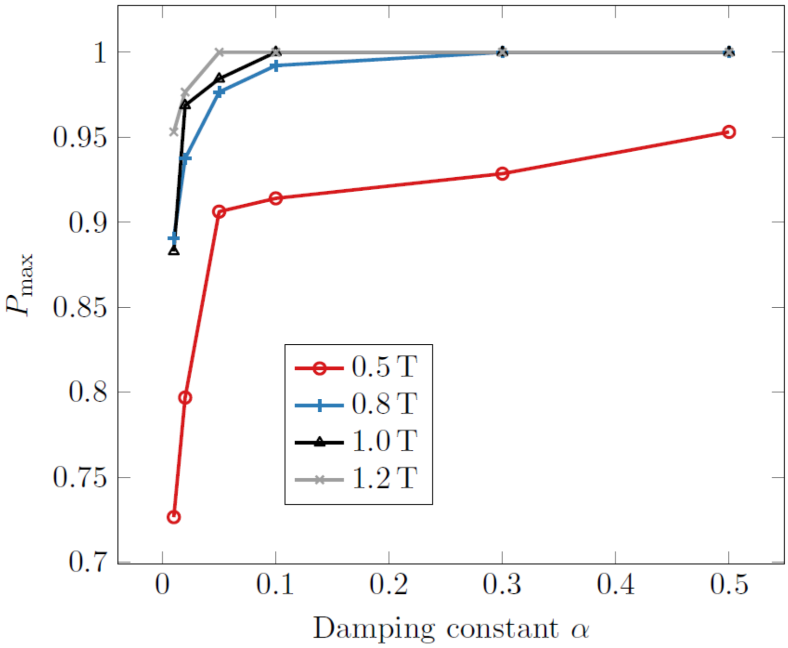

Figure 4.5: Maximum switching probability $P_{\max}$ over damping α for different field strengths. The duration of the heat pulse of 0.5 ns for grains with diameter $d = 5$ nm is assumed.

$d = 7$ nm, respectively, when changing from recording parameters used in former simulations [60, 89, 129] to the *ASRC parameters*. The change in the write head parameters showed a significant influence of the bit length on the SNR. The investigation with changing material parameters showed that most of the parameters have a minor relevance compared to the influence of the damping α.
The effect of the damping constant on the SNR was studied in more detail. The damping constant was varied between $\alpha = 0.01$ and $\alpha = 0.5$ for two different grain sizes $d = 5$ nm and $d = 7$ nm and the SNR was determined. In practice, the damping constant of FePt might be increased by enhancing the Pt concentration [130, 131]. Another option would be to use a high/low T_C bilayer structure [50] and increase the damping of the soft magnetic layer by doping with transition metals [132–136]. An interesting finding of the study is the enormous SNR improvement of 6 dB that can be achieved for 5 nm-grains when enhancing the damping constant from $\alpha = 0.01$ to $\alpha = 0.1$. It is reasonable that the SNR improves with larger damping. This results from the oscillatory behavior of the magnetization for small damping during switching. In fact, smaller damping facilitates the first switching but with larger damping it is more likely that the grain will switch stably during the cooling of the thermal

Parameter set	diameter [nm]	T_{peak} [K]	bit length [nm]	$P_{\max}$	σ_{down} [nm]	SNR [dB]
ASRC	5	760	10.2	0.974	0.95	17.51
Parameter set 1 [60, 89, 129]	5	600	22	0.984	0.384	25.76
ASRC	7	760	10.2	0.99	0.83	15.35
Parameter set 1	7	600	22	1.0	0.44	22.75

Table 4.7: Resulting $P_{\max}$, σ_{down} and SNR values for the simulations with ASRC parameters and those used in former simulations [60, 89, 129].

pulse [137]. This leads to a smaller mean switching time for larger damping constants and in the further course to higher SNR values. However, an increase of the duration of the heat pulse due to a smaller head velocity or an increase of the field strength can improve the SNR even for smaller damping constant.

Furthermore, the results display a SNR saturation for damping constants $\alpha \geq 0.1$. This SNR saturation can be explained with the saturation of the maximum switching probability and the marginal change of the down-track jitter for $\alpha \geq 0.1$. Indeed, one can check that for shorter pulse durations and smaller field strengths, the behavior is different and the SNR does not saturate. In this case, the SNR rises further for increasing damping constants. Summarizing, the SNR saturation for a varying damping constant depends strongly on the used field strength and the duration of the heat pulse.

The qualitative behavior for 7 nm-grains is the same as for the 5 nm-grains. Interestingly, the SNR change for a varying damping constant is not as significant as for grains with $d = 5$ nm. This results from the higher maximum switching probability and the smaller down-track jitter for 7 nm-grains even for small damping constants. This is as expected since larger grain sizes lead to an elevated maximum switching probability [89] and smaller transition jitter [40] compared to smaller grain sizes due to finite size effects. This limits the possible increase of the recording performance in terms of $P_{\max}$ and σ_{down} and thus the possible SNR gain. Additionally, the SNR saturation value is smaller for 7 nm-grains since one bit consists of fewer grains.

Together with the bit length variation, the SNR variation between the two considered parameter sets could be fully attributed to the damping enhancement. The other changed parameters like the atomistic spin moment, the grain height, the exchange interaction and the full width at half maximum have only a minor relevance compared to the influence of the damping α and the bit length.

In fact, the variation of the bit length gave the largest SNR change. However, since an increase of the bit length is not realistic in recording devices, the variation of the material parameters, especially the increase of the damping constant, is a more promising way to improve the SNR.

Chapter 5

Noise Due to a Temperature Gradient in $z-$direction

Parts of this chapter have been previously published in [138] and have been reproduced with permission of the coauthors and in accordance with the publisher's policy. Content that was not generated by the author of this thesis is explicitly denoted, copyright is held by Elsevier.

5.1 Introduction

Quite a number of investigations have been performed to study HAMR in all details since its proposal almost 60 years ago [18]. Since a heat pulse is included in the recording process, it is interesting to investigate how the applied temperature influences the recording process. There are works that study the temperature distribution in lateral direction [139, 140]. However, most of the theoretical works do not study the effect of the temperature reduction in $z-$direction within the material in the writing process. Since the temperature of the heat pulse acts differently on different layers in the material in reality, it is interesting to analyze how this effects the performance of HAMR in terms of the maximum switching probability and the transition jitter. These two parameters are considered for the reason that they have a strong influence on the SNR [119]. In this section, it is investigated how a temperature gradient in $z-$direction within the material influences the switching probability and the noise of a grain with a diameter of 5 nm and a height of 10 nm in terms of the down-track jitter. To do this, pure FePt$-$like hard magnetic grains are considered and different temperature variations of the heat pulse in $z-$direction are assumed. Furthermore, it is studied if an artificial Curie temperature gradient within the material in $z-$direction produced by a cleverly designed multilayer structure leads to the same effect as the temperature gradient and thus, can compensate the performance loss due to the decreased temperature. The simulations are performed with the atomistic simulation program VAMPIRE [96].

5.2 Modeling Parameters

5.2.1 Write head parameters

For the simulations, the HAMR model from Section 3.5 is used. The parameters that are used for the model of the HAMR process are the following:

- Grain diameter $d = 5\,\text{nm}$
- Grain height $h = 10\,\text{nm}$
- FWHM $= 20\,\text{nm}$
- Head velocity $v = 20\,\text{m/s}$
- Field duration $= 1\,\text{ns}$
- $T_{\text{min}} = 270\,\text{K}$

Note, the maximum thermal gradient in the simulations ($25\,\text{K/nm}$) is higher than that used in reality ($\sim 3 - 14\,\text{K/nm}$ [3, 14, 141]). These assumptions are made since higher thermal gradients will be needed to further increase the areal density in the future for the materials used in this section. However, this is only valid for high damping constant $\alpha = 0.1$ as used in this section. The simulations in Chapter 4 show that this is not the case for small damping $\alpha = 0.02$ since here the SNR decreases with smaller FWHM and the resulting higher thermal gradient. The reason is that due to the higher thermal gradient, the time window in which the grain can be aligned in write direction becomes to small to write the grain in the case of small damping. For $\alpha = 0.1$ the average switching time is smaller and thus the grain can be aligned correctly even for higher thermal gradients and the corresponding shorter time windows.

5.2.2 Variation of T_{peak}

An FePt-like hard magnetic grain is considered and different temperature variations in $z-$direction are studied. The first "ideal" structure is pure hard magnetic material

Curie temp. T_{C} [K]	Damping α	Uniaxial anisotropy k_u [J/atom]	J_{ij} [J/link]	μ_{s} [μ_{B}]
536.6	0.1	9.12×10^{-23}	5.18×10^{-21}	1.7

Table 5.1: Material parameters of an FePt-like hard magnetic material. k_u is the uniaxial anisotropy constant. J_{ij} is the exchange interaction within the material and μ_{s} is the atomistic spin moment. α is the damping constant.

(HM) where no temperature gradient is assumed but a constant temperature applied to the material is considered. A schematic picture of this material configuration can be seen in Figure 5.1(a) and was already studied in former works [60,89,90]. Secondly, a grain consisting of two identical layers of hard magnetic material is considered where the only difference is the peak temperature T_{peak} (which is in the further course of this section also denoted T_{p}) of the applied heat pulse on each layer. Hereby, the peak temperature of the heat pulse applied to the top layer is assumed to be 20% larger than that applied to the bottom layer [142] (see Figure 5.1(b)). The last structure is a grain consisting of 20 identical hard magnetic material layers, see Figure 5.1(c). Again, the difference between the applied peak temperature on the top layer and the applied peak temperature on the bottom layer is 20%. In between, the peak temperature decreases linearly from top to bottom. Henceforth, the first material is called "$(\mathrm{HM})_{N=1}$", while the second and third structures are named "$(T_{\mathrm{p}})_{N=2}$" and "$(T_{\mathrm{p}})_{N=20}$", respectively. The material parameters that are used for all structures can be seen in Table 5.1.

5.2.3 Variation of T_{C}

Additional simulations are performed, where the Curie temperature T_{C} of different layers is varied. The questions is, if a T_{C} gradient in $z-$direction with a spatially homogeneous applied temperature leads to the same results as an applied temperature gradient.

The treated structures are similar to those considered above. First, a grain consisting of two hard magnetic material layers is considered where the Curie temperature of the bottom layer is 20% larger than that of the top layer. This is done by increasing the exchange constant in the bottom layer by 20%, since there holds

$$J_{ij} = \frac{3k_{\mathrm{B}}T_{\mathrm{C}}}{\epsilon z}, \tag{5.1}$$

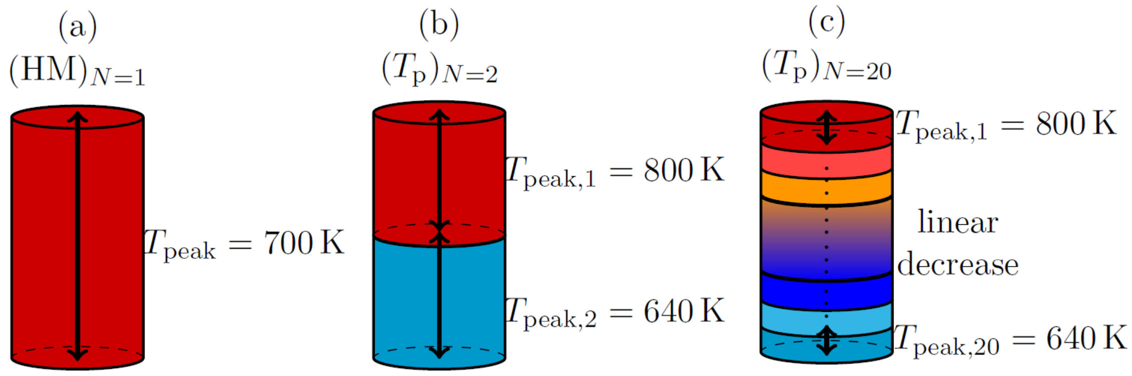

Figure 5.1: Schematic representation of the considered hard magnetic structures and the temperature profile of (a) (HM)$_{N=1}$, (b) $(T_p)_{N=2}$ and (c) $(T_p)_{N=20}$ in $z-$direction at $x = 0, y = 0$. The arrows indicate the $T(x = 0, y = 0, z)$ profile with T_{peak} being the peak temperature that is applied to the respective layer.

where k_B is the Boltzmann constant, z is the number of nearest neighbors and ϵ is a correction factor from the mean-field expression which is approximately 0.86 [96]. All other material parameters are taken as before. The second structure is a grain consisting of 20 hard magnetic material layers where the difference between the Curie temperature of the top layer and that of the bottom layer is 20% with a linear increase from top to bottom. The first structure is denoted "$(T_C)_{N=2}$" and the second one "$(T_C)_{N=20}$". Note, that for these structures the peak temperature is assumed to be homogeneous.
In the course of the work, a temperature gradient is combined with a T_C gradient, to see if both gradients can compensate each other. Here, other than previously, the Curie temperature is decreased from top to bottom. The results are then compared with pure hard magnetic material. Again, a structure with two layers, named "$(T_p + T_C)_{N=2}$", and one with 20 layers, called "$(T_p + T_C)_{N=20}$", are considered.

5.3 Results

5.3.1 T_p Gradient

First, the switching probability phase diagram of (HM)$_{N=1}$ is determined as described in Section 3.5.1. The phase diagram in Figure 5.2 shows the switching probability as a function of the down-track position x and the peak temperature T_{peak} that corresponds to y (see eq. (3.45)). The resolution in down-track direction is $\Delta x = 2\,\text{nm}$ and

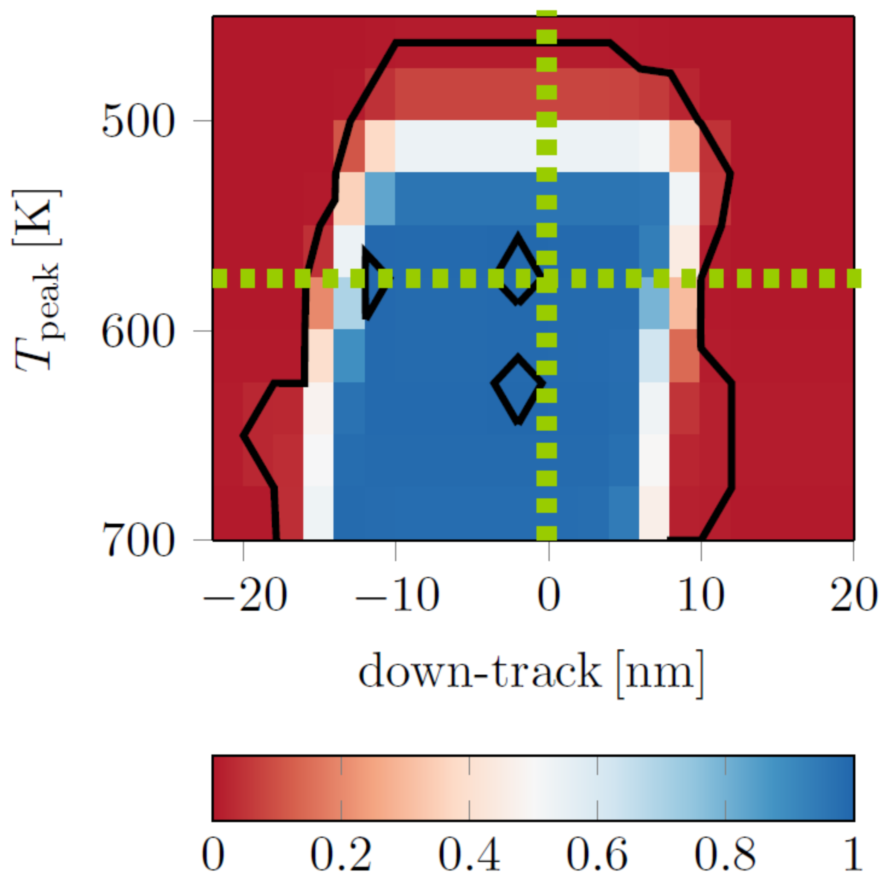

Figure 5.2: Switching probability phase diagram of a pure FePt-like hard magnetic grain with constant temperature applied. The contour lines indicate the transition between areas with switching probability less than 0.8% (red) and areas with switching probability higher than 99.2% (blue). The threshold 99.2% is used since 128 simulations per phase point are performed and thus 100% switching probability in the simulations corresponds to a switching probability greater than $1 - 1/128 = 0.992$ in reality. The dashed lines mark the switching probability curves in down-track and off-track direction that can be seen in Figure 5.4.

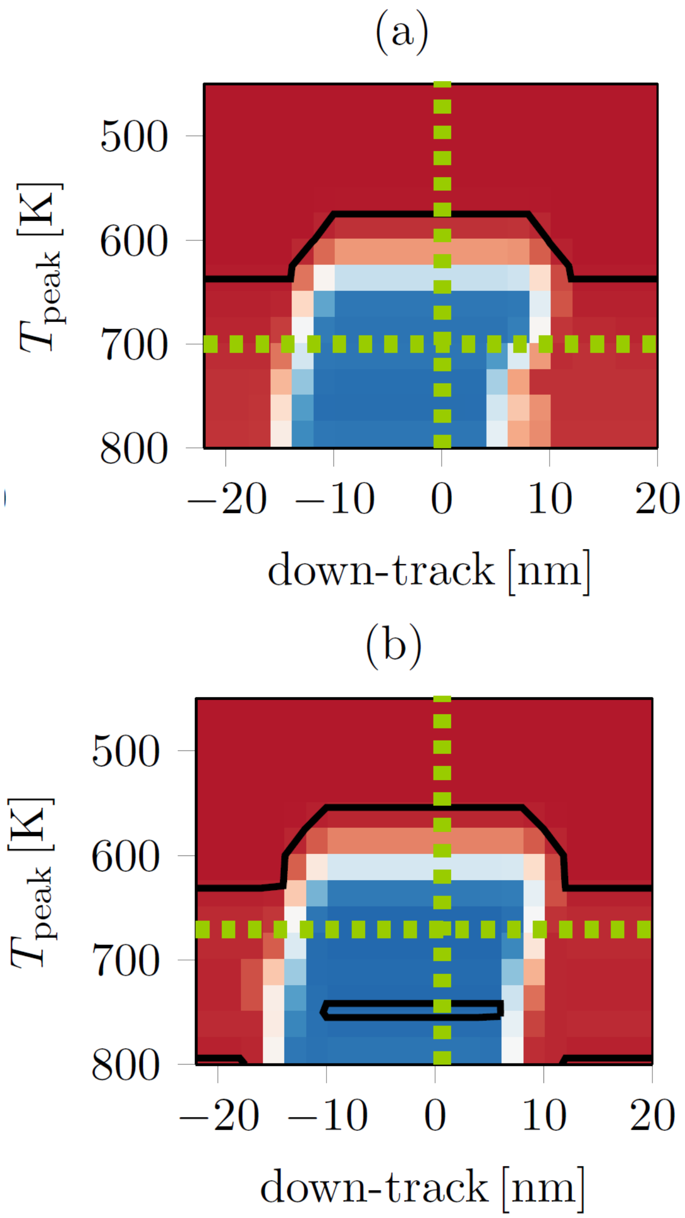

Figure 5.3: Switching probability phase diagrams of a grain with (a) two layers hard magnetic material and (b) 20 layers hard magnetic material and an applied temperature gradient. The contour lines mark the transition between areas with switching probability less than 0.8% (red) and areas with switching probability higher than 99.2% (blue). The dashed lines mark the switching probability curves in off-track and down-track direction that can be seen in more detail in Figure 5.4.

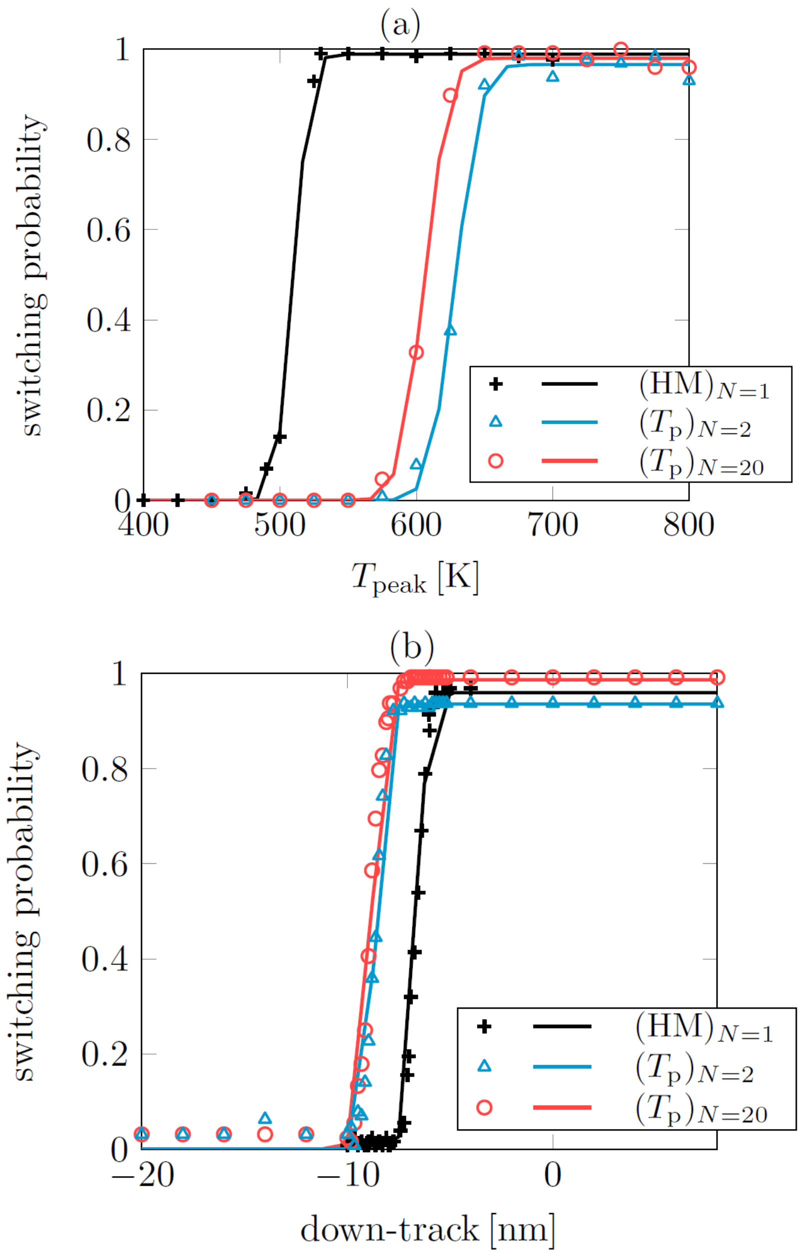

Figure 5.4: Simulations (marks) and fits (solid line) of switching probability curves of materials with an applied T_p gradient. The $P(T_{\mathrm{peak}})$ curve at down-track position $x = 0\,\mathrm{nm}$ is plotted in (a). In (b) one can see $P(x)$ at $T_{\mathrm{peak},(\mathrm{HM})_{N=1}} = 575\,\mathrm{K}$, $T_{\mathrm{peak},(\mathrm{T_p})_{N=2}} = 700\,\mathrm{K}$ and $T_{\mathrm{peak},(\mathrm{T_p})_{N=20}} = 675\,\mathrm{K}$.

the resolution in temperature direction is $\Delta T_{\text{peak}} = 25\,\text{K}$. In each phase point, 128 simulations are performed. Thus, the phase diagram contains about 60,000 switching trajectories, each with a duration of 2 ns. The vertical dashed line marks the down-track position $x = 0\,\text{nm}$, whereas the horizontal dashed line indicates the peak temperature $T_{\text{peak}} = 575\,\text{K}$. Analogous to $(\text{HM})_{N=1}$, phase diagrams for $(T_{\text{p}})_{N=2}$ and $(T_{\text{p}})_{N=20}$ are determined. The simulations with a T_{p} gradient are later compared to simulations with a T_{C} gradient (see Section 5.3.2). To make these simulations comparable, the write temperature $T_{\text{write}} = 800\,\text{K}$ is used in the simulations. The results can be seen in Figure 5.3(a) and (b). From the switching probability phase diagrams, one can see differences in the switching behavior of the three temperature gradients. $(\text{HM})_{N=1}$ only shows few areas of complete (100%) switching. Anyway, the phase diagram of $(T_{\text{p}})_{N=2}$ shows no areas of complete switching at all. For $(T_{\text{p}})_{N=20}$ the phase diagram shows 100% switching probability for only one temperature, namely $T_{\text{peak}} = 750\,\text{K}$. An interesting observation is that for $(\text{HM})_{N=1}$ switching starts at temperatures more than 20% lower than for the temperature gradients. To compare the switching behavior of the structures in more detail, the off-track jitter σ_{off} and the down-track jitter σ_{down} are computed. The switching probability curves in off-track direction at down-track position $x = 0\,\text{nm}$ are marked by the vertical dashed lines in Figure 5.2 and Figure 5.3(a) and (b). The resulting $P(T_{\text{peak}})-$curves for temperatures in a range of 400 K and 800 K with $\Delta T_{\text{peak}} = 25\,\text{K}$ can be seen in Figure 5.4(a). A significant difference between the off-track probability curves of the different structures is the temperature that is needed to write the grain with a switching probability $> 90\%$ (T_{switch}). Whereas the switching temperature for pure $(\text{HM})_{N=1}$ is at approximately $T_{\text{switch}} = 525\,\text{K}$ (see Figure 5.4), it is at 625 K for $(T_{\text{p}})_{N=20}$ and 650 K for $(T_{\text{p}})_{N=2}$. In order to compare the off-track jitter σ_{off} of the material configurations more accurately, the switching probability curves are fitted with a Gaussian cumulative distribution function as in Section 3.5.2. Fitting the $P(T_{\text{peak}})$ curve of the material configurations gives the jitter parameter in temperature direction. These computed jitter parameters in temperature direction are then converted into an off-track jitter via the given thermal pulse profile (3.45) and can be seen in Table 5.2. Similar to the off-track jitter, the down-track jitter of the different structures is compared. The down-track switching probability curve $P(x)$ at a certain peak temperature (resp. off-track position) can be determined by making a horizontal cut at the corresponding peak temperature in the phase diagram (see Figure 5.2 and Figure 5.3). Since writing of the grain starts at higher tempera-

Material	σ_{off} [nm]	σ_{off} [%]	σ_{down} [nm]	σ_{down} [%]	$P_{\text{max,off}}$	$P_{\text{max,down}}$
$(\text{HM})_{N=1}$	0.326	—	0.45	—	0.989	0.969
$(T_{\text{p}})_{N=2}$	0.49	+50	0.47	+4.4	0.988	0.936
$(T_{\text{p}})_{N=20}$	0.48	+47.2	0.52	+15.5	0.98	0.967
$(T_{\text{C}})_{N=2}$	0.87	+166.8	0.72	+60	0.966	0.968
$(T_{\text{C}})_{N=20}$	0.6	+84	0.6	+33.3	0.97	0.981
$(T_{\text{p}}+T_{\text{C}})_{N=2}$	0.398	+22	0.44	−2.2	0.999	0.994
$(T_{\text{p}}+T_{\text{C}})_{N=20}$	0.31	−4.9	0.41	−8.89	0.998	0.996

Table 5.2: Resulting jitter parameters extracted from Figure 5.4, Figure 5.6 and Figure 5.8. $P_{\text{max,off}}$ and $P_{\text{max,down}}$ are the fitting parameters P_{max} for the switching probability curves in off-track and down-track direction, respectively. σ_{down} and σ_{off} are additionally compared to those of $(\text{HM})_{N=1}$.

tures for $(T_{\text{p}})_{N=2}$ and $(T_{\text{p}})_{N=20}$, the down-track jitter is calculated at different peak temperatures for the different compositions to make it comparable. The considered peak temperatures are 10% higher than the switching temperature T_{switch}. Thus, the down-track switching probability curve is calculated at $T_{\text{peak},(\text{HM})_{N=1}} = 575\,\text{K}$, $T_{\text{peak},(\text{T}_{\text{p}})_{N=2}} = 700\,\text{K}$ and $T_{\text{peak},(\text{T}_{\text{p}})_{N=20}} = 675\,\text{K}$. The used peak temperatures are indicated by the horizontal dashed lines in Figure 5.2 and Figure 5.3. In Figure 5.4(b), the resulting $P(x)-$curves are shown. In comparison to the down-track jitter of $(\text{HM})_{N=1}$, the transitions of $(T_{\text{p}})_{N=2}$ and $(T_{\text{p}})_{N=20}$ are shifted to different down-track positions. Again, the switching probability curves are fitted according to Section 3.5.2 to determine the jitter parameter σ_{down} for the different material configurations. The resulting down-track jitter parameters can be seen in Table 5.2.

5.3.2 T_{C} Gradient

In this section, switching probability phase diagrams of the two considered structures with a T_{C} gradient are computed. The resulting phase diagrams can be seen in Figure 5.5. The phase diagrams are similar to those of Section 5.3.1, showing that both simulations qualitatively lead to the same results. However, there is one visible difference. One can see that switching starts at a temperature which is about 50 K lower if a T_{C} gradient is considered instead of a temperature gradient. For better comparison, the switching probability curves in off-track and down-track direction are plotted in Figure 5.6. The down-track switching probability curve of the different structures are again evaluated at different peak temperatures, namely $T_{\text{peak},(\text{HM})_{N=1}} =$

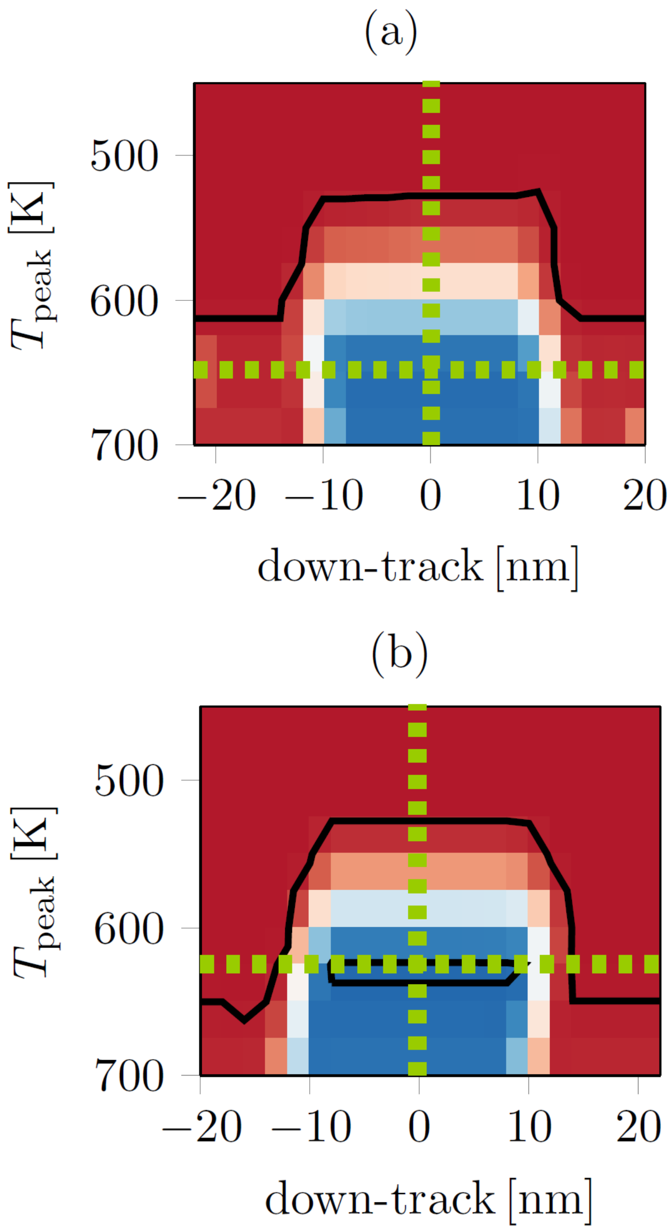

Figure 5.5: Switching probability phase diagrams of a grain with (a) two layers hard magnetic material and (b) 20 layers hard magnetic material, when the Curie temperature is varied between the layers. The contour lines mark the transition between areas with switching probability less than 0.8% (red) and areas with switching probability higher than 99.2% (blue). The dashed lines mark the switching probability curves in off-track and down-track direction that are considered in more detail in Figure 5.6.

575 K, $T_{\text{peak},(\text{T}_\text{C})_{N=2}} = 650\,\text{K}$ and $T_{\text{peak},(\text{T}_\text{C})_{N=20}} = 625\,\text{K}$ which for the latter two are indicated by the horizontal dashed lines in Figure 5.5(a) and (b). The switching probability curves are then fitted with a Gaussian distribution function. Both, the off-track and the down-track jitter parameters are summarized in Table 5.2. These fitting parameters show that compared to a temperature gradient both the off-track and the down-track jitter increase significantly in case of a T_C gradient.

5.3.3 Combination T_p - and T_C Gradient

Finally, simulations are performed where a temperature gradient is combined with a T_C gradient. The switching probability phase diagrams are shown in Figure 5.7. It can be seen that a combination of the T_p and the T_C gradient leads to complete switching in a wide range of down-track positions and peak temperatures. The switching probability curves in off-track and down-track direction are computed and then compared to those of pure hard magnetic material with a constant temperature applied. The resulting switching probability curves can be seen in Figure 5.8 (a) and (b). The switching probability curves in off-track direction of the combined structures look similar to that of $(\text{HM})_{N=1}$. An interesting difference is that the switching probabilities are higher for the combined structure than for $(\text{HM})_{N=1}$. More precisely, both combined structures reach 100% switching probability in the simulations for temperatures higher than 575 K whereas $(\text{HM})_{N=1}$ only reaches complete switching for single temperatures. The switching probability curves in down-track direction are computed at the same peak temperature for all three structures, in this case at $T_\text{peak} = 575\,\text{K}$. Again, it can be seen that a combination of a temperature and a T_C gradient leads to higher switching probabilities than a pure hard magnetic structure with homogeneous applied temperature. Once more, the off-track and down-track jitter parameters are calculated via fitting of the curves. The off-track and down-track jitter parameters for the structures are visible in Table 5.2. In fact, for $(T_\text{p}+T_\text{C})_{N=20}$ the off-track jitter even decreases slightly.

The down-track jitter parameters for the combined structures are even smaller than that of $(\text{HM})_{N=1}$. The higher switching probabilities can be clearly seen with the help of the fitting parameter $P_\text{max,off}$ and $P_\text{max,down}$ in Table 5.2, which is the mean maximum switching probability.

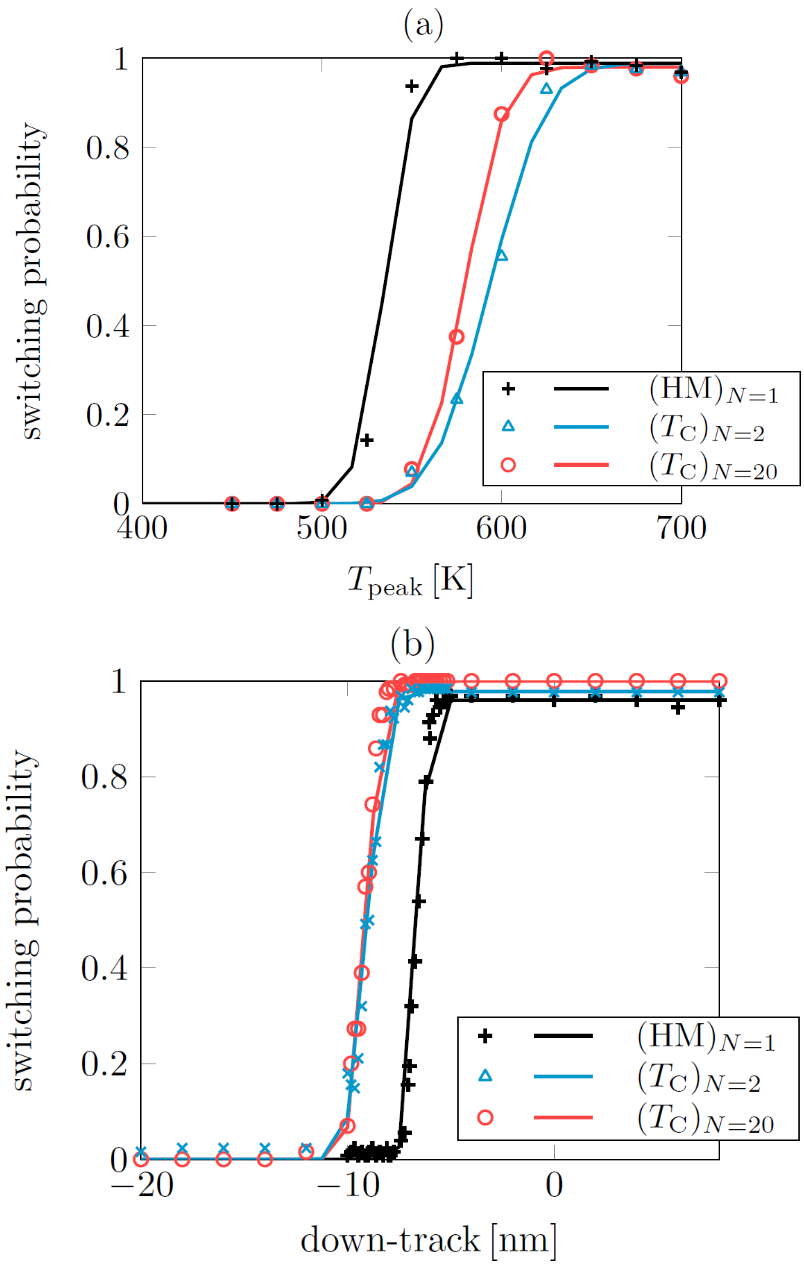

Figure 5.6: Simulations (marks) and fits (solid line) of switching probability curves of materials with a T_C gradient. The $P(T_{\text{peak}})$ curve at down-track position $x = 0\,\text{nm}$ is plotted in (a). In (b) one can see $P(x)$ at $T_{\text{peak},(\text{HM})_{N=1}} = 575\,\text{K}$, $T_{\text{peak},(\text{T}_\text{C})_{N=2}} = 650\,\text{K}$ and $T_{\text{peak},(\text{T}_\text{C})_{N=20}} = 625\,\text{K}$.

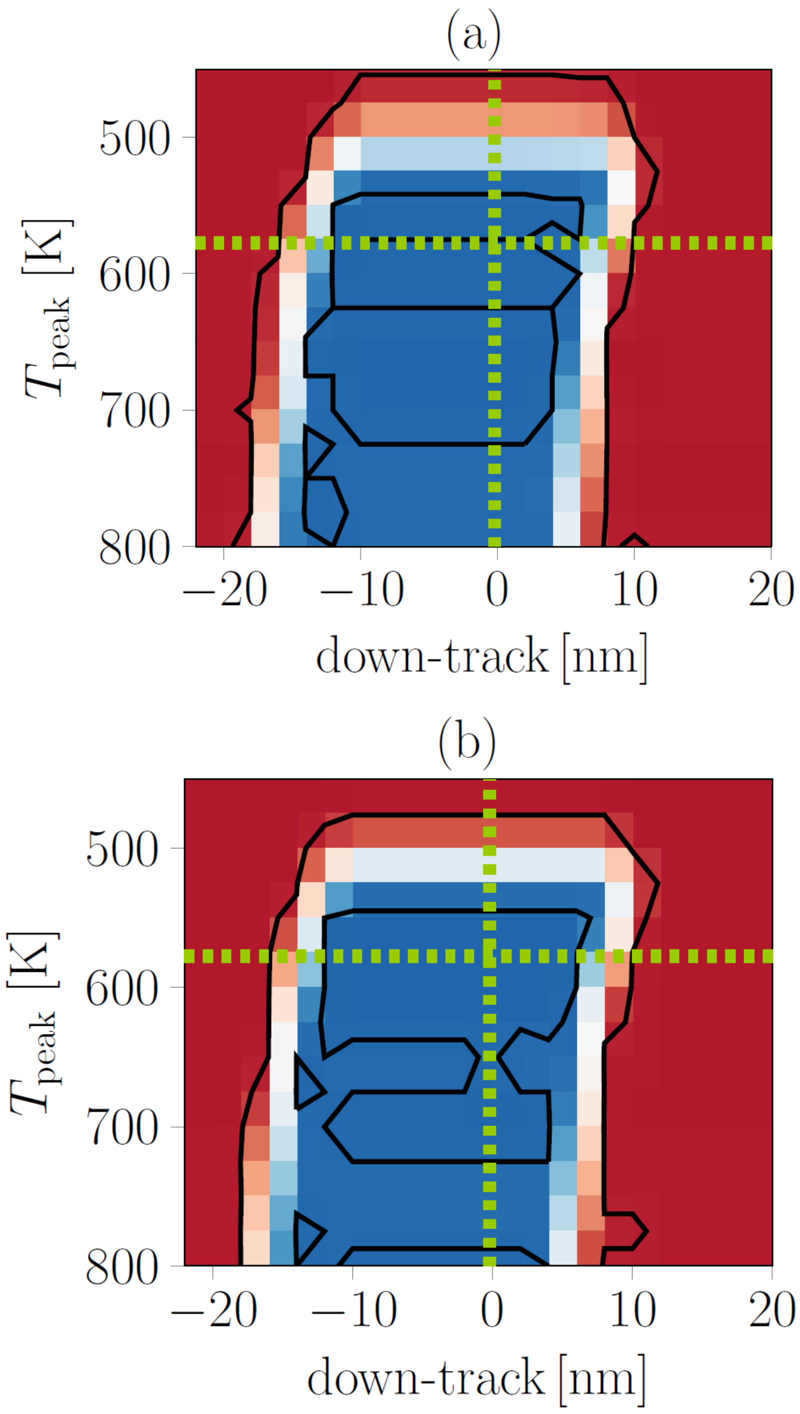

Figure 5.7: Switching probability phase diagrams of a grain with (a) two layers hard magnetic material and (b) 20 layers hard magnetic material, with combined T_{p} and T_{C} gradients. The contour lines mark the transition between areas with switching probability less than 0.8% (red) and areas with switching probability higher than 99.2% (blue). The dashed lines mark the switching probability curves in off-track and down-track direction that are considered in more detail in Figure 5.8.

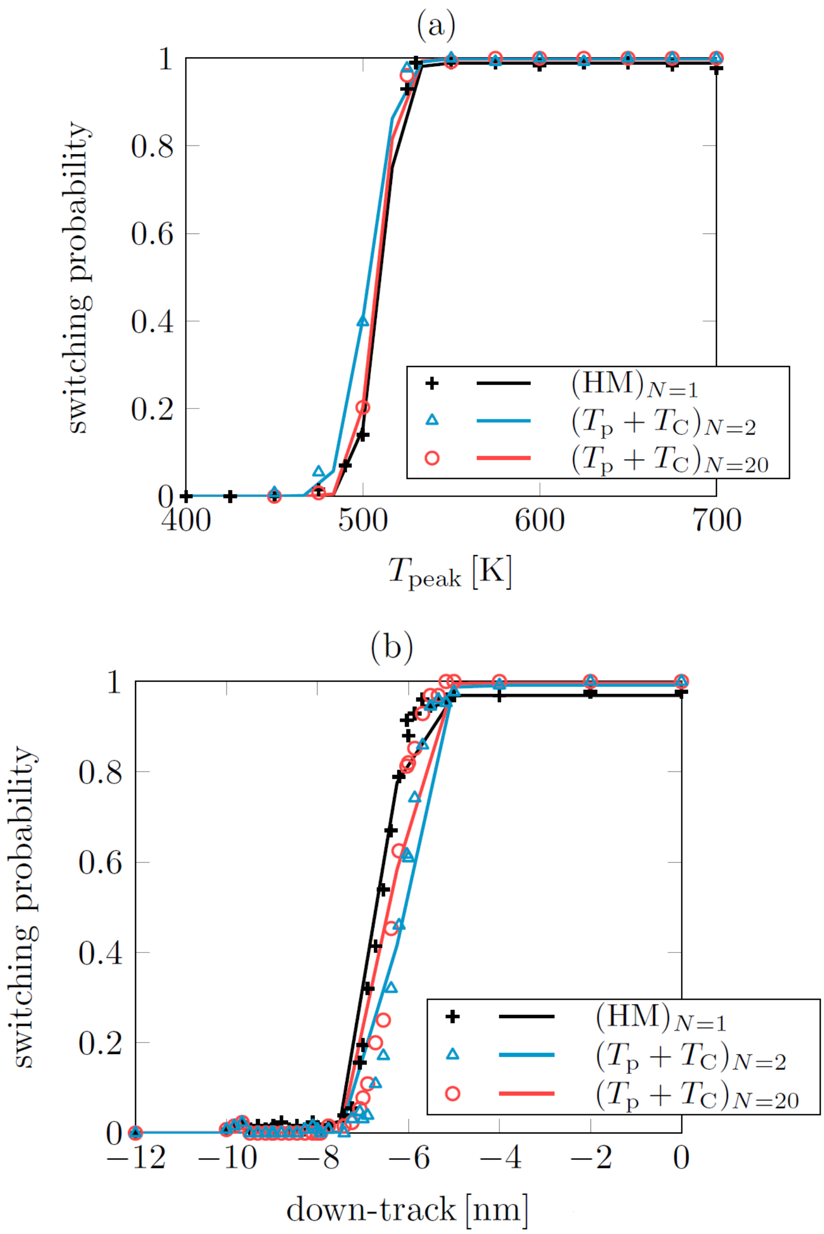

Figure 5.8: Simulations (marks) and fits (solid line) of switching probability curves of materials with combined T_p and T_C gradients. The $P(T_{\text{peak}})$ curve at down-track position $x = 0\,\text{nm}$ is plotted in (a). In (b) one can see $P(x)$ at $T_{\text{peak}} = 575\,\text{K}$.

5.4 Conclusion

Concluding, it was investigated how a reduction of the temperature in $z-$direction within the material influences the switching probability of a cylindrical recording grain with a diameter of 5 nm and a height of 10 nm. Different hard magnetic material compositions were considered where the temperature in the different layers was either reduced in one step or linearly in 20 steps. Additionally, simulations with a T_C gradient within the material were studied. As anticipated, the switching probability reduces for hard magnetic structures when the temperature is reduced in $z-$direction. The results show, that for pure hard magnetic material the grain switches at higher peak temperature and both the off-track and the down-track jitter increase if a temperature reduction in $z-$direction is assumed. In fact, the peak temperature that is needed to write the grain gets approximately 20% higher if the difference between the peak temperatures of the heat pulse in the top and the bottom layer is 20%. This result is especially interesting for the case where the temperature is linearly decreased. Here, one could think that the magnetic moments of the layers with higher temperature, switch easier and induce the magnetic moments in the layers below to switch as well, just like a thermally induced exchange spring effect [46, 47, 50, 143–145]. However, it seems that only the weakest link in the system, i.e. the layer with the lowest applied peak temperature influences the temperature at which the grain is reliably switched.

Note, that the simulations with $N = 2$ already display the qualitative behavior of a temperature gradient really well. The simulations with $N = 20$ do not change the results significantly. That is an interesting result for coarse graining since it shows that considering the temperature gradient very roughly in two layers is enough to get qualitatively good results.

The simulations with a Curie temperature gradient show the same qualitative behavior as those with a temperature gradient. However, a big difference is that switching starts at higher temperatures than for a T_p gradient. Additionally, both the off-track and the down-track jitter are significantly larger than for the temperature gradient. As mentioned before, the simulations with the T_C gradient and those with the temperature gradient qualitatively show the same behavior. In fact, the resulting difference could come from the different shapes of the applied heat pulse. For the Curie temperature gradient, a constant temperature is applied to the grain and thus the shape of the heat pulse is the same for every layer. In contrast to this, the peak temperature of the heat pulse is reduced in every layer for the T_p gradient. Since the

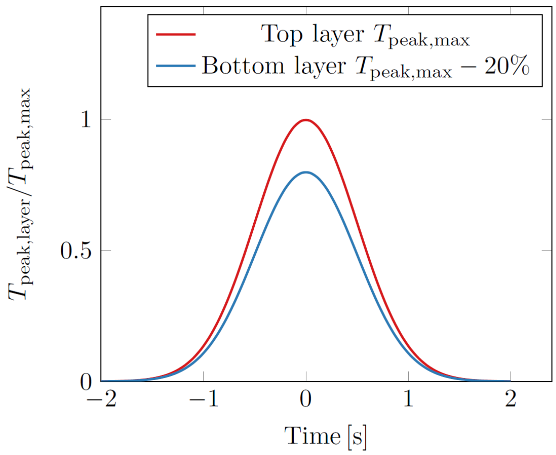

Figure 5.9: Schematic depiction of the different shapes of two heat pulses. The peak temperature of the bottom layer is 20% smaller than that of the top layer. The FWHM is the same for both heat pulses.

FWHM and thus the cooling time of the heat pulse stays the same in the simulation, the heat pulse applied to the top layer is steeper than that applied to the bottom layer. A schematic depiction of the shapes of the heat pulse if the peak temperature is 20% smaller than that of the top layer is shown in Figure 5.9. Eventually, this could result in the deviation between the two simulations. However, since both variations show the same behavior, we combined a temperature gradient with a decreasing Curie temperature in the material and studied if both gradients compensate each other. The results show that the down-track jitter are even smaller than that of $(\text{HM})_{N=1}$. The off-track jitter is also smaller for the $(T_\text{p} + T_\text{C})_{N=20}$ structure. Furthermore, a combination of a temperature and a T_C gradient leads to complete switching in a wider range of temperatures than for pure hard magnetic material with constant temperature. This is a very interesting result since one could use an exchange spring structure [46, 47, 50, 143–145] with a T_C gradient to compensate the HAMR performance loss due to the temperature gradient in z−direction.

For the further course of the work, the temperature drop in z−direction is not further considered within the simulations since the simulations could always be tuned in a way such that the temperature gradient is compensated.

Chapter 6

Noise Reduction in HAMR by Optimizing a High/Low T_C Bilayer Structure

Parts of this chapter have been previously published in [129] and [146] and have been reproduced with permission of the coauthors and in accordance with the publisher's policy. Content that was not generated by the author of this thesis is explicitly denoted, copyright is held by the American Institute of Physics (AIP).

6.1 Introduction

Considering the switching probability curves of a cylindrical FePt-like hard magnetic grain with diameter $d = 5\,\mathrm{nm}$ and height $h = 10\,\mathrm{nm}$ (see Figure 6.1) shows that the switching probability of one grain is clearly below 99% [46] which is too low for practical use in bit-patterned media [20–22]. The idea to overcome this problem is to use a bilayer structure with graded Curie temperature which consists of a hard magnetic layer with low Curie temperature and a soft magnetic layer with high Curie temperature [50]. It has been shown by Vogler *et al* [60] that using a 50/50 low/high T_C bilayer structure increases the maximum switching probability but leads to a significant increase of both the down-track and the off-track jitter parameter (see Figure 6.1).

In the first part of this section, an exchange coupled grain is optimized to obtain a switching probability of $P_{\mathrm{max}} > 99.2\%$ while maintaining the low down-track and off-track jitter of a pure FePt grain with the same dimensions. The threshold 99.2% is used since 128 simulations per phase point are performed and thus 100% switching probability in reality corresponds to a switching probability greater than $1 - 1/128 = 0.992$ in the simulations. The optimization is achieved by varying the composition of the soft magnetic layer as well as the ratio between the soft and the hard magnetic layer. It is reasonable to optimize the recording medium by

maximizing the maximum switching probability and minimizing the transition jitter, since these parameters have a strong influence on the signal-to-noise ratio [119] (see Chapter 4). The Gilbert damping in the hard magnetic layer that is used when obtaining the optimization process is assumed to be $\alpha_{\mathrm{HM}} = 0.1$. However, $\alpha = 0.1$ is too high for FePt-like hard magnetic material in reality.
In Chapter 4 it has already been studied that the damping constant is an important parameter when modeling magnetic recording material since it has a significant influence on the signal-to-noise ratio. Thus, in the second part of the section, the optimization approach is followed for material parameters that were introduced by the Advanced Storage Research Consortium [19], especially for small Gilbert damping $\alpha_{\mathrm{HM}} = 0.02$, and it is studied how the optimized material differs from that with $\alpha_{\mathrm{HM}} = 0.1$.
Additionally, it is investigated how much the areal storage density can be improved when using the optimized recording material instead of the pure hard magnetic one. This is done with the help of the signal-to-noise ratio. The section is structured as follows: First, the principle of exchange spring media (ESM) is introduced. Then, the recording medium optimization process is presented for $\alpha_{\mathrm{HM}} = 0.1$. Further, the optimization process for different material parameters according to the ASRC with $\alpha_{\mathrm{HM}} = 0.02$ is followed and it is studied how much the areal storage density can be improved when using the optimized structure instead of the pure hard magnetic one.

6.2 Exchange Spring Media

Exchange spring medium was first proposed by Suess *et al* [48] in 2004 and is used in commercial hard disks since 2007. Originally, it was introduced to increase the areal storage density in perpendicular magnetic recording. In conventional perpendiclar recording medium, the coercive field and the energy barrier ΔE are linearly dependent on the uniaxial anisotropy constant K via $\Delta E = KV$. Here, V is the volume of the grain. Consequently, enhancing the anisotropy to make smaller grains thermally stable immediately increases the energy barrier. However, the maximum anisotropy is limited by the maximum available head field which are for their parts limited by the highest saturation magnetizations of head materials [47, 144]. A way to further increase the anisotropy of the hard magnetic layer is exchange spring media. The idea of ESM is to use recording grains that consist of a soft magnetic (SM) and a hard magnetic (HM) layer which are strongly exchange coupled [46, 47, 49, 143, 144]. The soft magnetic layer acts as a magnetic spring to initiate switching of the hard

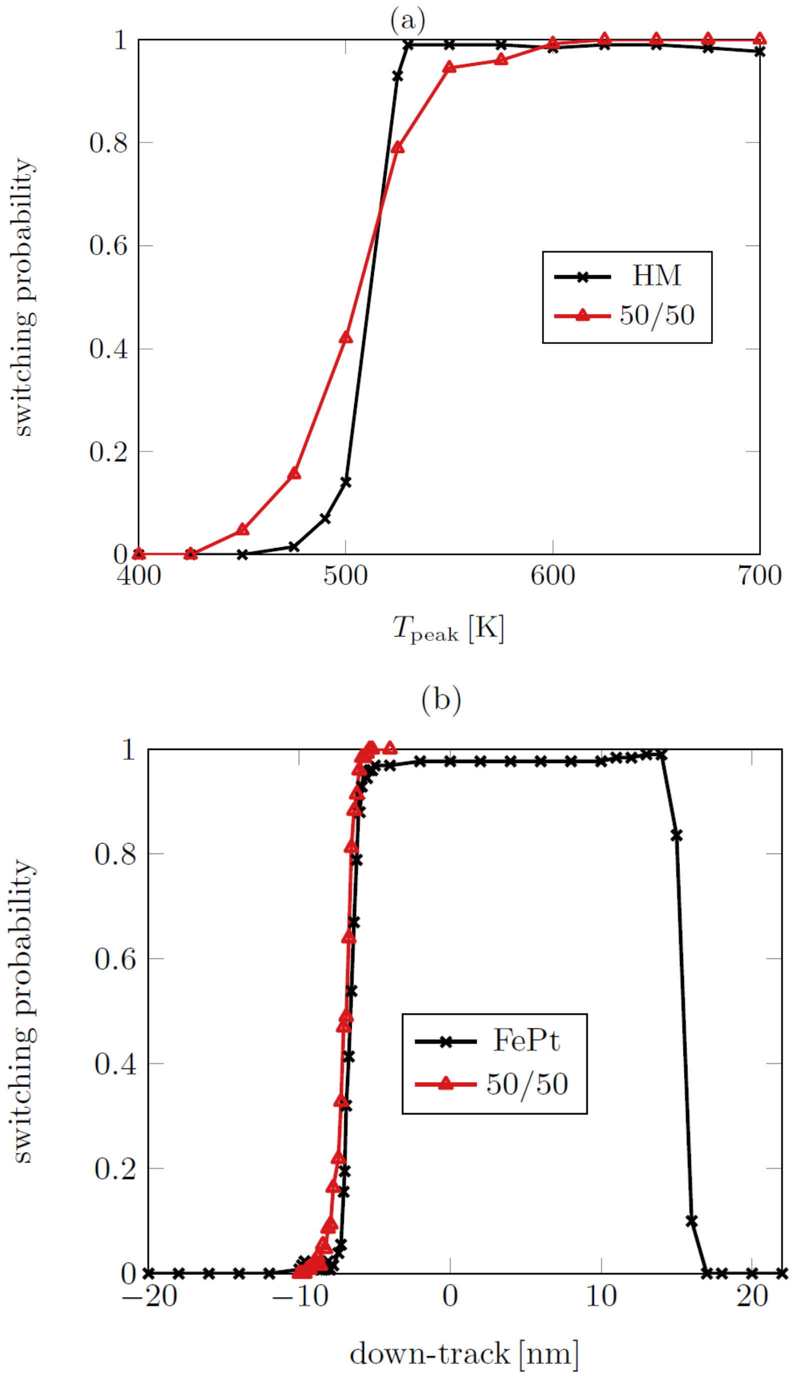

Figure 6.1: Comparison of the switching probability curves in (a) off-track direction and (b) down-track direction for pure hard magnetic material and a bilayer structure with 50% hard and 50% soft magnetic material.

magnetic layer and is thus a write assist. Switching happens in two steps. If an external field is applied, first, a nucleation is formed in the soft magnetic layer. The nucleation field is given by [49, 147]

$$H_\mathrm{N} = \frac{2K_\mathrm{soft}}{J_\mathrm{S}} + \frac{2A\pi^2}{4t_\mathrm{soft}^2 J_\mathrm{S}} \tag{6.1}$$

where K_soft, J_S and A are the anisotropy, the spontaneous polarization and the exchange constant in the soft magnetic layer, respectively. t_soft is the thickness of the soft magnetic layer. The second term on the right hand side describes the exchange field from the hard magnetic layer that stabilizes the soft layer. The nucleation propagates towards the interface between the hard and the soft magnetic layer where it gets pinned. If the external field exceeds the so-called pinning field H_P, the domain wall propagates through the hard magnetic layer and the whole grain switches. The resulting coercive field is then given by $H_\mathrm{c} = \max(H_\mathrm{N}, H_\mathrm{P})$. The coercive field is strongly dependent on the exchange coupling strength between the magnetic layers. If the layers are not exchange coupled, the switching field is equivalent to that of a pure hard magnetic grain. If the exchange coupling strength is increased, the switching field decreases until it reaches a minimum. However, further increasing the exchange coupling strength leads to an opposite effect by causing larger switching fields again. This is due to the fact that the soft magnetic layer gets coupled too strong to the hard magnetic layer and looses its ability to freely rotate before switching.

In ESM, the ratio between the energy barrier and the coercive field is not constant as predicted by the Stoner-Wohlfarth theory allowing for independent optimization. This is due the different magnetization states during switching. In fact, thermal stability and coercivity can be optimized independently from each other. Theoretically, the lowest coercive field can be obtained for $K_\mathrm{soft} = 1/5K_\mathrm{hard}$, where K_soft and K_hard are the anisotropy constants of the soft and the hard magnetic layer, respectively. Additionally, the thermal stability of the exchange spring medium can be improved by a factor 2 compared to a single phase medium while the coercivity stays unchanged by optimizing the material parameters.

6.3 Optimization Procedure

6.3.1 Modeling Parameters

A. Write Head Parameters

In this section, the same write head parameters as in Section 5.2.1 are used:

- FWHM = 20 nm
- Head velocity $v = 20\,\mathrm{m/s}$
- Field duration = 1 ns
- $T_{\mathrm{min}} = 270\,\mathrm{K}$

B. Hard Magnetic Layer

The composition of the FePt-like hard magnetic material (HM) is the same in all simulations which are performed with the atomistic simulation program VAMPIRE. Only the amount of the hard magnetic material is optimized later. The parameters are chosen as follows: For the damping constant we use $\alpha_{\mathrm{HM}} = 0.1$. The atomistic spin moment in $\mu_{\mathrm{HM}} = 1.7\,\mu_{\mathrm{B}}$ which corresponds to a saturation polarization $J_{\mathrm{HM}} = 1.42\,\mathrm{T}$. The exchange energy within the hard magnetic material is $J_{ij,\mathrm{HM}} = 5.18 \times 10^{-21}\,\mathrm{J/link}$. We use uniaxial anisotropy in $z-$direction with an anisotropy constant $k_{\mathrm{u}} = 9.12 \times 10^{-23}\,\mathrm{J/atom}$ which corresponds to an uniaxial anisotropy $K_{1,\mathrm{HM}} = 6.6\,\mathrm{MJ/m^3}$. This material composition was also used in former simulations by Suess *et al* [46] and Vogler *et al* [60].

C. Optional Parameters

In order to find the material composition which maximizes the switching probability and simultaneously minimizes the transition jitter, different parameters of the soft magnetic material (SM) are varied and simulations for the different material compositions are performed. However, some parameters of the soft magnetic material are specifically chosen to model the material as simple as possible. The fixed parameters, on one hand, are the damping constant $\alpha_{\mathrm{SM}} = 0.1$ and the anisotropy constant $k_{u,\mathrm{SM}}$ which is set to zero. On the other hand, the exchange energy within the layer, the exchange energy between the layers and the atomistic spin moment are variable. The amount of hard and soft magnetic material in the simulations to determine the

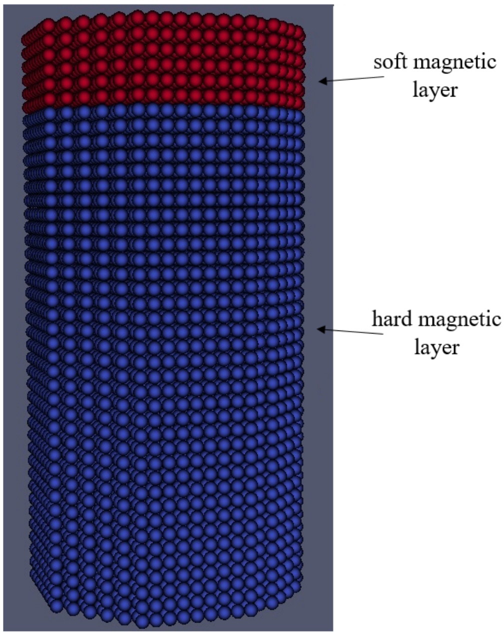

Figure 6.2: Schematic representation of the atoms within the cylindrical recording grain with a bilayer structure composed of 20% soft magnetic material (red) and 80% hard magnetic material (blue).

optimal soft magnetic material composition is always 50%.
After the optimal soft magnetic material configuration has been found, the amounts of soft and hard magnetic material are additionally varied to further optimize the recording grains. Figure 6.2 shows a grain consisting of different amounts hard and soft magnetic material.

6.3.2 Results

A. Hard Magnetic Layer

First, a phase diagram (see Section 3.5.1) is computed for a pure FePt-like grain, see Figure 6.3. In the phase diagram, the switching probability is shown as a function of the down-track position x and the peak temperature T_{peak}. The same parameters as in Section 5.3.1 are used, namely

- $\Delta x = 2\,\mathrm{nm}$
- $\Delta T_{\mathrm{peak}} = 25\,\mathrm{K}$
- 60,000 switching trajectories with 2 nm duration.

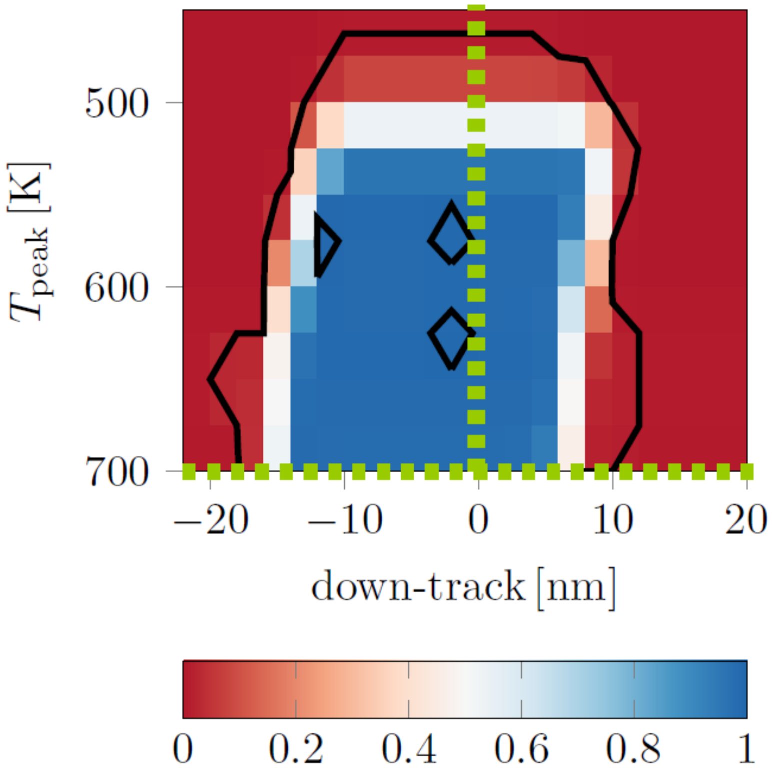

Figure 6.3: Switching probability phase diagram of a pure FePt-like hard magnetic grain. The contour lines indicate the transition between areas with switching probability less than 0.8% (red) and areas with switching probability higher than 99.2% (blue). The dashed lines mark the switching probability curves in Figure 6.5 and Figure 6.6.

The areas with less than 0.8% switching and the areas with more than 99.2% switching are marked by the contour lines. The phase diagram of the pure hard magnetic grain shows only a few areas of complete (100%) switching. In particular, no complete switching occurs for high peak temperatures larger than 650 K. This shows the high DC noise of pure hard magnetic grains. It can be explained by the high thermal gradient for temperatures larger than 650 K. Due to the high thermal gradient, the recording time window gets smaller and is therefore too small for the hard magnetic grain to reliably switch [40, 90, 148].
Both the off-track and the down-track jitter can be extracted from the switching probability phase diagram (see Section 3.5.2). In Figure 6.3, the off-track switching probability curve at down-track position $x = 0$ nm is marked by the dashed vertical line at $x = 0$ nm. The down-track switching probability curve for $T_{peak} = T_{write}$

(corresponds to off-track position $y = 0$ nm with eq. (3.45)) is marked by the dashed horizontal line. For a peak temperature $T_{\text{peak}} = 700$ K, the switching probability curve in off-track direction at down-track position $x = 0$ nm and the switching probability curve in down-track direction at off-track position $y = 0$ nm can be seen in Figure 6.5 and Figure 6.6.

B. Soft Magnetic Layer

In this section, an exchange coupled bilayer structure is considered. The parameters for a suitable soft magnetic composition are sought. Since the atomistic simulations are very time consuming, it is not possible to calculate a switching probability phase diagram for every material configuration. For this reason, only the switching probability curve along the temperature (corresponds to off-track) direction at down-track position $x = 0$ nm is calculated. The result of these simulations is a switching probability curve $P(T_{\text{peak}})$ for $400\,\text{K} \leq T_{\text{peak}} \leq 700\,\text{K}$ which gives both, the maximum switching probability in the center of the grain and the off-track jitter σ_{off}. Additionally, the switching probability curve along the down-track direcion at $T_{\text{peak}} = T_{\text{switch}} + 10\%$ (see Section 5.3.1) is computed and the down-track jitter σ_{down} is extracted. In a first optimization step, soft magnetic materials reaching complete switching in the center of the grains are pre-selected. To do this, the switching probability curves are fitted with a Gaussian cumulative distribution function as in Section 3.5.2. In Figure 6.4, one can see the fitting parameter P_{max} for a recording grain as a function of different atomistic spin moments μ_{SM} and different exchange energies $J_{ij,\text{SM}}$ within the soft layer. Materials with P_{max} less or equal 99.2% are not further considered. The phase diagram shows, that there are a few material compositions with sufficiently high P_{max}. For these materials, the fitting parameters σ_{off} and σ_{down} are additionally compared for the different configurations and the material with the lowest off-track and down-track jitter simultaneously is chosen. Two materials, namely that with $\mu_{\text{SM}} = 1.7\,\mu_{\text{B}}$ and $J_{ij,\text{SM}} = 7.25 \times 10^{-21}$ J/link and that with $\mu_{\text{SM}} = 2.0\,\mu_{\text{B}}$ and $J_{ij,\text{SM}} = 7.25 \times 10^{-21}$ J/link nearly have the same and the lowest σ_{off} and σ_{down}. Since the atomistic spin moment for the hard magnetic material is $\mu_{\text{HM}} = 1.7\,\mu_{\text{B}}$ the same value is chosen for the soft magnetic material.

In summary, the optimal parameters for the soft magnetic composition are shown in Table 6.1. The exchange energy between the materials is given by $J_{ij} = \sqrt{J_{ij,\text{HM}} \cdot J_{ij,\text{SM}}}$.

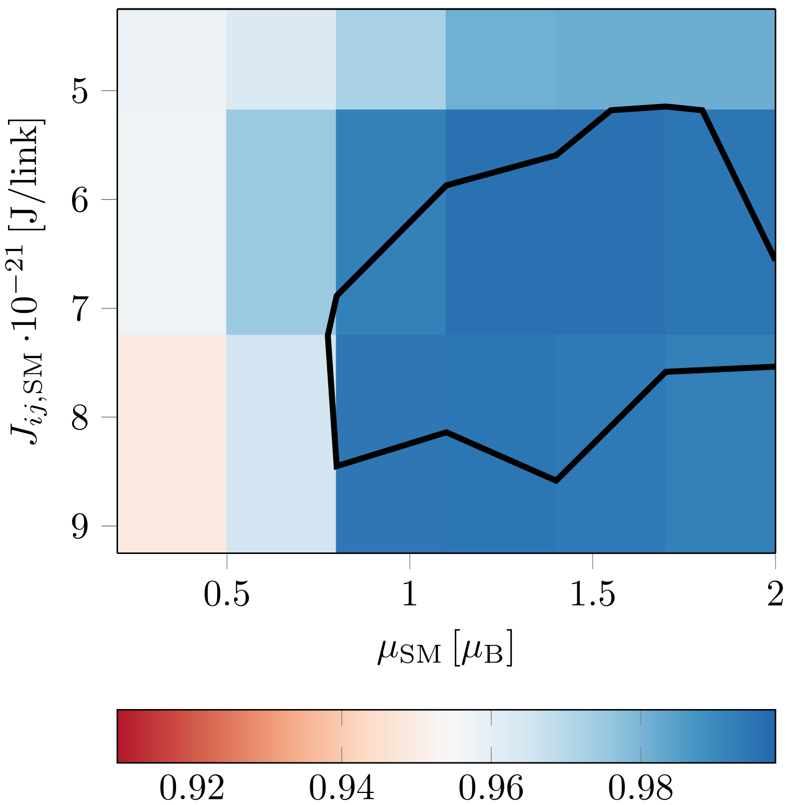

Figure 6.4: Phase diagram of a recording grain with 50% hard magnetic material and 50% soft magnetic material where the fitting parameter $P_{\max}$ can be seen for different configurations of the soft magnetic layer. The contour lines mark the areas with $P_{\max} > 99.2\%$.

Curie temp. T_C [K]	Damping α	Uniaxial anisotropy k_u [J/atom]	$J_{ij,\mathrm{SM}}$ [J/link]	J_{ij} [J/link]	μ_s [μ_B]
748.2	0.1	0	7.25×10^{-21}	$6.13 \cdot 10^{-21}$	1.7

Table 6.1: Material parameters of the optimized soft magnetic material composition.

Thickness HM/SM [%]	T_{peak} [K]	P_{max}
100/0 (HM)	654	0.984
90/10	660	0.984
89/11	660	0.984
88/12	666	0.992
87/13	666	0.992
86/14	672	1.0
85/15	672	1.0
84/16	678	0.976
83/17	678	0.976
82/18	678	0.976
81/19	684	1.0
80/20	690	1.0
79/21	696	1.0

Table 6.2: Results for material compositions with different amounts of hard magnetic (HM) and soft magnetic (SM) ratio. The maximum switching probability is calculated at down-track postition $x = 0\,\text{nm}$ and for a peak temperature T_{peak} which is 20% higher than the Curie temperature of the material composition.

C. Bilayer Composition

With the chosen parameters, the amount of soft and hard magnetic material is optimized. The idea is to use as little soft magnetic material as possible to get narrow transitions, but as much soft magnetic material as necessary to get 100% switching probability in the simulations. Phase diagrams are only computed for the most promising materials. To find candidates, again switching probability curves in the off-track and the down-track direction are calculated.
In Table 6.2 the resulting maximum switching probabilities for different material compositions with T_{peak} which is 20% above the Curie temperature of the material can be seen. One observes that materials with an amount of soft magnetic material of 20% or more have a switching probability of 100% for the indicated temperatures. Thus, the transition curves of these materials are compared to that of pure HM. This is done by fitting the switching probability curves according to Section 3.5.2. The switching probability curves in temperature direction and the corresponding fitting curves of the different materials can be seen in Figure 6.5 for peak temperatures between 400 K and 700 K. Note, the fitting curve of HM with the temperature jitter parameter $\sigma_{\text{T,HM}} = 9.7\,\text{K}$ shows that the switching probability does not reach

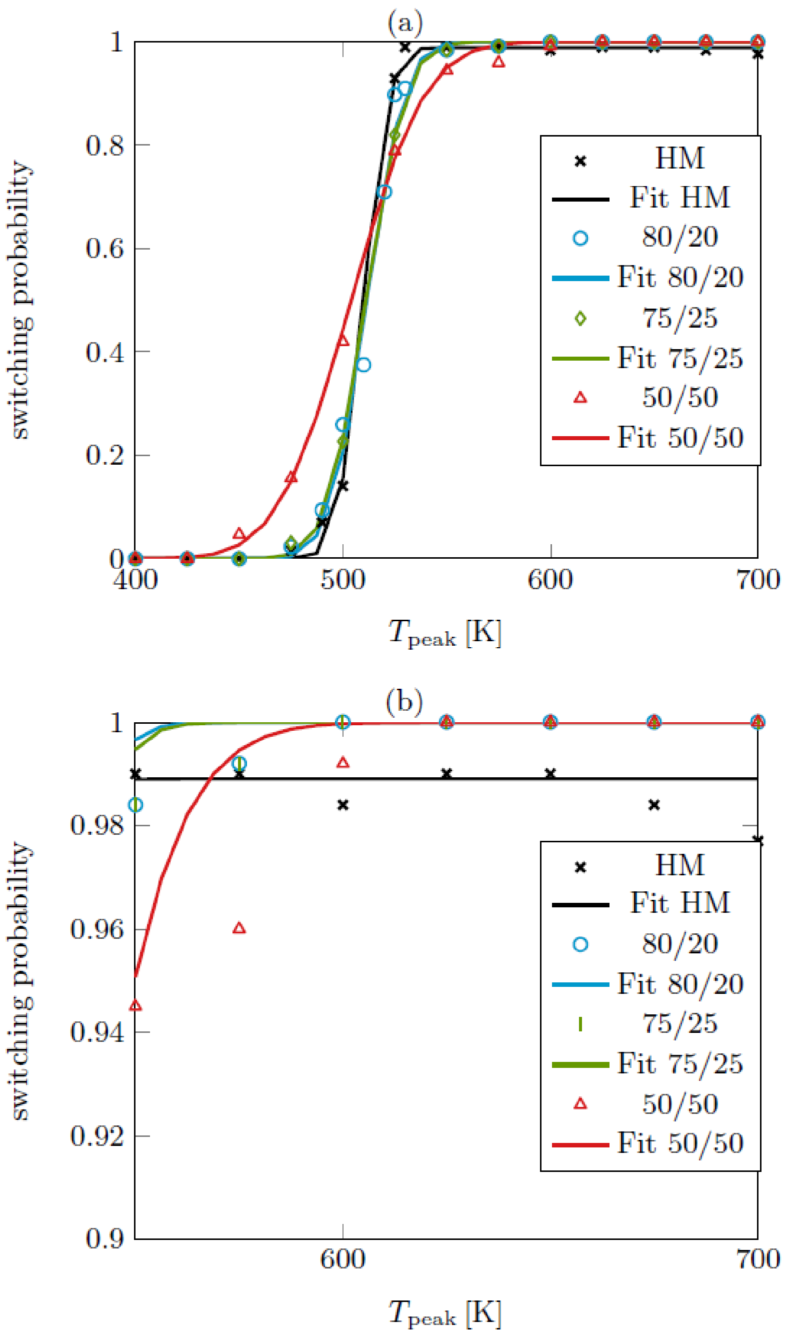

Figure 6.5: (a) $P(T_{\text{peak}})$−curves and corresponding fits of grains with different amounts of soft magnetic ratio at down-track position $x = 0$ nm for different peak temperatures T_{peak}. (b) Zoomed transition and fitting curves for peak temperatures in a range from 550 K to 700 K.

100% in the simulations. For the other material configurations, full switching can be seen for sufficiently high temperatures. Further, in Figure 6.5, one can see that the off-track transition jitter gets larger for a higher amount of soft magnetic material. For 20% soft magnetic material, the transition is the steepest one among the bilayer compositions with $\sigma_{\mathrm{T},80/20} = 14.2\,\mathrm{K}$. Thus, it is much steeper than that of a material with 50% soft magnetic volume fraction for which $\sigma_{\mathrm{T},50/50} = 27.87\,\mathrm{K}$ is almost twice as large as for 80/20. Note that the temperature jitter parameters can again be converted to off-track jitter σ_{off}. The off-track jitter parameters are then $\sigma_{\mathrm{off,HM}} = 0.326\,\mathrm{nm}$, $\sigma_{\mathrm{off},80/20} = 0.46\,\mathrm{nm}$, $\sigma_{\mathrm{off},75/25} = 0.49\,\mathrm{nm}$ and $\sigma_{\mathrm{off},50/50} = 0.93\,\mathrm{nm}$. Actually, the transition of the composition with 20% soft magnetic material is the best compared to that of HM although even here $\sigma_{\mathrm{off},80/20}$ is 41% larger than $\sigma_{\mathrm{off,HM}}$. Additionally, the jitter in down-track direction for one peak temperature and all down-track positions is calculated with higher resolution for pure hard magnetic material, a 50/50 structure and the candidate 80/20 material composition. Since writing of the grain starts at $T_{\mathrm{peak}} = 475\,\mathrm{K}$ for the materials, the jitter is considered at the same peak temperature, $T_{\mathrm{peak}} = 700\,\mathrm{K}$, for all materials. The simulations are done for down-track positions x between $-20\,\mathrm{nm}$ and $22\,\mathrm{nm}$ with a resolution of $\Delta x = 2\,\mathrm{nm}$. Again, in the area of the transitions the resolution is finer, namely $\Delta x = 0.16\dot{6}\,\mathrm{nm}$. In Figure 6.6, the results of these simulations can be seen. For $T_{\mathrm{peak}} = 700\,\mathrm{K}$, the 80/20 material reaches 100% switching probability whereas the switching probability of the pure HM is clearly below 100%. In contrast to the distinct switching probabilities of the materials, the transitions of HM and 80/20 are almost the same. The switching probability curves are again fitted with a Gaussian cumulative distribution function as in eq. (3.46) and eq. (3.47). For both material compositions (HM and 80/20), the steepness of the transitions differs marginally. This can be seen by the fitting values which are $\sigma_{\mathrm{down,HM}} = 0.45\,\mathrm{nm}$ and $\sigma_{\mathrm{down},80/20} = 0.49\,\mathrm{nm}$. For comparison, a composition with 50% hard and 50% soft magnetic material has a fitting value $\sigma_{\mathrm{down},50/50} = 0.64\,\mathrm{nm}$. Since a grain with 80% hard magnetic material and 20% soft magnetic material (80/20) is the optimal material with regard to the off-track and the down-track jitter, a switching probability phase diagram is calculated for 80/20. In Figure 6.7, this switching probability phase diagram is illustrated. In contrast to the phase diagram of HM (see Figure 6.3), the 80/20 phase diagram shows complete switching also for higher peak temperatures. Indeed, the bilayer structure shows 100% switching probability for peak temperatures higher than 550 K in a range from down-track position $x = +10\,\mathrm{nm}$ to $x = -6\,\mathrm{nm}$.

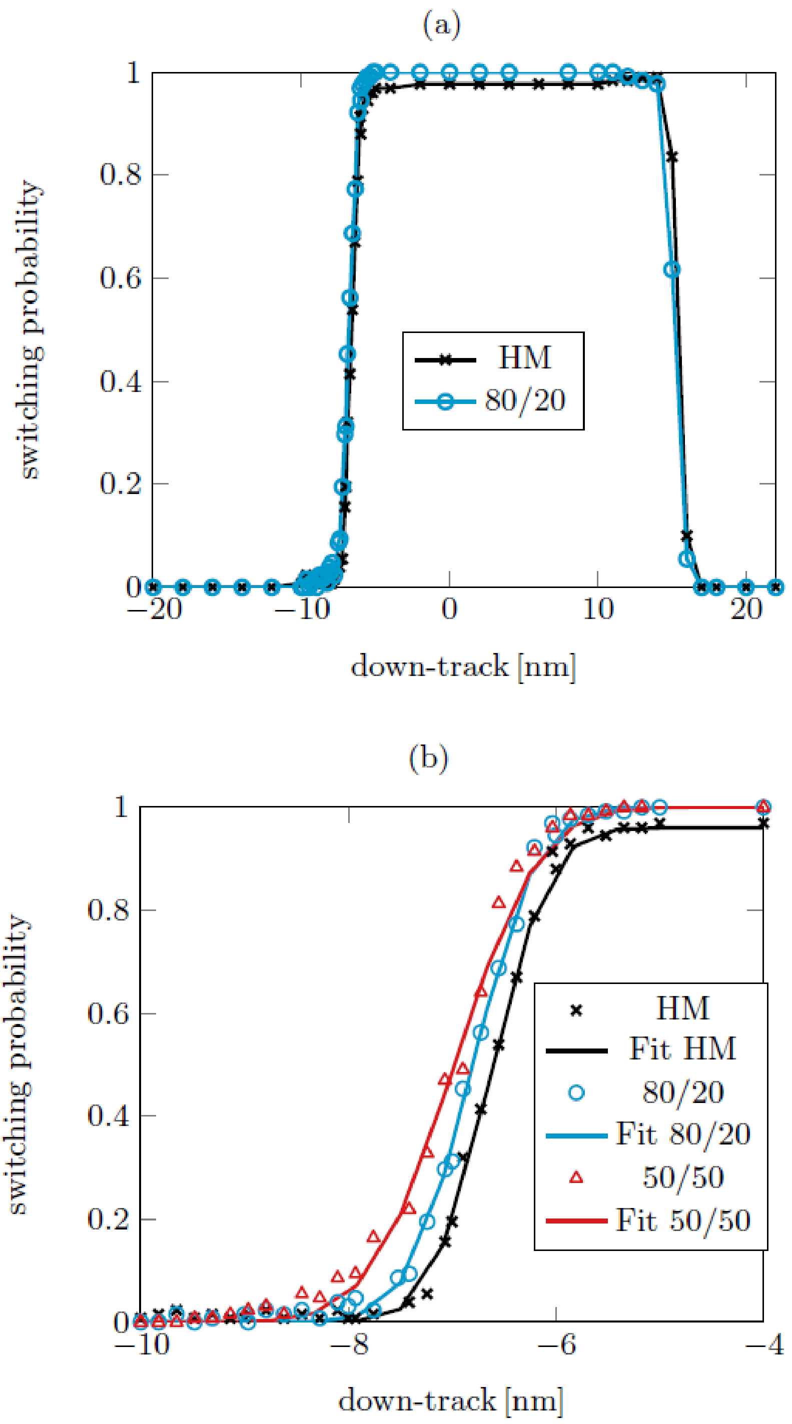

Figure 6.6: Comparison of down-track jitter at a peak temperature $T_{\text{peak}} = 700\,\text{K}$ for a pure hard magnetic grain and a 80/20 hard/soft layer composition (a) for all down-track positions x from - 20 nm to 22 nm. In (b) the jitter in down-track direction is shown more closely for down-track positions between $x = -10\,\text{nm}$ and $x = -4\,\text{nm}$.

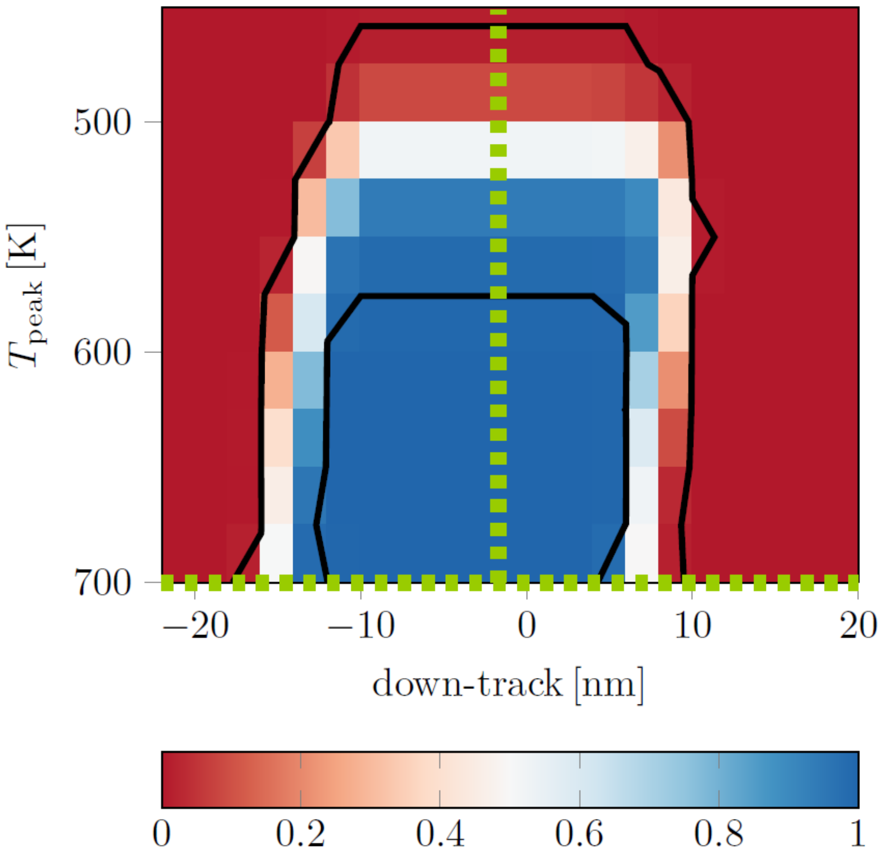

Figure 6.7: Switching probability phase diagram of recording grain consisting of a composition of 80% FePt-like hard magnetic material and 20% Fe like soft magnetic material. The contour lines indicate the transition between areas with switching probability less than 0.8% (red) and areas with switching probability higher than 99.2% (blue). The dashed lines mark the switching probability curves in Figure 6.5 and Figure 6.6.

6.4 Optimization of a Material with Gilbert Damping $\alpha = 0.02$

6.4.1 Modeling Parameters

A. Write Head Parameters

For the simulations, the HAMR model from Section 3.5 is used. The simulations are performed with the atomistic simulation program VAMPIRE [96]. The parameters that are used for the model of the HAMR process are the following:

- Grain diameter $d = 5\,\text{nm}$
- Grain height $h = 8\,\text{nm}$
- FWHM $= 60\,\text{nm}$
- Head velocity $v = 15\,\text{m/s}$
- Field duration $= 0.57\,\text{ns}$
- $T_{\text{min}} = 300\,\text{K}$

Note, most of the parameters differ from those used in Section 6.3. The thermal gradient is 11 K/nm. The write head and material parameters used in this section are parameters which agree with the guidelines of the Advanced Storage Research Consortium [19].

B. Material Parameters

The material parameters for the hard magnetic material can be seen in Table 6.3. For the soft magnetic material, the atomistic spin moment is assumed to be $\mu_s = 1.6\,\mu_B$ which corresponds to a saturation polarization $J_s = 1.35\,\text{T}$. The uniaxial anisotropy constant $k_{u,SM}$ in the soft magnetic layer is initially set to 0 but later varied. The Gilbert damping α_{SM} and the exchange interaction $J_{ij,SM}$ within the soft magnetic material are varied. Experimentally, it is possible to increase the damping constant by doping with transition metals like Gd (gadolinium) or Os (osmium) [132–136]. Thus, also enhanced damping constants α_{SM} larger than 0.02 are considered in the simulations.

Curie temp. T_C [K]	Damping α	Uniaxial anisotropy k_u [J/atom]	J_{ij} [J/link]	μ_s [μ_B]
693.5	0.02	9.124×10^{-23}	6.72×10^{-21}	1.6

Table 6.3: Material parameters of an FePt-like hard magnetic granular recording medium.

6.4.2 Results

Hard magentic grain

First, a switching probability phase diagram for the pure hard magnetic material is computed according to Section 3.5.1. The switching probability in Figure 6.8 is shown as a function of the down-track position x and the peak temperature T_{peak} that corresponds to the off-track position y. The resolution in down-track direction is $\Delta x = 1.5\,\text{nm}$ and that in temperature direction is $\Delta T_{\text{peak}} = 25\,\text{K}$. In each phase point, 128 trajectories are simulated with a length of 1.5 ns. Thus, the phase diagram contains more than 30,000 switching trajectories. From the phase diagram it can be seen that the pure hard magnetic grain shows only two small areas with switching probability larger than 99.2%. In this part, only the down-track jitter parameter σ_{down} is investigated since this is the more interesting parameter in praxis. To determine the down-track jitter, a down-track switching probability curve $P(x)$ for $-20\,\text{nm} \leq x \leq 6\,\text{nm}$ at a fixed temperature $T_{\text{peak}} = T_C + 60\,\text{K} = 760\,\text{K}$ is determined for pure hard magnetic material. The switching probability curve is fitted according to Section 3.5.2. The resulting fitting parameters of the hard magnetic material are $P_{\text{max}} = 0.974$ and $\sigma_{\text{down}} = 0.95\,\text{nm}$.

Media Optimization

To find the best soft magnetic material composition, down-track switching probability curves $P(x)$ are computed for 50/50 bilayer structures with different damping constants α_{SM} and different exchange interactions $J_{ij,\text{SM}}$. After the optimal soft magnetic material composition is found, the ratio between hard and soft magnetic material is optimized. The range in which the parameters are varied can be seen in Table 6.4. Note, that $P(x)$ is computed at different peak temperatures for the different exchange interactions, due to

$$J_{ij} = \frac{3k_B T_C}{\epsilon z}, \tag{6.2}$$

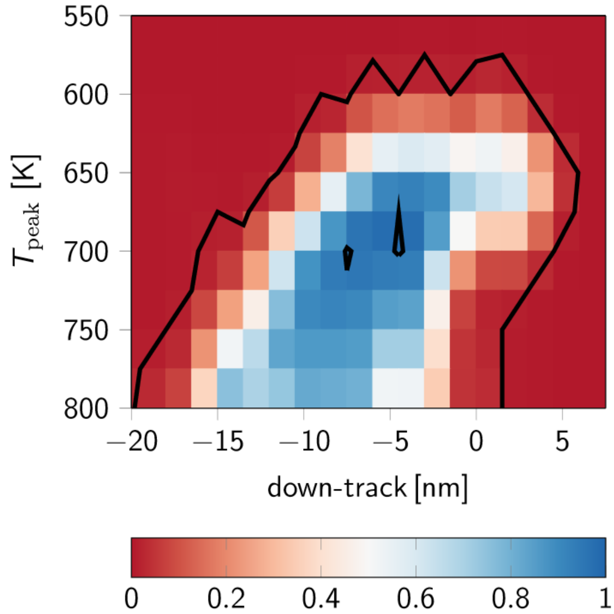

Figure 6.8: Switching probability phase diagram of a pure FePt-like hard magnetic grain. The contour lines indicate the transition between areas with switching probability less than 0.8% (red) and areas with switching probability higher than 99.2% (blue).

Parameter	min. value	max.value
α_{SM}	0.02	0.5
$J_{ij,\text{SM}}$ [J/link]	5.72×10^{-21}	9.72×10^{-21}
$k_{u,\text{SM}}$ [J/atom]	0	$1/2k_{\text{u,HM}} = 4.562 \times 10^{-23}$

Table 6.4: Range in which the different soft magnetic material parameters are varied.

where k_{B} is the Boltzmann constant, z is the number of nearest neighbors and ϵ is a correction factor from the mean-field expression which is approximately 0.86 [96]. The temperature at which $P(x)$ is calculated is chosen to be $T_{\text{C}} + 60\,\text{K}$. The down-track switching probability curves are then fitted according to Section 3.5.2. The down-track jitter parameters as a function of the damping constant and the exchange interaction can be seen in Figure 6.9. Note, the maximum switching probability is 1 for $\alpha \geq 0.1$.

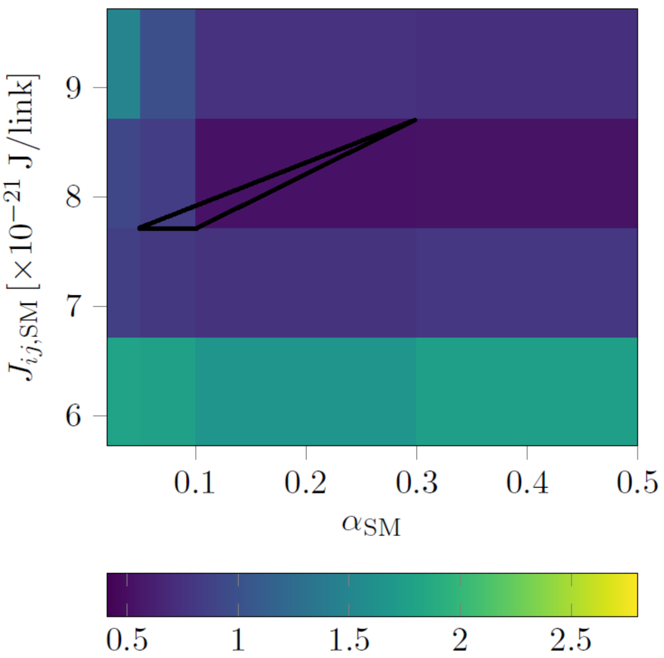

Figure 6.9: Down-track jitter σ_{down} as a function of the damping constant α_{SM} and the exchange interaction $J_{ij,SM}$. The contour line indicates the transition between areas with down-track jitter larger than 0.5 nm (blue,green) and areas with down-track jitter smaller than 0.5 nm (purple).

$k_{u,SM}$ $\times 10^{-23}$ [J/atom]	σ_{down} [nm]	P_{max}
0	0.41	1.0
0.562	0.919	1.0
1.8428 [$= 1/5\, k_{u,HM}$]	1.04	1.0
3.124	0.898	1.0
4.562 [$= 1/2\, k_{u,HM}$]	1.01	1.0

Table 6.5: Resulting down-track jitter parameters and mean maximum switching probability values for soft magnetic materials with different uniaxial anisotropy constants $k_{u,SM}$.

Damping α_{SM}	Uniaxial anisotropy k_u [J/atom]	$J_{ij,SM}$ [J/link]	J_{ij} [J/link]	μ_s [μ_B]
0.1	0	7.72×10^{-21}	7.2×10^{-21}	1.6

Table 6.6: Resulting material parameters for the optimal soft magnetic material composition.

HM/SM	σ_{down} [nm]	P_{max}
100/0 (HM)	0.95	0.974
90/10	1.06	0.969
80/20	0.813	0.998
70/30	0.6	0.988
60/40	0.8	0.999
50/50	0.41	1.0

Table 6.7: Resulting down-track jitter parameters and mean maximum switching probability values for hard magnetic material with Gilber damping $\alpha = 0.02$ and different hard/soft bilayer structures with enhanced damping constants in the soft magnetic material.

The results show that a Gilbert damping $\alpha_{\text{SM}} = 0.1$ together with $J_{ij,\text{SM}} = 7.72 \times 10^{-21}$ J/link leads to the best results with the smallest down-track jitter $\sigma_{\text{down}} = 0.41$ nm and a switching probability $P_{\text{max}} = 1$.
The last soft magnetic parameter that is varied, is the uniaxial anisotropy $k_{\text{u,SM}}$. It is known that the smallest coercive field in an exchange spring medium can be achieved if $K_{\text{SM}} = 1/5 K_{\text{HM}}$ [49, 149]. Here

$$K_{\text{i}} = \frac{n_{\text{at}} k_{\text{u,i}}}{a^3} \ , i \in \{\text{SM}, \text{HM}\} \tag{6.3}$$

are the macroscopic anisotropy constants in J/m^3 with the unit cell size $a = 0.24$ nm and the number of atoms n_{at} per unit cell. $k_{\text{u,SM}}$ is varied between 0 and $1/2 k_{\text{u,HM}} = 4.562 \times 10^{-23}$ J/atom. The resulting fitting parameters are summarized in Table 6.5. It can be seen that the switching probability is one for all varied $k_{\text{u,SM}}$. However, the down-track jitter increases for higher $k_{\text{u,SM}}$. Since for $k_{\text{u,SM}} = 0$ J/atom the jitter is the smallest, this value is chosen for the optimal material composition. In conclusion, the material parameters of the optimized soft magnetic material composition can be seen in Table 6.6.
Next, simulations for different ratios of hard and soft magnetic material are performed. Down-track switching probability curves $P(x)$ are computed for different ratios at $T_{\text{peak}} = 780$ K and the down-track jitter and the mean maximum switching probability are determined. The results are listed in Table 6.7. The results show that a structure with 50% hard magnetic and 50% soft magnetic material leads to the

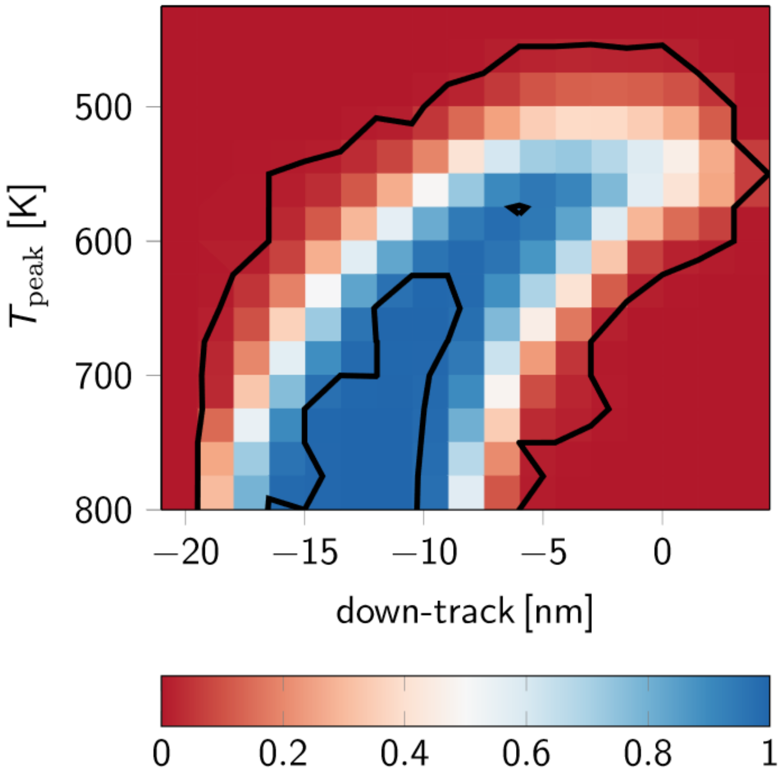

Figure 6.10: Switching probability phase diagram of recording grain consisting of a optimized composition of 50% hard magnetic material with Gilbert damping $\alpha = 0.02$ and 50% soft magnetic material with $\alpha_{\mathrm{SM}} = 0.1$, $k_{\mathrm{u,SM}} = 0\,\mathrm{J/atom}$ and $J_{ij,\mathrm{SM}} = 7.72 \times 10^{-21}\,\mathrm{J/link}$. The contour lines indicate the transition between areas with switching probability less than 0.8% (red) and areas with switching probability higher than 99.2% (blue).

smallest jitter and the highest switching probability. This result differs from the optimized material composition in Section 6.3, where the optimal composition consists of 80% hard magnetic and 20% soft magnetic materials. In Figure 6.10, a switching probability phase diagram of the optimized bilayer structure with 50% hard and 50% soft magnetic material can be seen. It is visible that the switching probability of the structure is larger than 99.2% for a bigger area of down-track positions and peak temperatures. This shows the reduction of DC noise in the optimized structure. The reduction of AC noise can be seen by the reduced jitter values in Table 6.7.

6.5 Areal Density Analysis

To analyse the possible increase of the areal density by using the optimized bilayer structure instead of the pure hard magnetic recording medium, the signal-to-noise ratio is calculated with the help of the analytical model from Section 3.3. The σ_{down} and P_{max} values are those resulting from the atomistic simulations for pure hard magnetic material and the optimized bilayer structure. All other model input parameters are obtained by a least square fit from a switching probability phase diagram computed with a coarse-grained LLB model [114]. According to the considerations of Section 4.2, all values except P_{max} and σ_{down} can be fixed. These fixed fitting parameters are shown in Table 6.8. The SNR is analyzed for areal densities of 2 to 5 Tb/in^2. For the bitsize (bs) at a certain areal density, there are different track width (t) and bit length (b) combinations (t, b) that yield

$$bs = t \cdot b. \tag{6.4}$$

To compute the SNR for a certain (t, b) combination, the reader is scaled in both the down-track and the off-track direction according to the bit length and the track width, respectively. The reader resolution R in down-track direction is scaled by

$$R = R_0 \cdot \frac{b}{b_0} \tag{6.5}$$

where b is the bit length, $R_0 = 13.26\,\mathrm{nm}$ is the initial reader resolution and $b_0 = 10.2\,\mathrm{nm}$ denotes the mean initial bit length according to the ASRC. In off-track direction, the reader width is scaled with the respective track width t. The initial

	5 nm
σ_{off} [K]	22.5
P_{max}	0.995
F_{50} [K]	602
b [nm]	10.2
c [10^{-4} nm/K^2]	3.88
p_2 [K]	839
p_3 [nm]	27.5

Table 6.8: Reference parameters that are evaluated via least square fit of the phase diagrams simulated with the coarse-grained LLB model for grain sizes 5 nm and 7 nm.

AD [Tb/in^2]	Max. SNR [dB] (HM)	x [nm] (HM)	y [nm] (HM)	Max. SNR [dB] (HM/SM)	x [nm] (HM/SM)	y [nm] (HM/SM)
2	13.85	10.0	32.26	16.08	8.06	40.02
3	11.07	6.23	34.52	13.37	5.37	37.53
4	9.46	5.0	32.26	11.55	5.0	32.26
5	7.16	4.3	30.01	9.16	4.69	27.51

Table 6.9: Resulting bit length x and track width y combinations for the maximum SNR at different areal densities (AD) for pure hard magnetic material (HM) and the optimized bilayer structure (HM/SM) with 50% hard magnetic and 50% soft magnetic material.

track width is 44.34 nm. In Figure 6.11(a) and (b) the SNR is shown as a function of the bit length and the track width for pure hard magnetic material and the optimized bilayer structure, respectively. Additionally, the phase plots include the SNR curves for (t, b) combinations that yield areal densities from 2 to 5 Tb/in^2. From the phase diagrams it is visible that higher SNR values can be achieved for the optimized structures than for the pure hard magnetic material in the same bit length − track width range. For example, the SNR for an areal density of 2 Tb/in^2 for the bilayer structure is larger than 15 dB whereas it is between 10 dB and 15 dB for pure hard magnetic material. For each AD there is a (t, b) combination for which the SNR is maximal and which is marked by a dot in the phase plots. In Figure 6.12 the maximum SNR over the areal density is displayed for both structures. The results show that the SNR that can be achieved with the optimized structure is around 2 dB higher than that of the hard magnetic material, if the same areal density is assumed. To get the same SNR, the optimized design allows for an areal density that is 1 Tb/in^2 higher than for the hard magnetic one. Summarizing, the bit length − track width combinations at which the maximum SNR is achieved are given in Table 6.9.

6.5.1 Conclusion

To conclude, the recording medium with high/low T_C grains for heat-assisted magnetic recording for two different Gilbert damping constants $\alpha_{HM} = 0.1$ and $\alpha_{HM} = 0.02$ in the hard magnetic part was optimized. The hard magnetic layer had a low Curie temperature and the soft magnetic layer a high Curie temperature. The goal was to vary the composition and the amount of soft magnetic material such that at the same time both the AC noise and the DC noise are minimized. AC noise determines the distance between neighboring bits in bit-patterned media. DC noise on the

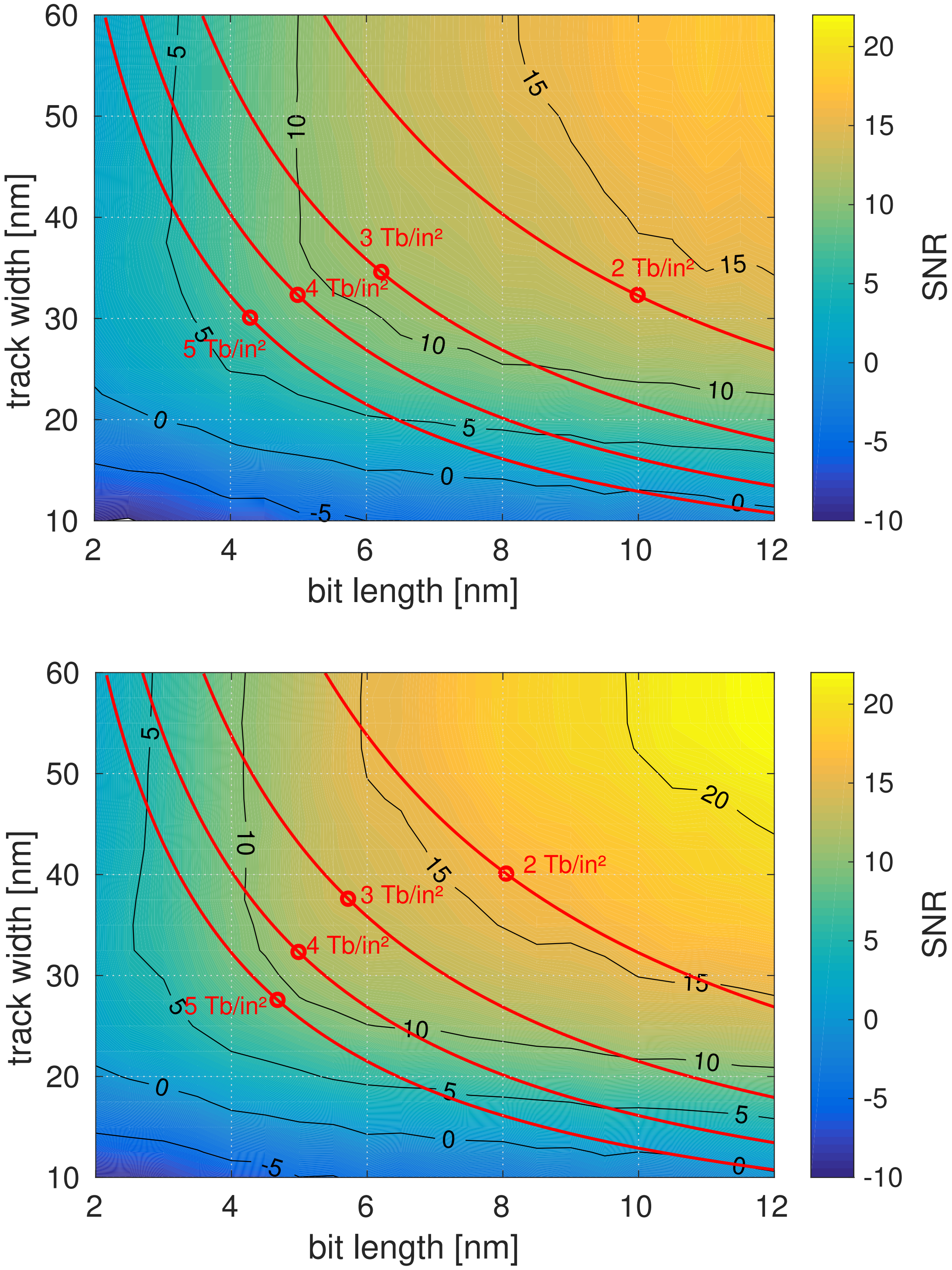

Figure 6.11: Signal-to-noise ratio (in dB) as a function of the bit length and the track width for (a) pure hard magnetic material and (b) the optimized hard/soft bilayer structure. The red lines indicate the bit length – track width combinations that yield 2, 3, 4 and 5 Tb/in^2 areal density. The dots indicate the combination at which the SNR is maximal.

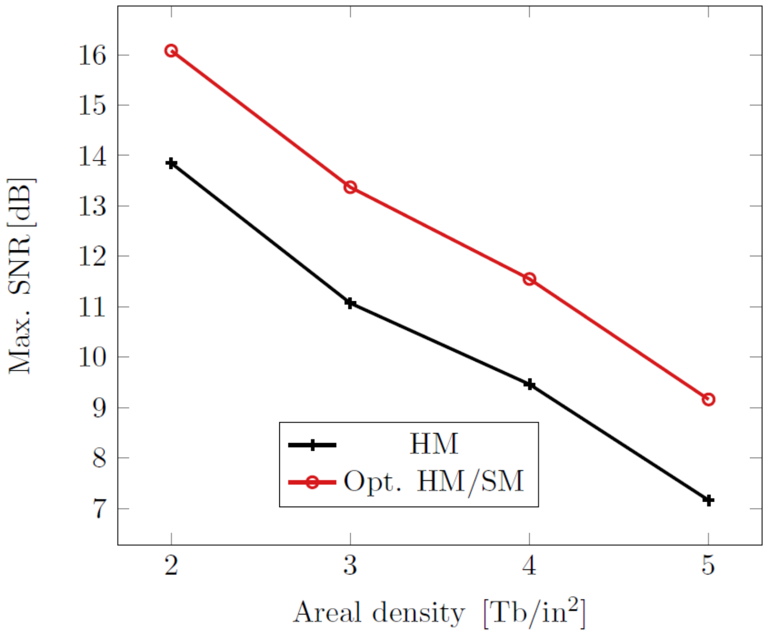

Figure 6.12: Maximum SNR for different areal densities for pure hard magnetic material and the optimized bilayer structure.

other hand limits the switching probability of a bit in bit-patterned media or a grain in granular media. The simulations for a cylindrical recording grain with diameter $d = 5\,\mathrm{nm}$ and two different heights $h = 10\,\mathrm{nm}$ and $h = 8\,\mathrm{nm}$ were performed with the atomistic simulation program VAMPIRE. Different material parameters in the soft magnetic layers were varied. Varying the soft magnetic composition for $\alpha_{\mathrm{HM}} = 0.1$ led to a soft magnetic material with the same atomistic spin moment as the hard magnetic material. A higher Curie temperature was chosen in the soft magnetic layer than in the hard magnetic layer. The used composition is similar to the one used by Vogler *et al* [60]. Further simulations to vary the amount of hard and soft magnetic material showed that more soft magnetic material leads to higher switching probabilities, whereas less soft magnetic material leads to narrower transitions. These results are not surprising. Because of the low coercivity of the soft magnetic layer and the exchange spring effect, the soft magnetic layer helps to switch the magnetization of the hard magnetic layer more reliably. Thus, the switching probability increases for a thicker soft magnetic layer. Furthermore, the soft magnetic layer facilitates switching of the grain in a larger range of temperatures and down-track positions. This increases the jitter in off-track and down-track direction for the bilayer structure.

We showed that a material composition consisting of 20% soft magnetic material and 80% hard magnetic material leads to similar AC and DC noise compared to pure hard magnetic material. The situation is different for hard magnetic materials with damping $\alpha_{HM} = 0.02$. The damping constant of the soft magnetic material was assumed to be enhanced by doping the soft magnetic material with transition metals. The simulations showed that larger damping constants in the soft magnetic layer lead to smaller jitter and higher switching probabilities. A damping constant $\alpha_{SM} = 0.1$, in combination with an exchange interaction $J_{ij,SM} = 7.72 \times 10^{-21}$ J/link and an uniaxial anisotropy constant $k_{u,SM} = 0$ J/atom, led to the best results in terms of small down-track jitter and high switching probability in a wide range of down-track and off-track positions. Interestingly, the soft magnetic composition is almost the same as for the structure with $\alpha_{HM} = 0.1$. Optimizing the amount of hard and soft magnetic material showed that, surprisingly, a higher amount of soft magnetic material leads to smaller down-track jitter. This is not as expected. However, it can be easily explained why a higher amount of soft magnetic material leads to better jitter results for $\alpha_{HM} = 0.02$. Studying the influence of the damping constant on the down-track jitter (see Chapter 4) shows that an increase of the damping constant from 0.02 to 0.1 reduces the down-track jitter by almost 30%. Additionally, the maximum switching probability increases to 1. Since it can be seen that higher damping leads to smaller jitter and higher maximum switching probability, it is reasonable that a higher amount of soft magnetic material with $\alpha_{SM} = 0.1$ leads to a better recording performance. For $\alpha_{HM} = 0.1$, the improved performance due to higher damping was not an issue since the damping constant was 0.1 in both layers. This explains the different ratios of hard and soft magnetic material.
Furthermore, the increase of the areal density can be improved if an optimized bilayer structure is used instead of pure hard magnetic recording material. This was done by analyzing the signal-to-noise ratio for the optimized material compositions with $\alpha_{HM} = 0.02$. The results showed that the areal density of the optimized bilayer structure could be increased by $1\,\mathrm{Tb/in^2}$ to achieve the same SNR as for the pure hard magnetic structure. In other words, that means that at a certain areal density, the SNR was increased by about 2 dB by using the optimized structure. Concluding, the optimized bilayer structure is a promising design to increase the areal storage density by just modifying the recording material.

Chapter 7

Eliminating transition curvature in HAMR

Parts of this chapter have been previously published in [150] and have been reproduced with permission of the coauthors and in accordance with the publisher's policy. Content that was not generated by the author of this thesis is explicitly denoted, copyright is held by American Institute of Physics (AIP).

7.1 Introduction

In HAMR, the heat pulse is used to write high-anisotropy grains with the available small head fields. In general, the Gaussian shaped heat pulse produced by a near-field transducer leads to circular temperature contours within the recording medium. The write field produced by state-of-the art write heads can be assumed to be spatially relatively homogeneous. This in combination with the circular temperature contours always creates transitions with a significant curvature [64, 65], see Figure 7.1. These curved transitions are expected to be a serious problem in the read-back process in HAMR since the signal-to-noise ratio is reduced [94]. Additionally, transition curvature yields edge erasure at higher linear densities. Different methods to efficiently reduce transition curvature in HAMR have been proposed, for example a special write head field design by Zhu *et al* [94, 151, 152] or a flipped head design by Vogler *et al* [93]. In this section, this latter approach is used to design write heads that are supposed to be able to reduce transition curvature in HAMR media. The section is based on the publication by Vogler *et al* [93], where a recording head design to effectively reduce transition curvature is suggested. In the proposal, the difference to a conventional recording head design is that the write and the return pole are switched. Thus, the grain gets written spatially after the return pole and near the near field transducer (NFT) [16] whereas for the standard head the grain is written spatially between the write pole and the NFT (see Figure 7.2). This leads to a differ-

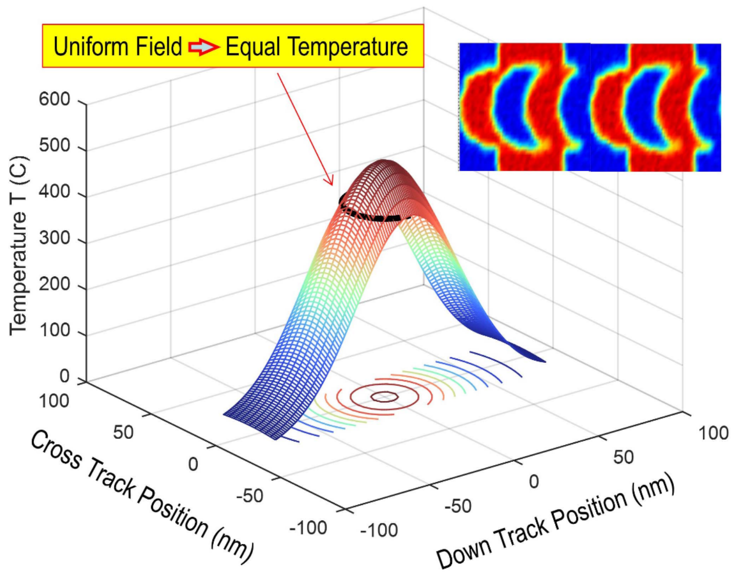

Figure 7.1: Illustration of curved bit transitions due to a Gaussian shaped heat pulse if a uniform write field is applied. The picture is taken from Zhu *et al* [94].

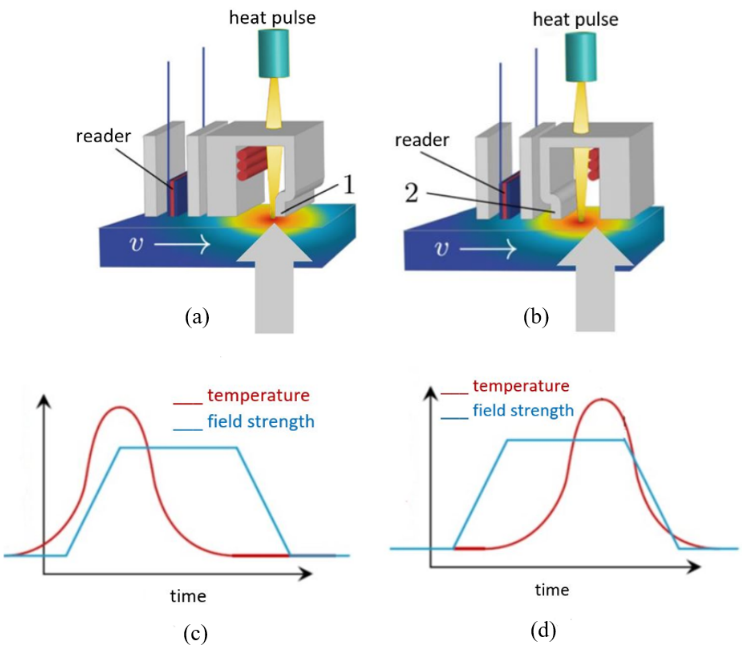

Figure 7.2: Schematic representation of (a) a conventional and (b) a flipped recording head design proposed by Vogler *et al* [93]. In (c) and (d) the temporal evolution of the applied field and the temperature pulse for the conventional and the flipped design, respectively, can be seen. The grey arrows in (a) and (b) indicate the position at which the grains are written.

ent behavior of the write field during the cooling process of the heat pulse. For the conventional design, the applied field is relatively homogeneous during the cooling process. However, for the flipped design, due to the larger distance between the pole tip and the grains to be written, the field is decreasing in down-track direction during cooling which leads to a head field gradient in the same direction as the temperature gradient. At the track edges, the grain is written at the same temperature as before since the write field is sufficiently high. This is due to the fact that at the lower temperatures at the track edges the maximum field is required to reverse the grains. However, in the track center, the transition contour shifts to higher temperature since the write field is quickly decreased in down-track direction. This then leads to a reduction of the transition curvature. Unfortunately, in the former work, the field gradient is assumed to be much higher than in reality.
Thus, the realistic field gradient for an initial flipped design that follows the model of a state-of-the-art recording head design [153, 154] at the position of the cooling of the heat pulse is computed. Since this field gradient is too small to efficiently reduce transition curvature, a write pole that maximizes both the field and the field gradient at the required position is designed. This is done by topology optimization [155], an application of the inverse magnetostatic problem [156]. With the resulting fields and field gradients locally resolved switching probability phase diagrams with a coarse-grained LLB model [114] are computed. From this locally resolved phase diagrams, the resulting curvature can be analyzed.

7.2 Topology Optimization

In today's applications, like magnetic sensors [157, 158], electric generators and motors [159], magnetic materials play a key role. Often it is required that the field produced by the magnet fulfills certain requirements such as high field values or high field gradients. The inverse magnetostatic problem allows to reconstruct the magnetization in a certain magnetic region from a prescribed magnetic field measured outside this magnetic region or to design a magnet to have desired field properties. The inverse magnetostatic problem can on the one hand be used to design the geometry of a magnet to rebuild a certain strayfield [160–162]. On the other hand it is possible to design the magnetization configuration of existing components [163, 164]. Since it is not easy to produce magnets with complicated inhomogeneous magnetization configurations, the design of an optimal geometry is often a more promising

approach.
The inverse magnetostatic problem does not necessarily have a unique solution and is worse conditioned than the forward problem. Thus, solvers of the inverse problem are based on stable and reliable solvers of the forward problem. In this section, the forward problem and the inverse magnetostatic problem are introduced. Furthermore, a general method - the adjoint method - to solve the inverse magnetostatic problem is presented. Last, the density method that is used in this work for topology optimization is explained.

7.2.1 Forward Problem

In the forward problem, the demagnetization field H_d is computed. The demagnetization field is the field that is generated by the magnetization $\boldsymbol{m}$ of a magnetic body. In this work, the simulation of the forward and the inverse problem is based on the work of Huber [165]. The starting point is the Maxwell's equations

$$\nabla \cdot \boldsymbol{B} = 0 \tag{7.1}$$

$$\nabla \times \boldsymbol{H} = 0. \tag{7.2}$$

Equation (7.2) allows to express $\boldsymbol{H}$ as the gradient of a scalar potential u by

$$\boldsymbol{H} = -\nabla u. \tag{7.3}$$

To solve the problem, the space is divided into three regions based on the magnetic characteristics. These regions are (i) the air region Ω_a outside the magnetic region (needed for finite element method (FEM) based computation), (ii) a soft magnetic material region Ω_s and (iii) a permanent magnetic region Ω_p. The magnetic flux density $\boldsymbol{B}$ combined with eq. (7.3) is given by

$$\boldsymbol{B} = \begin{cases} -\mu_0 \nabla u & \text{in } \Omega_\mathrm{a} \\ -\mu_0 \mu_\mathrm{r} \nabla u & \text{in } \Omega_\mathrm{s} \\ -\mu_0 \mu_\mathrm{m} \nabla u + \mu_0 \boldsymbol{M}_0 & \text{in } \Omega_\mathrm{p} \end{cases} \tag{7.4}$$

This results from the following considerations:

- Air region Ω_a

$$\boldsymbol{B}_\mathrm{a} = \mu_0 \boldsymbol{H}_\mathrm{a} = -\mu_0 \nabla u \tag{7.5}$$

with the vacuum permeability $\mu_0\,[= 4\pi 10^{-7}\,\mathrm{Tm/A}]$. $\boldsymbol{H}_\mathrm{a}$ is the magnetic field in the air region.

- Soft magnetic region Ω_s

$$\boldsymbol{B}_\mathrm{s} = \mu_0(\boldsymbol{H}_\mathrm{s} + \boldsymbol{M}_\mathrm{s}) = \mu_0\mu_\mathrm{r}\boldsymbol{H}_\mathrm{s} = -\mu_0\mu_\mathrm{r}\nabla u \tag{7.6}$$

with the relative permeability μ_r and the magnetic field $\boldsymbol{H}_\mathrm{s}$ in the soft magnetic region.

- Hard magnetic region Ω_p

$$\boldsymbol{B}_\mathrm{p} = \mu_0(\boldsymbol{H}_\mathrm{p} + \boldsymbol{M}_0) = \mu_0\mu_\mathrm{m}\boldsymbol{H}_\mathrm{p} + \mu_0\boldsymbol{M}_0 = -\mu_0\mu_\mathrm{m}\nabla u + \mu_0\boldsymbol{M}_0 \tag{7.7}$$

where μ_m is the recoil permeability which is e.g. between 1.05 and 1.2 for rare earth magnets. $\mathbf{H_p}$ is the magnetic field in the permanent region and $\boldsymbol{M}_0 = \boldsymbol{B}_\mathrm{r}/\mu_0$ is the prescribed magnetization vector with $\boldsymbol{B}_\mathrm{r}$ being the remance of the permanent magnet.

In the simulations, μ_r and μ_m are constant. Thus, the method allows only to describe linear material laws.
$\nabla \cdot \boldsymbol{B} = 0$ together with the definition of $\boldsymbol{B}$ in eq. (7.4) is a Poisson equation. To use the finite element method (FEM), a variational approach is used. For this reason eq. (7.1) is multiplied with a test function v and integrated over the region $\Omega = \Omega_\mathrm{a} \cup \Omega_\mathrm{s} \cup \Omega_\mathrm{p}$. Ω is a good approximation to the real space if the air region Ω_a is sufficiently large. This is because the Maxwell's equations only hold for an infinitely large air space. Integration by parts then yields

$$-\int_\Omega \boldsymbol{B}\nabla v\,\mathrm{d}\boldsymbol{r} + \int_{\partial\Omega} \boldsymbol{B}v\boldsymbol{n}\,\mathrm{ds} = 0 \;\;\forall v \text{ in } H_0^1(\Omega). \tag{7.8}$$

The boundary term vanishes since the Sobolev space $H_0^1(\Omega)$ with zero boundary conditions is used for the test functions. This space is taken since the magnetic flux vanishes at the infinitely far away boundary which corresponds to zero Dirichlet boundary conditions in the distant boundary $\partial\Omega = \partial\Omega_\mathrm{a}$. Splitting the region Ω into Ω_a, Ω_s und Ω_p gives an equation

$$a(u, v) = L(v) \tag{7.9}$$

with the bilinear form $a(u, v)$ given by

$$a(u,v) = \int_{\Omega_{\mathrm{a}}} \nabla u \nabla v \mathrm{d}\boldsymbol{r} + \sum_{i=1}^{k} \left(\int_{\Omega_{\mathrm{s}_i}} \mu_{\mathrm{r}_i} \nabla u \nabla v \mathrm{d}\boldsymbol{r} \right) + \sum_{j=1}^{m} \left(\int_{\Omega_{\mathrm{p}_j}} \mu_{\mathrm{m}_j} \nabla u \nabla v \mathrm{d}\boldsymbol{r} \right) \tag{7.10}$$

and the linear form $L(v)$ given by

$$L(v) = \sum_{j=1}^{m} \left(\int_{\Omega_{\mathrm{p}_j}} \boldsymbol{M}_{0_j} \nabla v \mathrm{d}\boldsymbol{r} \right). \tag{7.11}$$

Introducing a discrete subspace $X_h \subset \Omega$ with basic functions $\phi_1, \phi_2, ..., \phi_N$ allows to write the discrete functions

$$u_h = \sum_{i=1}^{N} u_i \phi_i \quad \text{and} \quad v_h = \sum_{j=1}^{N} u_j \phi_j. \tag{7.12}$$

When the discrete functions u_h and v_h are inserted into eq. (7.9), this yields a system of linear equations

$$\boldsymbol{A} \cdot \boldsymbol{u} = \boldsymbol{b} \tag{7.13}$$

with the matrix $\boldsymbol{A}$ and the vector $\boldsymbol{b}$ given by

$$(\boldsymbol{A})_{ij} = a(\phi_i, \phi_j) \tag{7.14}$$

$$(\boldsymbol{b})_j = L(\phi_j). \tag{7.15}$$

Numerically, this system can be solved by the open-source library FEniCS [166, 167] for solving partial differential equations (PDE).

7.2.2 Inverse Problem and Adjoint Method

In contrast to the forward problem, the inverse problem is ill-posed since it is usually bad conditioned and the solution is not unique [156]. To get a unique solution, additional information needs to be provided for example by using a Tikhonov regularization [168]. The inverse problem can be seen as an optimization problem that is constrained by a partial differential equation. The constraining PDE is the forward problem.

Consider a general objective functional J that has to be minimized

$$\min_M J(\boldsymbol{M}, \boldsymbol{H}) = \min_M J(\boldsymbol{M}, u) \tag{7.16}$$

with the magnetization $\boldsymbol{M}$ and the field $\boldsymbol{H}$. A necessary condition for this functional to be minimized is $\mathrm{d}J/\mathrm{d}\boldsymbol{M} \stackrel{!}{=} 0$. $\mathrm{d}J/\mathrm{d}\boldsymbol{M}$ can be written as

$$\frac{\mathrm{d}J}{\mathrm{d}\boldsymbol{M}} = \frac{\partial J}{\partial u}\frac{\partial u}{\partial \boldsymbol{M}} + \frac{\partial J}{\partial \boldsymbol{M}} \tag{7.17}$$

The direct computation of $\partial u/\partial \boldsymbol{M}$ is very inefficient. A better way to compute the derivative is to use the adjoint equation [169, 170]. For this reason, the forward problem is used since the scalar potential u is determined by

$$F = \boldsymbol{A} \cdot \boldsymbol{u} - \boldsymbol{b} = 0 \tag{7.18}$$

To use the adjoint equation, the derivative of the constraint F

$$\frac{\mathrm{d}F}{\mathrm{d}\boldsymbol{M}} = \frac{\partial \boldsymbol{F}}{\partial u}\frac{\partial u}{\partial \boldsymbol{M}} + \frac{\partial F}{\partial \boldsymbol{M}} \tag{7.19}$$

is considered, which yields

$$\boldsymbol{A} \cdot \frac{\partial u}{\partial \boldsymbol{M}} + \frac{\partial \boldsymbol{A}}{\partial \boldsymbol{M}} u = \frac{\partial \boldsymbol{b}}{\partial \boldsymbol{M}} \tag{7.20}$$

$$\Leftrightarrow \frac{\partial u}{\partial \boldsymbol{M}} = \boldsymbol{A}^{-1}\left(-\frac{\partial \boldsymbol{A}}{\partial \boldsymbol{M}} u + \frac{\partial \boldsymbol{b}}{\partial \boldsymbol{M}}\right). \tag{7.21}$$

Inserting eq. (7.21) into eq. (7.17) gives

$$\frac{\mathrm{d}J}{\mathrm{d}\boldsymbol{M}} = \underbrace{\frac{\partial J}{\partial u}\boldsymbol{A}^{-1}}_{(*)}\left(-\frac{\partial \boldsymbol{A}}{\partial \boldsymbol{M}} u + \frac{\partial \boldsymbol{b}}{\partial \boldsymbol{M}}\right) + \frac{\partial J}{\partial \boldsymbol{M}}. \tag{7.22}$$

$(*)$ is the product of a row vector with a matrix and can thus be interpreted as the solution of a linear equation

$$\lambda = \left(\frac{\partial J}{\partial u}\boldsymbol{A}^{-1}\right)^T = \left(\boldsymbol{A}^{-1}\right)^T \left(\frac{\partial J}{\partial u}\right)^T \tag{7.23}$$

$$\Rightarrow \boldsymbol{A}^T \lambda = \left(\frac{\partial J}{\partial u}\right)^T \tag{7.24}$$

This equation eq. (7.24) is called adjoint equation. With the help of the adjoint equation, the gradient of J can be written as

$$\frac{\mathrm{d}J}{\mathrm{d}\boldsymbol{M}} = \lambda^T \left(-\frac{\partial \boldsymbol{A}}{\partial \boldsymbol{M}} u + \frac{\partial \boldsymbol{b}}{\partial \boldsymbol{M}} \right) + \frac{\partial J}{\partial \boldsymbol{M}}. \tag{7.25}$$

Since the gradient needs to vanish, there holds

$$\frac{\partial J}{\partial \boldsymbol{M}} = \lambda^T \left(-\frac{\partial \boldsymbol{A}}{\partial \boldsymbol{M}} u + \frac{\partial \boldsymbol{b}}{\partial \boldsymbol{M}} \right). \tag{7.26}$$

With this, the inverse problem can easily be solved by solving the adjoint equation eq. (7.24). To numerically solve this problem, the library dolfin-adjoint [171, 172] is used. Dolfin-adjoint automatically determines and solves adjoint linear equations using PDEs which are discretized with finite elements.

7.2.3 Density Method

To solve the topology-optimization problem, the density method, which is also known as solid isotropic microstructure with penalization (SIMP), is used [173, 174]. First, the geometry is meshed with a tetrahedral mesh. At each element of the mesh the density ρ of the material is considered and a value between 0 (no material) and 1 (material) is assigned to it. ρ is a filling factor which indicates if the element is assigned with material (1) or not (0). This leads to one optimization variable per element. The final design should only have density values of 0 or 1. This is achieved by using a penalization parameter k to penalize those densities that are intermediate. For a permanent magnetic region $\Omega_\mathrm{p} \subset \mathbb{R}^3$, the magnetization as a function of the density ρ can be written as

$$\boldsymbol{M}(\rho) = \rho^k \boldsymbol{M}_0 \tag{7.27}$$

with the density value $\rho \in [0, 1]$ of one element and the penalization parameter k. $\boldsymbol{M}_0$ is the prescribed magnetization. For hard magnetic materials, $k = 1$ is a good choice [175]. For a soft magnetic design region $\Omega_\mathrm{s} \subset \mathbb{R}^3$, the magnetic susceptibiliy χ can be reformulated as a function of the density to

$$\chi(\rho) = \chi_0 \cdot \rho^k \tag{7.28}$$

and thus for the relative permeability, there holds

$$\mu_r(\rho) = (\mu_{r0} - 1)\rho^k + 1 \tag{7.29}$$

and it can in this way be used for topology optimization. In the case of soft magnetic material, $k = 4$ leads to good results [165].
The topology-optimization problem that needs to be solved is given by

$$\begin{aligned} \text{Find} : \min_{\rho} J(\rho) \\ \text{subject to} : \int_{\Omega_i} \rho(r) dr \leq V; \\ 0 \leq \rho(r) \leq 1, r \in \Omega_i \end{aligned} \tag{7.30}$$

where J is the objective functional, V is the maximum volume of the design as a constraint and $i \in \{s, p\}$ defines the soft and permanent magnetic region, respectively. In words this means that the objective functional J is minimized under the constraints that the density ρ only lives in the prescribed region (dimensions: $(x_{\text{write}} + x_{\text{back}}) \times y_{\text{total}} \times z_{\text{opt}})$) and that ρ only takes values between 0 and 1.
The objective function used to maximize the magnetic field and the $z-$field gradient is given by minimizing

$$\begin{aligned} J(\rho) = \int_{\Omega_{\text{field}}} \frac{1}{|\nabla H_z(\rho)|^2} dr + \int_{\Omega_{\text{field}}} \frac{1}{|H_z(\rho)|^2} dr \\ + \underbrace{\lambda \cdot \int_{\Omega_{\text{opt}}} \rho(1 - \rho) dr,}_{\text{penalization}} \end{aligned} \tag{7.31}$$

where Ω_{opt} is the region of the material that is optimized, $H_z(\rho)$ is the $z-$field and $\nabla H_z(\rho)$ is the gradient of the $z-$field. λ is a penalization parameter. The penalization term is used to force the densities ρ to only take the values 0 and 1.
The topology-optimization problem is solved by a finite element method (FEM) which is based on the open-source library FEniCS [166, 167] for solving partial differential equations (PDEs) and the library dolfin-adjoint [171, 172]. Dolfin-adjoint automatically determines and solves adjoint linear equations using PDEs which are discretized with finite elements. The minimization problem is solved using the L-BFGS-B (Limited-Broyden-Fletcher-Goldfarb-Shanno-Bound-constraint) method [176, 177] which is an optimization method in the family of quasi-Newton solvers and uses a

limited amount of memory. The extension -B extends the L-BFGS solver to problems with bound constraints.

7.3 Write Head Design to Effectively Reduce Transition Curvature

7.3.1 Head Design Parameters

In the topology-optimization simulations, a write head [72, 178] is optimized, which consists of a write and a return pole, a permanent magnet to simulate the core magnetized by a coil and a 50 nm thick soft magnetic underlayer (SUL). Additionally, in some simulations a backshield is considered. All components and the dimensions of the write head are marked in Figure 7.3 and summarized in Table 7.1. The tip of the write pole and the backshield, if considered, are the parts of the write head that are optimized by topology optimization. Except the permanent magnet, all other parts of the write head consist of soft magnetic material.
The material of the recording head is assumed to be FeCo [67]. Hence, a relative permeability $\mu_{\mathrm{r}} = 18000$ and a saturation polarization of 2.4 T are assumed [44]. It is considered that the coil magnetizes the core with 0.8 T in $x-$direction which is modeled by the means of a permanent magnet that is magnetized in $x-$direction with 0.8 T. This field is chosen because then the maximum magnetization of the initial design is slightly below the saturation polarization of the material.
The field and the field gradient are computed and optimized at the position where the recording medium heated by the heat spot produced by the NFT is already cooling down. This position is assumed to be 50 nm away from the pole tip in $x-$direction. Since small head to media spacings (HMS) are needed, to get high areal storage density [179], the HMS is assumed to be 5 nm.
Four different starting geometries are considered. The starting geometries are basic geometries of dimensions $x_{\mathrm{write}} \times y_{\mathrm{total}} \times z_{\mathrm{opt}}$, where the density initially is 1 for each element. During the optimization process, the density of each element is adjusted. The difference between the geometries is the dimension in $x-$direction and whether a backshield is considered or not. The dimensions in $y-$ and $z-$direction are the same for all starting geometries and equal to y_{total} and z_{opt}, respectively. The first geometry to be optimized, is one with dimension $x_{\mathrm{write}} = 100$ nm and no backshield. This one is referred to as Basic$_{100}$. The second geometry also has dimension $x_{\mathrm{write}} = 100$ nm. However, for this geometry a backshield with $x_{\mathrm{back}} = 100$ nm is additionally con-

x_{SUL}	y_{total}	z_{total}	x_{magn}	y_{magn}	z_{magn}	z_{opt}	x_{write}	x_{return}	$\text{dist}_{\text{w,r}}$	x_{back}	$\text{dist}_{\text{f,w}}$	x_{field}	y_{field}
$2\,\mu$m	$5\,\mu$m	$13\,\mu$m	$1\,\mu$m	$3\,\mu$m	$3\,\mu$m	$2\,\mu$m	varied	200 nm	$1\,\mu$m	varied	50 nm	100 nm	100 nm

Table 7.1: Dimensions of an initial flipped recording head design as marked in Figure 7.3.

sidered and optimized. Afterwards, this geometry is called Backshield_{100}. The last geometries are similar to the former ones but with dimensions $x_{\text{write}} = 200\,\text{nm}$ and $x_{\text{back}} = 200\,\text{nm}$. They are labeled Basic_{200} and Backshield_{200}. The x_{write} and x_{back} values of the different geometries are summarized in Table 7.2.
After the optimal head designs are determined via topology-optimization, additional simulations with magnum.fe [180] that include a coil instead of a permanent magnet are performed. These coil-simulations are performed in order to determine realistic fields with the optimized head designs. Here, all parts of the write head are considered to be soft magnetic with the above material parameters. A head design with simulated coil can be seen in Figure 7.4. The current density inside the coil is assumed to be $2.5 \times 10^{10}\,\text{A/m}^2$, which is below the current density limit of $10^{12}\,\text{A/m}^2$, [181].

7.3.2 Results

A. Field Gradients

Forward simulations show that the field gradient of the initial flipped design, which follows a state-of-the-art head design [153,154], at 50 nm distance from the write pole is approximately 2.2 mT/nm. In Figure 7.5 the resulting fields from simulations with and without the coil with the optimized geometries are plotted. Figure 7.5(a) and (b) show the change of the magnitude of the external field over the down-track position. The results show that the best outcome can be achieved for a geometry with a pole tip with $x_{\text{write}} = 200\,\text{nm}$ and an additional backshield with $x_{\text{back}} = 200\,\text{nm}$. Here, the maximum field gradient is 11.8 mT/nm. The optimized *Backshield*$_{200}$ geometry is shown in Figure 7.6. Note that all optimized geometries are similar and show a tapered shape. Recapitulating, the resulting write fields and field gradients for the different geometries are summarized in Table 7.2.

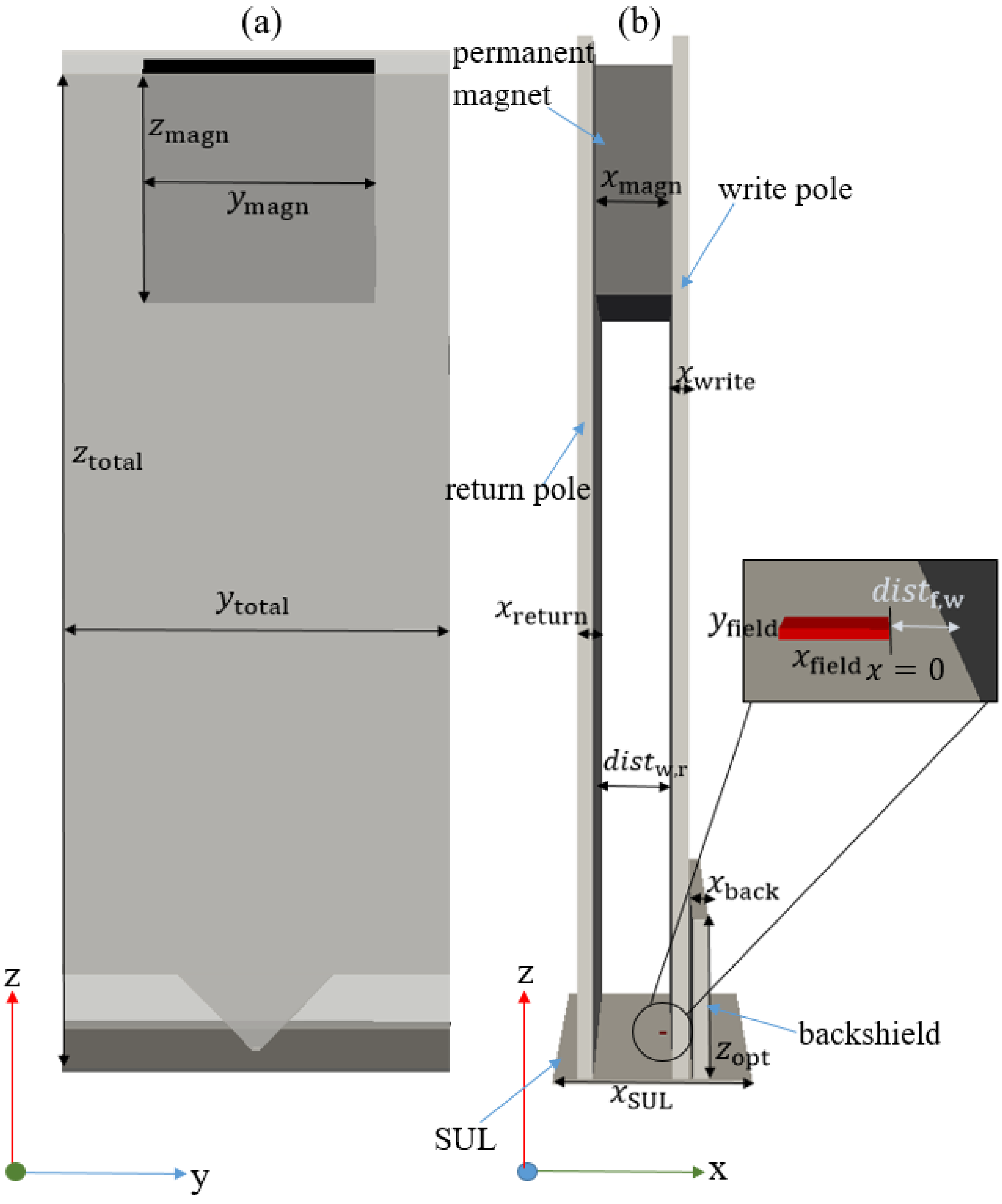

Figure 7.3: Schematic representation with dimensions of the initial flipped head design. The dimensions can be seen in Table 7.1. In (a) the front view and in (b) the side view can be seen.

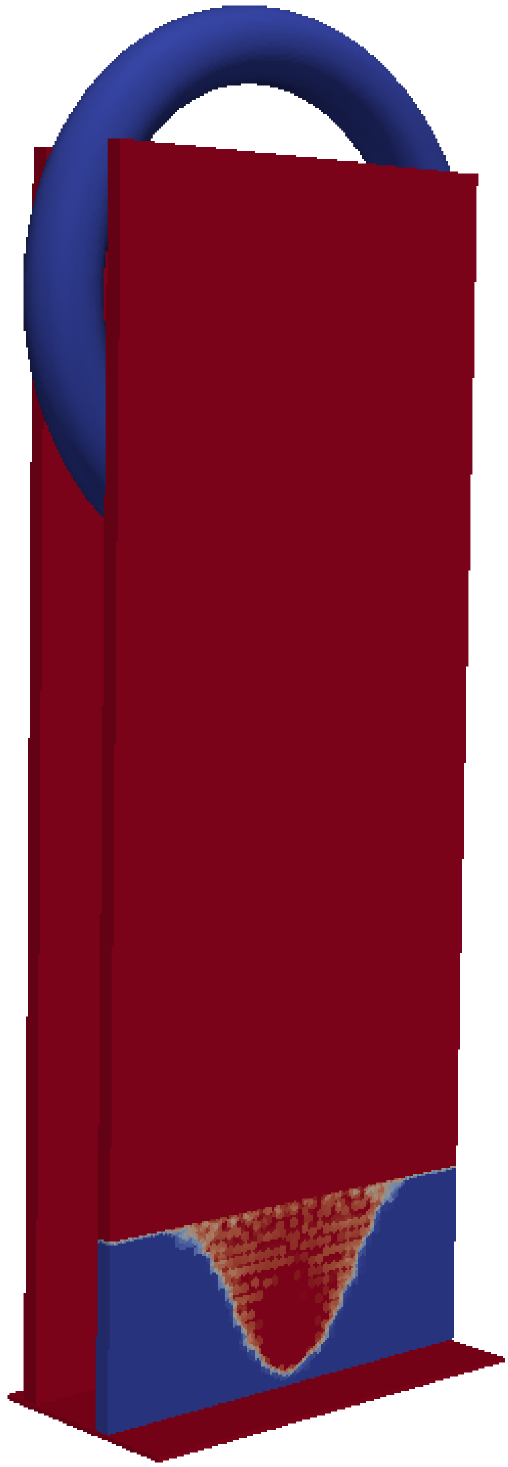

Figure 7.4: Schematic representation of the $Basic_{200}$ geometry simulated with a coil. The color red indicates areas where the filling factor ρ is 1 (magnetic material), whereas blue indicates ares with $\rho = 0$ (no material). The coil is blue since it is not made out of magnetic material.

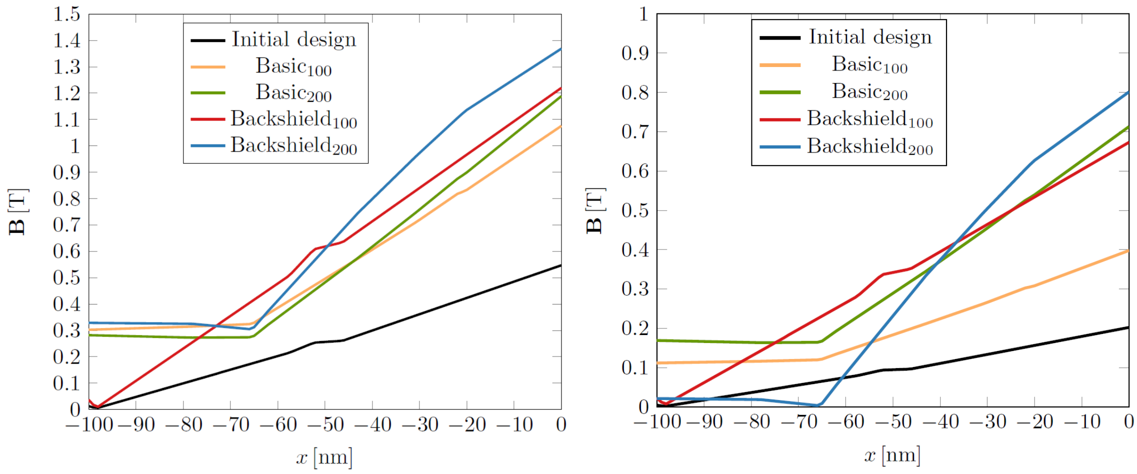

Figure 7.5: Comparison of the fields of the topology optimized geometries for an FeCo like head material. The magnetic field is plotted over the $x-$length of the 100 nm × 100 nm wide fieldbox. At $x = 0$, the fieldbox is 50 nm away from the edge of the write pole. On the left the preliminary results after the topology optimization without the coil are displayed, on the right the realistic fields with an assumed coil are plotted.

Geometry	x_{write} [nm]	x_{back} [nm]	$\mu_0 H$ [T]	Max. $\mu_0 dH/dx$ [mT/nm]
Conventional	100	—	0.8	0
Initial flipped design	100	—	0.2	2.2
Basic$_{100}$	100	—	0.4	4.1
Basic$_{200}$	200	—	0.7	8.6
Backshield$_{100}$	100	100	0.67	8.1
Backshield$_{200}$	200	200	0.8	11.8

Table 7.2: Resulting fields and field gradients produced by the write heads which are optimized with the help of topology optimization for an FeCo like head material. The field and field gradient of a conventional head are added for comparison.

(a)

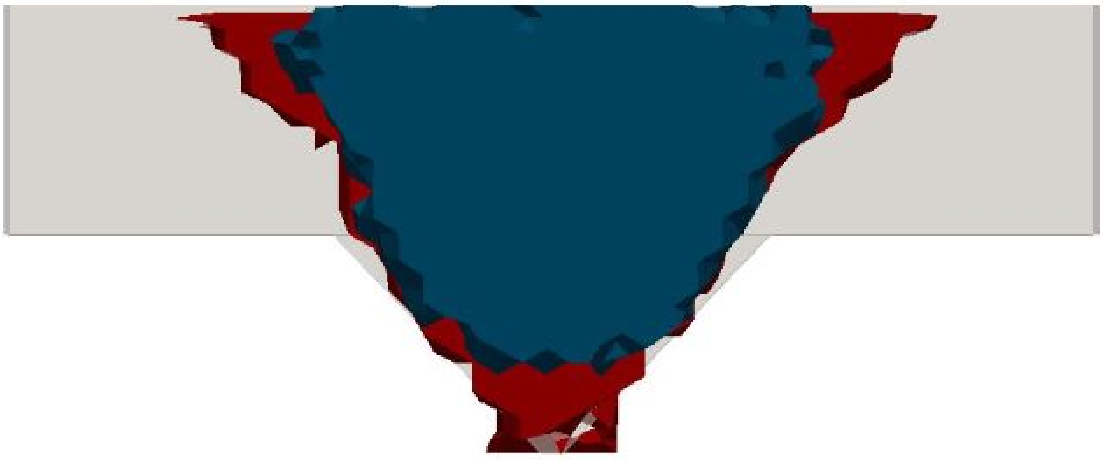

(b)

Figure 7.6: Comparison of the initial flipped head design (grey) and the topology optimized write pole (red) with a backshield (blue) with $x_{\mathrm{write}} = 200\,\mathrm{nm}$ and $x_{\mathrm{back}} = 200\,\mathrm{nm}$ (red). (a) Front view and (b) rear view with backshield of the optimized write pole.

B. Curvature Reduction

To analyse the curvature reduction, switching probability phase diagrams are computed with the help of a coarse-grained model from Section 3.2 based on the stochastic Landau-Lifshitz-Bloch equation [114] for an FePt-like granular recording medium as described in Section 3.5.1. The following write head parameters are used:

- FWHM = 60 nm
- Head velocity $v = 15\,\mathrm{m/s}$
- Field duration = 0.57 ns
- $T_{\mathrm{min}} = 300\,\mathrm{K}$

The shift (h_{shift}) between the heat pulse and the write field, which is an important parameter in the work of Vogler *et al* [93], is adjusted according to the former publication.
The material parameters of the medium can be seen in Table 7.3. In each phase point 128 simulations are performed. In the phase diagrams the switching probability is shown as a function of the down-track position x and the off-track position y. First, the phase diagram is computed for a spatially homogeneous field which corresponds to a conventional recording head design. Additionally, switching probability phase diagrams for optimized geometries with field gradients of 8.6 mT/nm ($Basic_{200}$), 8.1 mT/nm ($Backshield_{100}$) and 11.8 mT/nm ($Backshield_{200}$) are computed. The geometries with field gradients 2.2 mT/nm (*Initial flipped*) and 4.1 mT/nm ($Basic_{100}$) are not further considered since the phase diagrams show too much noise to get reliable results due to the low maximum fields. Note, that different write fields (see Table 7.2) are used for the simulations with different field gradients as seen in Table 7.2. In Figure 7.7, the resulting switching probability phase diagrams are displayed. There are some visible differences between the phase diagrams of the different field gradients.
One can see that for the flipped designs the recording performance is worse than for the conventional design where a homogeneous field is assumed. This can be seen by the increase of jitter in down-track direction and the reduction of the maximum switching probability P_{max} and can be explained as follows: First, note that the origin of the Gaussian shaped heat pulse is at $x = 0\,\mathrm{nm}$ and $y = 0\,\mathrm{nm}$. The full width at half maximum is 60 nm for the heat pulse. This means a heat pulse with $T_{\mathrm{write}} = 800\,\mathrm{K}$ would heat all pure hard magnetic grains within an off-track distance

Curie temp. T_C [K]	Damping α	Anisotropy const. K_1 [MJ/m^3]	Anisotropy field $\mu_0 H_k$ [T] at 300 K	J_s [T]	height h [nm]	diameter d [nm]
693.5	0.02	6.6	10	1.35	8	5

Table 7.3: Material parameters of an FePt-like hard magnetic granular recording medium. Note, that different material parameters for the recording medium are used compared to the original work of Vogler *et al* [93].

of $0 - 17$ nm above their Curie temperature. Without an external applied field all of these grains would end up with a switching probability of 50% after cooling, since there is no bias. Only by applying a field the grains can be magnetized along the $z-$direction. But for the flipped head design the field is reduced during cooling and especially for Figure 7.7(c) the maximum field is about 15% lower than that for the conventional design in Figure 7.7(a). This means that the field is too weak for the flipped design to align 100% of the corresponding grains within the effective recording time window, yielding noise along the whole track in down-track direction.
P_max and the jitter can be determined by fitting the $P(x)-$curve at one temperature with a Gaussian cumulative distribution function as described in Section 3.5.2. The temperature at which the down-track jitter is determined is $T_\mathrm{peak} = 760$ K. The resulting jitter and P_max values are summarized in Table 7.4. Additionally, it can be seen that the grains at larger off-track positions are written for increasing field gradients. The various write fields lead to writing of the grains at different peak temperatures. For smaller write fields the grains are written at higher temperatures only whereas they are written at lower temperatures for higher fields. The convention

$$T_\mathrm{peak}(y) = (T_\mathrm{write} - T_\mathrm{min})e^{-\frac{y^2}{2\sigma^2}} + T_\mathrm{min}. \tag{7.32}$$

shows that with higher write fields the off-track edge of a bit shifts to larger off-track positions, because the minimum temperature necessary to write a grain is smaller.
For a detailed analysis of the transition curvature, the full down-track range Δx in which the bit is written with $P_\mathrm{max} \geq 50\%$ is computed. Δx is marked in Figure 7.7 as the distance between the dashed black lines. Because of the different off-track widths Δy in the phase diagrams for the different geometries, it is necessary to scale the curvature parameter with Δy. This is done, since the track width is usually kept constant in magnetic recording. In reality the track-width can be controlled by adjusting the write temperature T_write or the full width at half maximum [182]. With the curvature parameter $c = \Delta x/\Delta y$, the curvature can be reliably analyzed. This

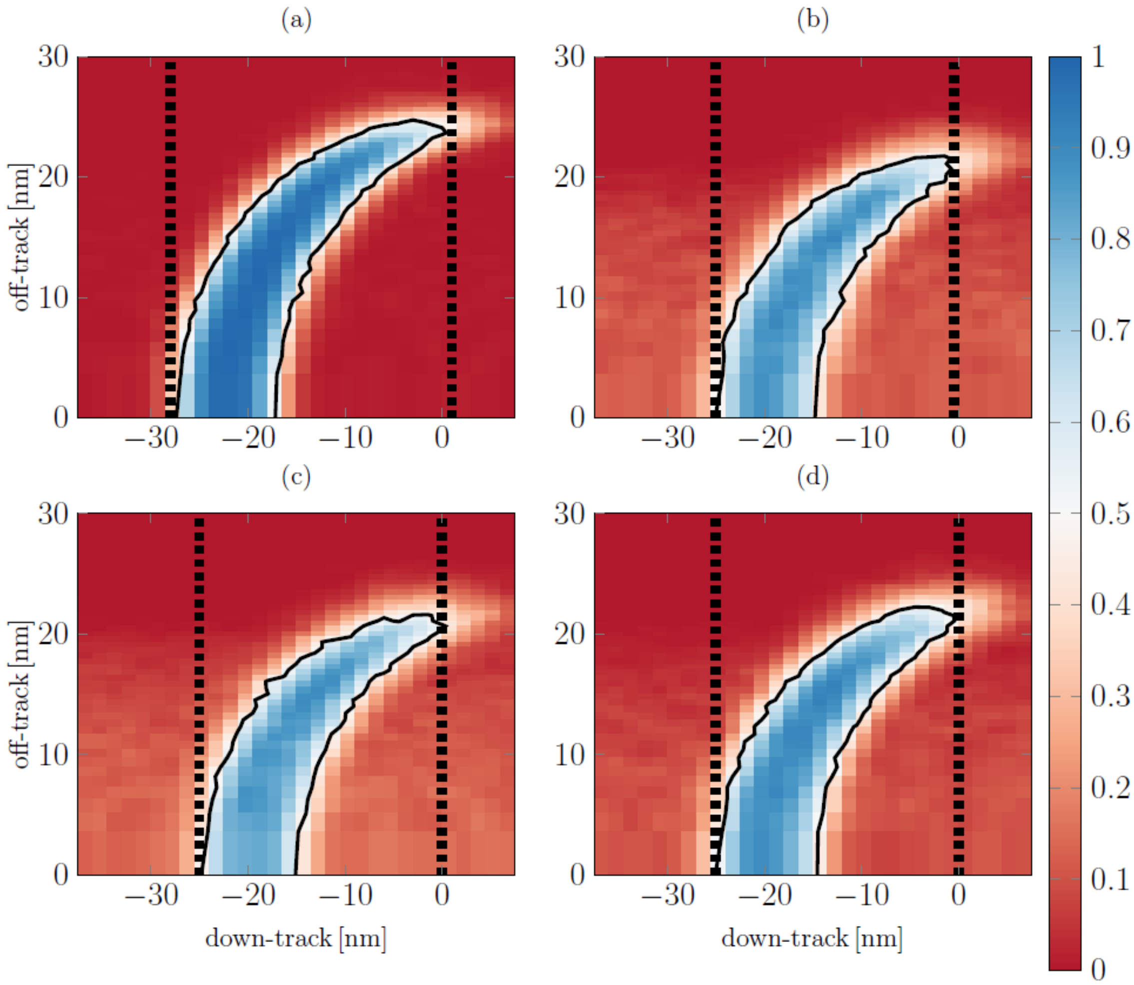

Figure 7.7: Switching probability phase diagrams of (a) a conventional head with a homogeneous write field and the flipped design with optimized field gradients (b) $\mu_0 dH/dx = 8.6\,\mathrm{mT/nm}$ ($Basic_{200}$), (c) $\mu_0 dH/dx = 8.1\,\mathrm{mT/nm}$ ($Backshield_{100}$) and (d) $\mu_0 dH/dx = 11.8\,\mathrm{mT/nm}$ ($Backshield_{200}$) in combination with pure hard magnetic recording material. The dashed black lines indicate the maximum and minimum down-track position x with $P(x) = 50\%$.

Geometry	c [%]	P_{max} [%]	σ_{down} [%]
$Basic_{200}$	+1.4	−5.5	+118.7
$Backshield_{100}$	+3.8	−7	+113.5
$Backshield_{200}$	−1.35	−2.3	+28.4

Table 7.4: Resulting curvature, P_{max} and jitter reduction/increase of the different flipped head designs in combination with a pure hard magnetic recording material given with regard to a conventional recording head design. The values of the conventional design are $c = 1.05974$, $P_{\mathrm{max}} = 0.95$ and $\sigma_{\mathrm{down}} = 0.974\,\mathrm{nm}$.

curvature parameter is used instead of that given by Vogler *et al* [93] since the one in the latter work is strongly depending on the fitting procedure of the curvature with a second-order polynomial. In contrast to this, the curvature parameter c in this work is only dependent on the track width Δy and Δx which are both unique values. The curvature analysis shows that the curvature is increased for both the $Basic_{200}$ and the $Backshield_{100}$ design compared to the conventional design. The curvature reduction for the $Backshield_{200}$ flipped head design with a field gradient of 11.8 mT/nm is about 1.35%. Detailed information about the curvature parameters can be seen in Table 7.4.

C. Exchange Spring Recording Medium

Since the curvature reduction is only small for pure hard magnetic recording media in combination with the flipped head design, a bilayer structure with 50% hard and 50% soft magnetic material is tested as recording material. The total height of the grains is again $h = 8\,\mathrm{nm}$. The material parameters of the soft magnetic composition can be seen in Table 7.5. Phase diagrams for the different head designs are calculated and shown in Figure 7.8. Again, the jitter σ_{down} and P_{max} are determined from the switching probability phase diagrams and compared in Table 7.6. Due to the higher Curie temperature of the exchange coupled recording medium, the down-track jitter is determined at 800 K. For the exchange coupled recording material the behavior of the curvature reduction is even worse than that of the pure hard magnetic recording media. For the $Backshield_{200}$ head design the decrease is only 0.08% compared to the conventional design. However, the maximum switching probability stays 100% and the down-track jitter decreases.

Curie temp. T_C [K]	Damping α	Anisotropy const. K_1 [MJ/m^3]	J_s [T]
740.9	0.1	0	1.35

Table 7.5: Material parameters of the soft magnetic composition of the bilayer structure.

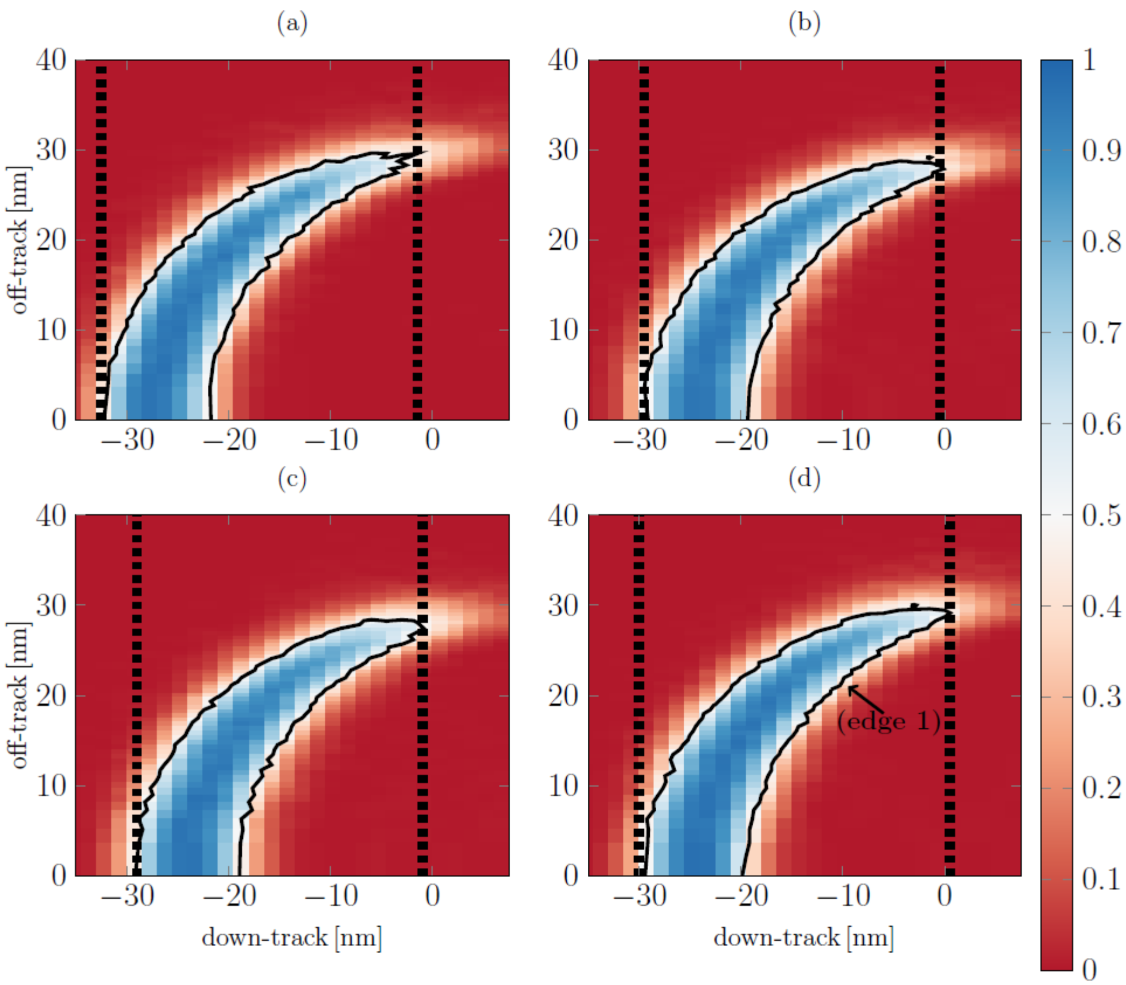

Figure 7.8: Switching probability phase diagrams of (a) a conventional head with $\mu_0 dH/dx$ = 0 mT/nm and the flipped design with optimized field gradients (b) $\mu_0 dH/dx$ = 8.6 mT/nm, (c) $\mu_0 dH/dx$ = 8.1 mT/nm and (d) $\mu_0 dH/dx$ = 11.8 mT/nm in combination with an exchange coupled bilayer structure.

Geometry	c [%]	$P_{\max}$ [%]	σ_{down} [%]
$Basic_{200}$	$+1.38$	-2.5	-16.2
$Backshield_{100}$	$+1.9$	-1.19	-4.7
$Backshield_{200}$	-0.08	$+/-0.0$	-19

Table 7.6: Resulting curvature, $P_{\max}$ and jitter reduction/increase of the different flipped head designs in combination with an exchange spring recording medium given with regard to a conventional recording head design with the same recording material. The values of the conventional design are $c = 0.96414$, $P_{\max} = 1.0$ and $\sigma_{\text{down}} = 0.5\,\text{nm}$.

D. Comparison with ERTW Model

To understand why both the pure hard magnetic and the exchange coupled media show almost no curvature reduction, the results are compared to theoretical considerations with the effective recording time window (ERTW) model described in Section 3.4 [93]. For the $Backshield_{200}$ geometry, the theoretically expected curvature reduction is about 1% for the pure hard magnetic recording material compared to the conventional design. This agrees very good with the curvature reduction resulting from the LLB simulations. For the exchange spring bilayer structure, the ERTW model predicts a curvature reduction of about 1.7%. The very small value achieved by the LLB simulation (-0.08%) results from the shift of edge 1 (marked in Figure 7.8(d)) that happens around the down-track position $x = 0\,\text{nm}$. This shift does not happen in the analytical ERTW model and comes from the stochastic nature of the LLB model.
Additionally, with the ERTW model, it can be analyzed with reasonable computational effort how the transition curvature reduction depends on the field gradient. The resulting curvature reduction values can be seen in Table 7.7. They display that the curvature reduces linearly with the field gradient. Moreover, a higher potential for the curvature reduction can be seen for the exchange spring bilayer structure.

However, even with field gradients up to 40 mT/nm, the bilayer structure did not show as high curvature reduction as the exchange spring media used by Vogler *et al.* The curvature reduction for the exchange coupled recording media (EC1 and EC2 - see Table 7.8) from [93] resulting from the ERWT model and evaluated with the curvature definition $c = \Delta x/\Delta y$ are shown in Table 7.9. The much smaller curvature reduction effect can most likely be explained by the different damping constants used in the hard and soft magnetic material. In the work by Vogler *et al*, the damping constant is $\alpha_{\text{HM}} = 0.1$ whereas it is $\alpha_{\text{HM}} = 0.02$ in this work. The different damping

Field gradient [mT/nm]	c [%] HM	c [%] HM/SM
12	-1.0	-1.7
16	-1.6	-3.64
20	-2.09	-5.58
24	-2.59	-7.5
28	-3.38	-9.48
32	-4.6	-11.4
36	-5.2	-13.11
40	-5.8	-14.2

Table 7.7: Curvature reduction in % compared to a conventional design for pure hard magnetic recording material (HM) and an exchange coupled bilayer structure (HM/SM).

Parameter	EC1	EC2
$k_{\mathrm{u,hard}}$ [$\cdot 10^{-23}$ J/atom]	9.12	9.12
$\mu_{\mathrm{S,hard}}$ [μ_{B}]	1.7	1.7
α_{HM}	0.1	0.1
h_{hard} [nm]	5	5
$T_{\mathrm{C,hard}}$ [K]	644	537
$k_{\mathrm{u,soft}}$ [$\cdot 10^{-23}$ J/atom]	0	0
$\mu_{\mathrm{S,soft}}$ [μ_{B}]	1.7	1.7
α_{SM}	1.0	1.0
h_{soft} [nm]	5	5
$T_{\mathrm{C,soft}}$ [K]	537	795

Table 7.8: Material parameters for the exchange coupled recording materials used by Vogler *et al* [93].

constants lead to different dH_{c}/dT gradients. The dH_{c}/dT gradients for the exchange coupled recording media (EC1 and EC2) from [93] compared to that of the bilayer structure used in this work (HM/SM) can be seen in Figure 7.9. The dH_{c}/dT gradient of the HM/SM structure is with 16.95 mT/K significantly larger than that of the EC-structures with 4.8 mT/K and 5.6 mT/K for EC1 and EC2, respectively. By taking the reciprocal of these gradients, one gets the change of the freezing temperature if the coercive field changes by 1 mT. The gradients dT/dH_{c} are then 0.06 K/mT, 0.2 K/mT and 0.17 K/mT for the HM/SM structure, the EC1 and the EC2 structure, respectively. Consequently, the freezing temperature reduces less for the HM/SM structure than for the EC media if the coercive field is reduced during the HAMR process. This results in a higher freezing temperature for the HM/SM structure and

Material	FWHM [nm]	c [%]
EC1	20	-10
EC1	40	-16
EC2	40	-29.5
EC2	60	-40

Table 7.9: Resulting curvature reduction from phase diagrams computed with the ERTW model for the exchange coupled materials used by Vogler *et al.* The curvature definition is $c = \Delta x/\Delta y$ and it is compared to the same material with a conventional design. The field gradient is assumed to be 40 mT/nm.

thus in a narrower ERTW. The consequence is a decreased curvature reduction effect. This shows that damping plays a key role for the curvature reduction.

7.3.3 Conclusion

To conclude, in this section it was tried to optimize the design of the write pole of a recording head for heat-assisted magnetic recording in order to reduce transition curvature. The write pole of the head was optimized in a way to maximize both the $z-$field and the $z-$field gradient at the position where the applied heat pulse is cooling down. This was done with the help of topology optimization which is an application of the inverse magnetostatic problem. Different starting geometries were considered. The comparison of the different geometries to a conventional recording head design showed the best results for a write pole and an additional backshield which both have dimension 200 nm in down-track direction. The resulting field gradient is then 11.8 mT/nm with a maximum field of 0.8 T. The optimized geometries are all similar. They all have smooth edges, a tapered shape with a tip in the middle and the peak is skewed in $x-$direction such that the distance of the pole tip to the recording medium is close to the fieldbox and larger on the side away from it (see Figure 7.6). An option to further increase the field gradient produced by the write pole is a design where the NFT is closer to the write pole.
The switching probability phase diagrams of FePt-like magnetic recording media was calculated for the different optimized field gradients. It is noteworthy that the switching performance, in terms of down-track jitter and maximum switching probability, for all flipped head designs is worse than that of the conventional head design. Both, the AC and the DC noise increase for the flipped head designs. The performance loss results most likely from the smaller write fields that are produced by the flipped

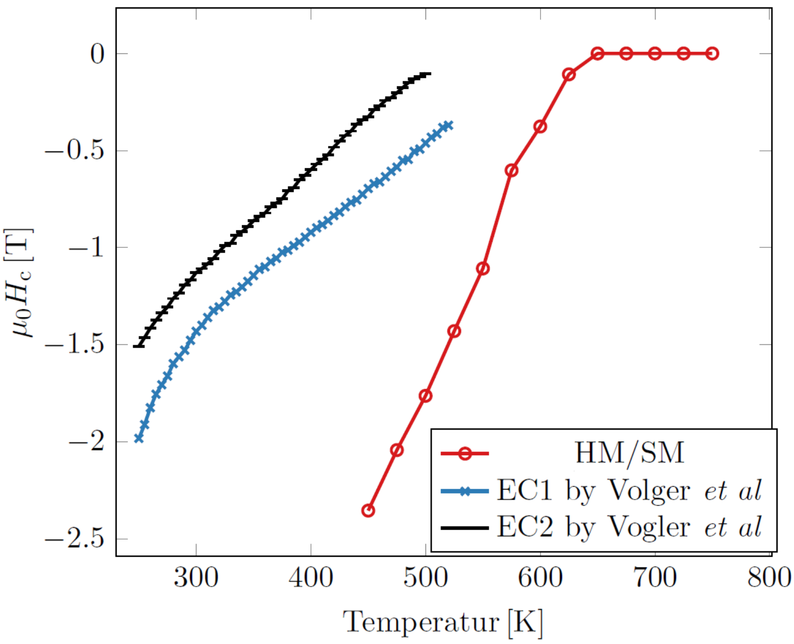

Figure 7.9: dH_c/dT gradients for the exchange coupled structures (EC1 and EC2) from the work by Vogler *et al* [93] and the bilayer structure (HM/SM) used in this work.

head designs. Analyzing the transition curvature showed that the curvature reduces only marginally even for the *Backshield*$_{200}$ design where the highest write field and field gradient can be achieved. An idea how to improve the curvature reduction is to use an exchange spring medium [46, 47, 50, 143–145]. The soft magnetic layer acts as a write assist and thus smaller write fields are required to write the grains. For the conventional design the curvature of the exchange spring recording medium is larger than that of the pure hard magnetic medium. Thus, the curvature reduction potential was expected to be higher for the exchange spring media. Switching probability phase diagrams for the different head designs in combination with the exchange spring recording media were computed. Surprisingly, the curvature reduction for the *Backshield*$_{200}$ design was even smaller than for the pure hard magnetic material. To understand why the curvature reduces only so little, the results were analyzed in the context of the effective recording time window (ERTW) model that was used in the paper by Vogler *et al* [93]. The ERTW model confirmed the results of the LLB model. Hence, it is possible to conclude that the marginal reduction of the curvature is not a consequence of noise. The analysis also pointed out that the exchange spring recording medium shows a larger potential for curvature reduction if higher field gradients are used.

In conclusion, it was not possible to see any improvement for the resulting field gradients of the optimized flipped head design in combination with pure hard magnetic and exchange spring recording media. The results showed that a simple optimization of the conventional head design is not sufficient for effective curvature reduction but that new head concepts have to be introduced to reduce transition curvature.

Chapter 8

Conclusion

To conclude, in this work challenges of heat-assisted magnetic recording that result from the elevated temperatures during the recording process were investigated. The sources that lead to temperature-dependent noise during recording were studied and suitable solutions to reduce the noise were presented. Overall, the goal was to improve the quality of the information that is written on the grains during the HAMR process.

The parameter that determines the quality of the bits is the signal-to-noise ratio. It was examined how various material and write head parameters influence the SNR. The investigation showed that for small grain sizes the SNR strongly depends on the damping constant. Together with a varying bit length, the damping constant is the key parameter to explain large SNR changes between different parameters. All the other material and write head parameters showed only a marginal influence on the SNR.

In reality, the applied heat pulse during HAMR leads to a temperature gradient within the recording material. Since this temperature gradient is a source of thermal noise, it was investigated how this temperature gradient influences the recording performance in terms of the maximum possible switching probability and the width of the transition between bits. The results showed that the behavior when assuming a temperature gradient is qualitatively similar to that when a Curie temperature gradient is considered. Moreover, it was illustrated that an artificial Curie temperature gradient within the material can compensate the performance loss due to the temperature gradient.

A critical point for the quality of the recorded information is the choice of recording material. Single phase hard magnetic recording material shows a reduced maximum switching probability and a bilayer structure consisting of 50% hard and 50% soft magnetic material with graded Curie temperature show noise that limits possible density of the recording grains. A bilayer structure was thus optimized in order to reduce these noise sources. The results showed a strong dependence of the optimal material composition on the damping constant of the hard magnetic layer. Whereas the optimized composition of the soft magnetic material was similar in all cases, the amount of soft magnetic material was strongly varying with the damping constant of the hard magnetic layer. This again shows the strong dependece of the damping constant on the recording performance.

Another challenge of HAMR results from the heat pulse. Due to the Gaussian shape of the heat pulse, the temperature contours in the recording material and thus also the transition between bits are significantly stronger curved than in perpendicular magnetic recording. This curvature is expected to reduce the quality of the read-back signal and thus the resulting SNR. Recently, a write head design with flipped write and return poles was proposed. In this design a large spatial field gradient of the write head is the key to significantly reduce the transition curvature. Thus, in this work, the write pole of a heat-assisted magnetic recording head was optimized with topology optimization in order to produce large field gradients as well as large fields in the region of the heat pulse. Locally resolved switching probability diagrams were computed and the results were compared with a qualitative model. The results showed that the gradients of the optimized head design were not sufficient to lead to any significant improvement of the written track neither for single phase hard magnetic recording material nor for the optimized bilayer structure that was determined during the optimization process of the recording material. An additional analysis showed that even higher field gradients did not lead to a curvature reduction as expected for both recording materials. Again, a strong influence of the damping constant on the possible curvature reduction could be seen.

List of Figures

List of Tables

Bibliography

[1] 10 key marketing trends for 2017 and ideas for exceeding customer expectations.

[2] John Gantz and David Reinsel. THE DIGITAL UNIVERSE IN 2020: Big Data, Bigger Digital Shadows, and Biggest Growth in the Far East. page 16, December.

[3] Gaspare Varvaro and Francesca Casoli. *Ultra-High-Density Magnetic Recording: Storage Materials and Media Designs*. CRC Press, March 2016.

[4] Remzi H Arpaci-Dusseau and Andrea C Arpaci-Dusseau. *Operating systems: Three easy pieces*, volume 1. Arpaci-Dusseau Books, 2015.

[5] Edward Grochowski and Robert D Halem. Technological impact of magnetic hard disk drives on storage systems. *IBM Systems Journal*, 42(2):338–346, 2003.

[6] Edward Grochowski and Roger F Hoyt. Future trends in hard disk drives. *IEEE transactions on Magnetics*, 32(3):1850–1854, 1996.

[7] Hard disk drive, June 2019. Page Version ID: 903433024.

[8] Dave Anderson. Hdd opportunities challenges, now to 2020, May 2013.

[9] Bruno Marchon, Thomas Pitchford, Yiao-Tee Hsia, and Sunita Gangopadhyay. The head-disk interface roadmap to an areal density of tbit/in2. *Advances in Tribology*, 2013, 2013.

[10] IBM Archives: IBM 350 disk storage unit, January 2003.

[11] Seagate reaches One Terabit per Square Inch Milestone in Hard Drive Storage with New Technology Demonstration | News Archive | Seagate UK, May 19 2012.

[12] Michael Cornwell. Anatomy of a solid-state drive. *Commun. ACM*, 55(12):59–63, 2012.

[13] Feng Chen, David A Koufaty, and Xiaodong Zhang. Understanding intrinsic characteristics and system implications of flash memory based solid state drives. In *ACM SIGMETRICS Performance Evaluation Review*, volume 37, pages 181–192. ACM, 2009.

[14] Mark H. Kryder, Edward C. Gage, Terry W. McDaniel, William A. Challener, Robert E. Rottmayer, Ganping Ju, Yiao-Tee Hsia, and M. Fatih Erden. Heat assisted magnetic recording. *Proceedings of the IEEE*, 96(11):1810–1835, 2008.

[15] Robert E. Rottmayer, Sharat Batra, Dorothea Buechel, William A. Challener, Julius Hohlfeld, Yukiko Kubota, Lei Li, Bin Lu, Christophe Mihalcea, Keith Mountfield, and others. Heat-assisted magnetic recording. *IEEE Transactions on Magnetics*, 42(10):2417–2421, 2006.

[16] W. A. Challener, Chubing Peng, A. V. Itagi, D. Karns, Wei Peng, Yingguo Peng, XiaoMin Yang, Xiaobin Zhu, N. J. Gokemeijer, Y.-T. Hsia, G. Ju, Robert E. Rottmayer, Michael A. Seigler, and E. C. Gage. Heat-assisted magnetic recording by a near-field transducer with efficient optical energy transfer. *Nature Photonics*, 3(4):220–224, April 2009.

[17] Ganping Ju, Yingguo Peng, Eric KC Chang, Yinfeng Ding, Alexander Q Wu, Xiaobin Zhu, Yukiko Kubota, Timothy J Klemmer, Hassib Amini, Li Gao, et al. High density heat-assisted magnetic recording media and advanced characterization—progress and challenges. *IEEE Transactions on Magnetics*, 51(11):1–9, 2015.

[18] L. Burns Jr Leslie and others. *Magnetic recording system.* Google Patents, December 1959.

[19] ASRC | IDEMA. http://idema.org/?cat=10.

[20] H. J. Richter, A. Y. Dobin, R. T. Lynch, D. Weller, R. M. Brockie, O. Heinonen, K. Z. Gao, J. Xue, R. J. M. v. d. Veerdonk, P. Asselin, and M. F. Erden. Recording potential of bit-patterned media. *Applied Physics Letters*, 88(22):222512, May 2006.

[21] H. J. Richter, A. Y. Dobin, O. Heinonen, K. Z. Gao, R. J. M. v d Veerdonk, R. T. Lynch, J. Xue, D. Weller, P. Asselin, M. F. Erden, and R. M. Brockie. Recording on Bit-Patterned Media at Densities of 1 Tb/in^2 and Beyond. *IEEE Transactions on Magnetics*, 42(10):2255–2260, October 2006.

[22] Bing K Yen, Jim Hennessey, Eric Freeman, Kim Yang Lee, David S Kuo, and Mark Ostrowski. Bit patterned media, August 15 2013. US Patent App. 13/835,873.

[23] Mark Re. HAMR: the Next Leap Forward is Now, October 2017.

[24] Grünberg Binasch, Peter Grünberg, F Saurenbach, and W Zinn. Enhanced magnetoresistance in layered magnetic structures with antiferromagnetic interlayer exchange. *Physical review B*, 39(7):4828, 1989.

[25] Mario Norberto Baibich, Jean Marc Broto, Albert Fert, F Nguyen Van Dau, Frédéric Petroff, P Etienne, G Creuzet, A Friederich, and J Chazelas. Giant magnetoresistance of (001) fe/(001) cr magnetic superlattices. *Physical review letters*, 61(21):2472, 1988.

[26] Dennis E. Speliotis. Magnetic recording beyond the first 100 Years. *Journal of Magnetism and Magnetic Materials*, 193(1-3):29–35, March 1999.

[27] Stanley H Charap, Pu-Ling Lu, and Yanjun He. Thermal stability of recorded information at high densities. *IEEE Transactions on Magnetics*, 33(1):978–983, 1997.

[28] CP Bean and undJ D Livingston. Superparamagnetism. *Journal of Applied Physics*, 30(4):S120–S129, 1959.

[29] H Neal Bertram and M Williams. Snr and density limit estimates: A comparison of longitudinal and perpendicular recording. *IEEE transactions on magnetics*, 36(1):4–9, 2000.

[30] Shun-ichi Iwasaki and Katsumaro Takemura. An analysis for the circular mode of magnetization in short wavelength recording. *IEEE Transactions on Magnetics*, 11(5):1173–1175, 1975.

[31] Toshiba Ships First 40gb 1.8-inch Perpendicular Magnetic Recording Drive. Accessed: 2019-06-14.

[32] S. Iwasaki. Perpendicular magnetic recording. *IEEE Transactions on Magnetics*, 16(1):71–76, January 1980.

[33] Yukiko Kubota, Dieter Weller, and Mei-Ling Wu. Soft magnetic underlayer (sul) for perpendicular recording medium, May 16 2002. US Patent App. 10/003,363.

[34] Dmitri Litvinov, Mark H Kryder, and Sakhrat Khizroev. Recording physics of perpendicular media: soft underlayers. *Journal of Magnetism and Magnetic Materials*, 232(1-2):84–90, 2001.

[35] Kai Zhong Gao, Olle Heinonen, and Yonghua Chen. Read and write processes, and head technology for perpendicular recording. *Journal of Magnetism and Magnetic Materials*, 321(6):495–507, 2009.

[36] R. F. L. Evans, Roy W. Chantrell, Ulrich Nowak, Andreas Lyberatos, and H.-J. Richter. Thermally induced error: Density limit for magnetic data storage. *Applied Physics Letters*, 100(10):102402, 2012.

[37] Hendrik F Hamann, Yves C Martin, and H Kumar Wickramasinghe. Thermally assisted recording beyond traditional limits. *Applied Physics Letters*, 84(5):810–812, 2004.

[38] M Mallary, A Torabi, and M Benakli. One terabit per square inch perpendicular recording conceptual design. *IEEE Transactions on Magnetics*, 38(4):1719–1724, 2002.

[39] Mark H Kryder and Roy W Gustafson. High-density perpendicular recording—advances, issues, and extensibility. *Journal of Magnetism and Magnetic Materials*, 287:449–458, 2005.

[40] Jian-Gang Zhu and Hai Li. Understanding signal and noise in heat assisted magnetic recording. *IEEE Transactions on Magnetics*, 49(2):765–772, 2013.

[41] J Mallinson. On extremely high density digital recording. *IEEE Transactions on Magnetics*, 10(2):368–373, 1974.

[42] Roger Wood. The feasibility of magnetic recording at 1 terabit per square inch. *IEEE Transactions on magnetics*, 36(1):36–42, 2000.

[43] K Hono, YK Takahashi, Ganping Ju, Jan-Ulrich Thiele, Antony Ajan, XiaoMin Yang, Ricardo Ruiz, and Lei Wan. Heat-assisted magnetic recording media materials. *MRS Bulletin*, 43(2):93–99, 2018.

[44] Y. Okada, H. Hoshiya, T. Okada, and M. Fuyama. Magnetic properties of FeCo multilayered films for single pole heads. *IEEE Transactions on Magnetics*, 40(4):2368–2370, July 2004.

[45] Daniel Z Bai and Jian-Gang Zhu. Micromagnetics of perpendicular write heads with extremely small pole tip dimensions. *Journal of applied physics*, 91(10):6833–6835, 2002.

[46] Dieter Suess. Micromagnetics of exchange spring media: Optimization and limits. *Journal of magnetism and magnetic materials*, 308(2):183–197, 2007.

[47] Dieter Suess, Thomas Schrefl, S. Fähler, Markus Kirschner, Gino Hrkac, Florian Dorfbauer, and Josef Fidler. Exchange spring media for perpendicular recording. *Applied Physics Letters*, 87(1):012504, 2005.

[48] D. Suess, T. Schrefl, R. Dittrich, M. Kirschner, F. Dorfbauer, G. Hrkac, and J. Fidler. Exchange spring recording media for areal densities up to 10tbit/in2. *Journal of Magnetism and Magnetic Materials*, 290-291:551–554, April 2005.

[49] D. Suess. Multilayer exchange spring media for magnetic recording. *Applied Physics Letters*, 89(11):113105, September 2006.

[50] D. Suess and T. Schrefl. Breaking the thermally induced write error in heat assisted recording by using low and high Tc materials. *Applied Physics Letters*, 102(16):162405, April 2013.

[51] Simon Greaves, Yasushi Kanai, and Hiroaki Muraoka. Shingled recording for 2–3 tbit/in˜2. *IEEE Transactions on Magnetics*, 45(10):3823–3829, 2009.

[52] Yasushi Kanai, Yoshihiro Jinbo, Toshio Tsukamoto, Simon John Greaves, Kazuetsu Yoshida, and Hiroaki Muraoka. Finite-element and micromagnetic modeling of write heads for shingled recording. *IEEE Transactions on Magnetics*, 46(3):715–721, 2010.

[53] Roger Wood, Mason Williams, Aleksandar Kavcic, and Jim Miles. The feasibility of magnetic recording at 10 terabits per square inch on conventional media. *IEEE Transactions on Magnetics*, 45(2):917–923, 2009.

[54] Kheong Sann Chan, Jim J Miles, Euiseok Hwang, BVK Vijayakumar, Jian-Gang Zhu, Wen-Chin Lin, and Rohit Negi. Tdmr platform simulations and experiments. *IEEE Transactions on Magnetics*, 45(10):3837–3843, 2009.

[55] Y Shiroishi, K Fukuda, I Tagawa, H Iwasaki, S Takenoiri, H Tanaka, H Mutoh, and N Yoshikawa. Future options for hdd storage. *IEEE Transactions on Magnetics*, 45(10):3816–3822, 2009.

[56] Jian-Gang Zhu, Xiaochun Zhu, and Yuhui Tang. Microwave assisted magnetic recording. *IEEE Transactions on Magnetics*, 44(1):125–131, 2007.

[57] Satoshi Okamoto, Nobuaki Kikuchi, Masaki Furuta, Osamu Kitakami, and Takehito Shimatsu. Microwave assisted magnetic recording technologies and related physics. *Journal of Physics D: Applied Physics*, 48(35):353001, 2015.

[58] Terumitsu Tanaka, Y Otsuka, Y Furomoto, Kimihide Matsuyama, and Yukio Nozaki. Selective magnetization switching with microwave assistance for three-dimensional magnetic recording. *Journal of Applied Physics*, 113(14):143908, 2013.

[59] Masukazu Igarashi, Masato Matsubara, Keiichi Nagasaka, and Masato Shiimoto. Spin-torque oscillator (sto) for microwave-assisted magnetic recording (mamr) and methods of use thereof, October 1 2013. US Patent 8,547,656.

[60] Christoph Vogler, Claas Abert, Florian Bruckner, Dieter Suess, and Dirk Praetorius. Areal density optimizations for heat-assisted magnetic recording of high-density media. *Journal of Applied Physics*, 119(22):223903, 2016.

[61] Tim Rausch, Jon D Trantham, Alfredo S Chu, Housan Dakroub, Jason W Riddering, Charles P Henry, James D Kiely, Edward C Gage, and John W Dykes. Hamr drive performance and integration challenges. *IEEE Transactions on Magnetics*, 49(2):730–733, 2013.

[62] G Bertero, M Alex, B Valcu, and R Eaton. Hamr recording challenges at high linear densities. In *2015 IEEE International Magnetics Conference (INTERMAG)*, pages 1–1. IEEE, 2015.

[63] William A Challener, Terry W Mcdaniel, Christophe D Mihalcea, Keith R Mountfield, Kalman Pelhos, and Ibrahim K Sendur. Light delivery techniques for heat-assisted magnetic recording. *Japanese journal of applied physics*, 42(2S):981, 2003.

[64] Nan Zhou, Xianfan Xu, Aaron T. Hammack, Barry C. Stipe, Kaizhong Gao, Werner Scholz, and Edward C. Gage. Plasmonic near-field transducer for heat-assisted magnetic recording. *Nanophotonics*, 3(3), January 2014.

[65] Jacek Gosciniak, Marcus Mooney, Mark Gubbins, and Brian Corbett. Novel droplet near-field transducer for heat-assisted magnetic recording. *Nanophotonics*, 4(1), January 2015.

[66] Michael C Kautzky and Martin G Blaber. Materials for heat-assisted magnetic recording heads. *MRS Bulletin*, 43(2):100–105, 2018.

[67] M.T. Kief and R.H. Victora. Materials for heat-assisted magnetic recording. *MRS Bulletin*, 43(02):87–92, February 2018.

[68] Kevin Arthur Gomez, William Albert Challener, Ravishankar Ajjanagadde Shivarama, and Patrick Breckow Chu. Light delivery technique for heat assisted magnetic recording head, March 18 2008. US Patent 7,345,840.

[69] AV Itagi, WA Challener, C Peng, D Karns, Y Peng, X Yang, X Zhu, N Gokemeijer, Y-T Hsia, G Ju, et al. Integrated near field transducer heat assisted magnetic recording head: Design and recording demonstration. In *2009 Optical Data Storage Topical Meeting*, pages 19–21. IEEE, 2009.

[70] Chubing Peng, Edward Charles Gage, and Yongjun Zhao. Near-field transducer, April 15 2014. US Patent 8,699,307.

[71] Michael A Seigler, William A Challener, Edward Gage, Nils Gokemeijer, Ganping Ju, Bin Lu, Kalman Pelhos, Chubing Peng, Robert E Rottmayer, Xiaomin Yang, et al. Integrated heat assisted magnetic recording head: Design and recording demonstration. *IEEE Transactions on Magnetics*, 44(1):119–124, 2007.

[72] Michael Allen Seigler, Mark William Covington, Michael Leigh Mallary, Hua Zhou, and Amit Vasant Itagi. Recording head for heat assisted magnetic recording, May 2013.

[73] Yufeng Hu and Wentao Yan. Energy assisted magnetic recording head having a near field transducer with reduced thermal protrusion, June 26 2012. US Patent 8,208,350.

[74] Dieter Weller, Gregory Parker, Oleksandr Mosendz, Eric Champion, Barry Stipe, Xiaobin Wang, Timothy Klemmer, Ganping Ju, and Antony Ajan. A hamr media technology roadmap to an areal density of 4 tb/in˜2. *IEEE transactions on magnetics*, 50(1):1–8, 2013.

[75] Dieter Weller, Oleksandr Mosendz, Gregory Parker, Simone Pisana, and Tiffany S Santos. L10 fe p t x–y media for heat-assisted magnetic recording. *physica status solidi (a)*, 210(7):1245–1260, 2013.

[76] Li Zhang, YK Takahashi, K Hono, BC Stipe, J-Y Juang, and M Grobis. L10-ordered feptag–c granular thin film for thermally assisted magnetic recording media. *Journal of Applied Physics*, 109(7):07B703, 2011.

[77] Steven D Granz and Mark H Kryder. Granular l10 fept (0 0 1) thin films for heat assisted magnetic recording. *Journal of Magnetism and Magnetic Materials*, 324(3):287–294, 2012.

[78] Hua Yuan, Alexander Chernyshov, Gerardo A Bertero, and B Ramamurthy Acharya. Low roughness heatsink design for heat assisted magnetic recording media, October 4 2012. US Patent App. 13/077,160.

[79] Chubing Peng, Edward Charles Gage, Ganping Ju, Jan-Ulrich Thiele, and Kaizhong Gao. Heat sink layer, November 5 2013. US Patent 8,576,672.

[80] Eric J Champion, Adam F Torabi, and Matthew R Gibbons. Energy assisted discrete track media with heat sink, August 21 2012. US Patent 8,247,095.

[81] Bit Patterned Media (BPM) - Helmholtz-Zentrum Dresden-Rossendorf, HZDR.

[82] Bin Lu, Dieter Weller, and Ganping Ju. Thermally isolated granular media for heat assisted magnetic recording, September 15 2005. US Patent App. 10/797,204.

[83] Thomas R Albrecht, Daniel Bedau, Elizabeth Dobisz, He Gao, Michael Grobis, Olav Hellwig, Dan Kercher, Jeffrey Lille, Ernesto Marinero, Kanaiyalal Patel, et al. Bit patterned media at 1 tdot/in 2 and beyond. *IEEE Transactions on Magnetics*, 49(2):773–778, 2013.

[84] XiaoMin Yang, Yuan Xu, Kim Lee, Shuaigang Xiao, David Kuo, and Dieter Weller. Advanced lithography for bit patterned media. *IEEE Transactions on Magnetics*, 45(2):833–838, 2009.

[85] Elizabeth A Dobisz, Zvonomir Z Bandic, Tsai-Wei Wu, and Thomas Albrecht. Patterned media: nanofabrication challenges of future disk drives. *Proceedings of the IEEE*, 96(11):1836–1846, 2008.

[86] Christoph Vogler, Claas Abert, Florian Bruckner, Dieter Suess, and Dirk Praetorius. Heat-assisted magnetic recording of bit-patterned media beyond 10 Tb/in ^{2}. *Applied Physics Letters*, 108(10):102406, March 2016.

[87] Akira Kikitsu. Prospects for bit patterned media for high-density magnetic recording. *Journal of Magnetism and Magnetic Materials*, 321(6):526–530, 2009.

[88] HJ Richter, Andreas Lyberatos, Ulrich Nowak, Richard Francis L Evans, and Roy W Chantrell. The thermodynamic limits of magnetic recording. *Journal of Applied Physics*, 111(3):033909, 2012.

[89] Dieter Suess, Christoph Vogler, Claas Abert, Florian Bruckner, Roman Windl, Leoni Breth, and J. Fidler. Fundamental limits in heat-assisted magnetic recording and methods to overcome it with exchange spring structures. *Journal of Applied Physics*, 117(16):163913, 2015.

[90] Christoph Vogler, Claas Abert, Florian Bruckner, Dieter Suess, and Dirk Praetorius. Basic noise mechanisms of heat-assisted-magnetic recording. *Journal of Applied Physics*, 120(15):153901, 2016.

[91] PAA van der Heijden, TW Clinton, and MF Erden. Effects of transition curvature on perpendicular magnetic recording performance. *Applied physics letters*, 83(21):4369–4371, 2003.

[92] M. Hashimoto, M. Salo, Y. Ikeda, A. Moser, R. Wood, and H. Muraoka. Analysis of written transition curvature in perpendicular magnetic recording from spin-stand testing. *IEEE transactions on magnetics*, 43(7):3315–3319, 2007.

[93] Christoph Vogler, Claas Abert, Florian Bruckner, and Dieter Suess. Efficiently reducing transition curvature in heat-assisted magnetic recording with state-of-the-art write heads. *Applied Physics Letters*, 110(18):182406, May 2017.

[94] J. G. J. Zhu and H. Li. Correcting Transition Curvature in Heat-Assisted Magnetic Recording. *IEEE Transactions on Magnetics*, 53(2):1–7, February 2017.

[95] W. Kohn and L. J. Sham. Quantum Density Oscillations in an Inhomogeneous Electron Gas. *Physical Review*, 137(6A):A1697–A1705, March 1965.

[96] Richard FL Evans, Weijia J. Fan, Phanwadee Chureemart, Thomas A. Ostler, Matthew OA Ellis, and Roy W. Chantrell. Atomistic spin model simulations of magnetic nanomaterials. *Journal of Physics: Condensed Matter*, 26(10):103202, 2014.

[97] Claas Abert. Micromagnetics and spintronics: Models and numerical methods. *arXiv preprint arXiv:1810.12365*, 2018.

[98] M. Lakshmanan. The fascinating world of the Landau-Lifshitz-Gilbert equation: an overview. *Philosophical Transactions of the Royal Society A: Mathematical, Physical and Engineering Sciences*, 369(1939):1280–1300, March 2011.

[99] U. Atxitia, D. Hinzke, and U. Nowak. Fundamentals and applications of the Landau–Lifshitz–Bloch equation. *Journal of Physics D: Applied Physics*, 50(3):033003, December 2016.

[100] LALE Landau. L. Landau and E. Lifshitz, Phys. Z. Sowjetunion 8, 153 (1935). *Phys. Z. Sowjetunion*, 8:153, 1935.

[101] R. Wieser. Role of quadratic terms in the Heisenberg model for quantum spin dynamics. *Physical Review B*, 84(5):054411, August 2011.

[102] Thomas L. Gilbert. A Lagrangian formulation of the gyromagnetic equation of the magnetization field. *Phys. Rev.*, 100:1243, 1955.

[103] Massimiliano d'Aquino. *Nonlinear Magnetization Dynamics in Thin-films and Nanoparticles*. PhD thesis, Università degli studi di Napoli "Federico II", 2004.

[104] W. Brown. Thermal fluctuation of fine ferromagnetic particles. *IEEE Transactions on Magnetics*, 15(5):1196–1208, September 1979.

[105] William Coffey and Yu P. Kalmykov. *The Langevin Equation: With Applications to Stochastic Problems in Physics, Chemistry and Electrical Engineering*. World Scientific, 2012. Google-Books-ID: r1K6CgAAQBAJ.

[106] José Luis García-Palacios and Francisco J. Lázaro. Langevin-dynamics study of the dynamical properties of small magnetic particles. *Physical Review B*, 58(22):14937–14958, December 1998.

[107] A. Lyberatos, D. V. Berkov, and R. W. Chantrell. A method for the numerical simulation of the thermal magnetization fluctuations in micromagnetics. *Journal of Physics: Condensed Matter*, 5(47):8911–8920, November 1993.

[108] M d'Aquino, C Serpico, G Coppola, ID Mayergoyz, and G Bertotti. Midpoint numerical technique for stochastic landau-lifshitz-gilbert dynamics. *Journal of applied physics*, 99(8):08B905, 2006.

[109] DV Berkov and NL Gorn. Thermally activated processes in magnetic systems consisting of rigid dipoles: equivalence of the ito and stratonovich stochastic calculus. *Journal of Physics: Condensed Matter*, 14(13):L281, 2002.

[110] W Moon and JS Wettlaufer. On the interpretation of stratonovich calculus. *New Journal of Physics*, 16(5):055017, 2014.

[111] Riccardo Mannella and Peter VE McClintock. Itô versus stratonovich: 30 years later. *Fluctuation and Noise Letters*, 11(01):1240010, 2012.

[112] Christoph Vogler. *Thermische Effekte in Mikromagnetimus : von ultraschnellen Schaltprozessen zu Langzeitstabilitäten*. PhD thesis, TU Wien, 2015.

[113] Szymon Peszat and Jerzy Zabczyk. Stochastic evolution equations with a spatially homogeneous wiener process. *Stochastic Processes and their Applications*, 72(2):187–204, 1997.

[114] Christoph Vogler, Claas Abert, Florian Bruckner, and Dieter Suess. Landau-Lifshitz-Bloch equation for exchange-coupled grains. *Physical Review B*, 90(21):214431, December 2014.

[115] Hai Li. Storage Physics and Noise Mechanism in Heat-Assisted Magnetic Recording. page 186, 2016.

[116] R. F. L. Evans, D. Hinzke, U. Atxitia, U. Nowak, R. W. Chantrell, and O. Chubykalo-Fesenko. Stochastic form of the Landau-Lifshitz-Bloch equation. *Physical Review B*, 85(1):014433, January 2012.

[117] D. A. Garanin. Fokker-Planck and Landau-Lifshitz-Bloch equations for classical ferromagnets. *Physical Review B*, 55(5):3050–3057, February 1997.

[118] O. Chubykalo-Fesenko, U. Nowak, R. W. Chantrell, and D. Garanin. Dynamic approach for micromagnetics close to the Curie temperature. *Physical Review B*, 74(9), September 2006.

[119] Florian Slanovc, Christoph Vogler, Olivia Muthsam, and Dieter Suess. Systematic parametrization of heat-assisted magnetic recording switching probabilities and the consequences for the resulting snr. *TBA*, TBA:TBA, 2019.

[120] Jian-Gang Jimmy Zhu and Hai Li. Medium optimization for lowering head field and heating requirements in heat-assisted magnetic recording. *IEEE Magnetics Letters*, 6:1–4, 2015.

[121] Oleg N Mryasov, Ulrich Nowak, K Yu Guslienko, and Roy W Chantrell. Temperature-dependent magnetic properties of fept: Effective spin hamiltonian model. *EPL (Europhysics Letters)*, 69(5):805, 2005.

[122] O Hovorka, S Devos, Q Coopman, WJ Fan, CJ Aas, RFL Evans, Xi Chen, G Ju, and RW Chantrell. The curie temperature distribution of fept granular magnetic recording media. *Applied Physics Letters*, 101(5):052406, 2012.

[123] Xiaobin Wang, Bogdan Valcu, and Nan-Hsiung Yeh. Transition width limit in magnetic recording. *Applied Physics Letters*, 94(20):202508, 2009.

[124] Kenichi Takano. Readback spatial sensitivity function by reciprocity principle and media readback flux. *IEEE Transactions on Magnetics*, 49(7):3818–3821, 2013.

[125] Yao Wang, MF Erden, and Randall H Victora. Novel system design for readback at 10 terabits per square inch user areal density. *IEEE Magnetics Letters*, 3, 2012.

[126] TA Roscamp, ED Boerner, and GJ Parker. Three-dimensional modeling of perpendicular reading with a soft underlayer. *Journal of applied physics*, 91(10):8366–8368, 2002.

[127] S. Hernández, P. Lu, S. Granz, P. Krivosik, P. Huang, W. Eppler, T. Rausch, and E. Gage. Using Ensemble Waveform Analysis to Compare Heat Assisted Magnetic Recording Characteristics of Modeled and Measured Signals. *IEEE Transactions on Magnetics*, 53(2):1–6, February 2017.

[128] Olivia Muthsam, Florian Slanovc, Christoph Vogler, and Dieter Suess. The superior role of the gilbert damping on the signal-to-noise ratio in heat-assisted magnetic recording. *arXiv preprint arXiv:1907.04577*, 2019.

[129] O. Muthsam, C. Vogler, and D. Suess. Noise reduction in heat-assisted magnetic recording of bit-patterned media by optimizing a high/low Tc bilayer structure. *Journal of Applied Physics*, 122(21):213903, 2017.

[130] Satoshi Iihama, Shigemi Mizukami, Nobuhito Inami, Takashi Hiratsuka, Gukcheon Kim, Hiroshi Naganuma, Mikihiko Oogane, Terunobu Miyazaki, and Yasuo Ando. Observation of Precessional Magnetization Dynamics in L10-FePt Thin Films with Different L10 Order Parameter Values. *Japanese Journal of Applied Physics*, 52(7R):073002, June 2013.

[131] Ji-Wan Kim, Hyon-Seok Song, Jae-Woo Jeong, Kyeong-Dong Lee, Jeong-Woo Sohn, Toshiyuki Shima, and Sung-Chul Shin. Ultrafast magnetization relaxation of L10-ordered Fe50pt50 alloy thin film. *Applied Physics Letters*, 98(9):092509, February 2011.

[132] W. Zhang, S. Jiang, P. K. J. Wong, L. Sun, Y. K. Wang, K. Wang, M. P. de Jong, W. G. van der Wiel, G. van der Laan, and Y. Zhai. Engineering Gilbert damping by dilute Gd doping in soft magnetic Fe thin films. *Journal of Applied Physics*, 115(17):17A308, May 2014.

[133] S. Ingvarsson, Gang Xiao, S. S. P. Parkin, and R. H. Koch. Tunable magnetization damping in transition metal ternary alloys. *Applied Physics Letters*, 85(21):4995–4997, November 2004.

[134] J. Fassbender, J. von Borany, A. Mücklich, K. Potzger, W. Möller, J. McCord, L. Schultz, and R. Mattheis. Structural and magnetic modifications of Cr-implanted Permalloy. *Physical Review B*, 73(18), May 2006.

[135] W. Bailey, P. Kabos, F. Mancoff, and S. Russek. Control of magnetization dynamics in Ni/sub 81/Fe/sub 19/ thin films through the use of rare-earth dopants. *IEEE Transactions on Magnetics*, 37(4):1749–1754, July 2001.

[136] J. O. Rantschler, R. D. McMichael, A. Castillo, A. J. Shapiro, W. F. Egelhoff, B. B. Maranville, D. Pulugurtha, A. P. Chen, and L. M. Connors. Effect of 3d, 4d, and 5d transition metal doping on damping in permalloy thin films. *Journal of Applied Physics*, 101(3):033911, February 2007.

[137] Roger W Wood, Jim Miles, and Terry Olson. Recording technologies for terabit per square inch systems. *IEEE Transactions on Magnetics*, 38(4):1711–1718, 2002.

[138] Olivia Muthsam, Christoph Vogler, and Dieter Suess. Curie temperature modulated structure to improve the performance in heat-assisted magnetic recording. *Journal of Magnetism and Magnetic Materials*, 474:442–447, 2019.

[139] Sumei Wang and R. H. Victora. Temperature distribution of granular media for heat assisted magnetic recording. *Journal of Applied Physics*, 117(17):17D147, April 2015.

[140] B. Xu, J. Yang, H. Yuan, J. Zhang, Q. Zhang, and T. C. Chong. Thermal Effects in Heat Assisted Bit Patterned Media Recording. *IEEE Transactions on Magnetics*, 45(5):2292–2295, May 2009.

[141] Douglas A Saunders, Julius Hohlfeld, Xuan Zheng, Tim Rausch, and Chris Rea. Hamr thermal gradient measurements and analysis. *IEEE Transactions on Magnetics*, 53(2):1–5, 2016.

[142] B. X. Xu, Z. J. Liu, R. Ji, Y. T. Toh, J. F. Hu, J. M. Li, J. Zhang, K. D. Ye, and C. W. Chia. Thermal issues and their effects on heat-assisted magnetic recording system (invited). *Journal of Applied Physics*, 111(7):07B701, April 2012.

[143] Jian-Ping Wang, Weikang Shen, and Jianmin Bai. Exchange coupled composite media for perpendicular magnetic recording. *IEEE transactions on magnetics*, 41(10):3181–3186, 2005.

[144] R. H. Victora and X. Shen. Exchange coupled composite media for perpendicular magnetic recording. *IEEE Transactions on Magnetics*, 41(10):2828–2833, October 2005.

[145] Kevin Robert Coffey, Jan-Ulrich Thiele, and Dieter Klaus Weller. *'Thermal spring'magnetic recording media for writing using magnetic and thermal gradients*. Google Patents, April 2005.

[146] Olivia Muthsam, Florian Slanovc, Christoph Vogler, and Dieter Suess. Improving the signal-to-noise ratio for heat-assisted magnetic recording by optimizing a high/low tc bilayer structure. *Journal of Applied Physics*, 126(12):123907, 2019.

[147] K Yu Guslienko, O Chubykalo-Fesenko, O Mryasov, R Chantrell, and D Weller. Magnetization reversal via perpendicular exchange spring in fe pt/ fe rh bilayer films. *Physical Review B*, 70(10):104405, 2004.

[148] Jian-Gang Jimmy Zhu and Hai Li. Medium optimization for lowering head field and heating requirements in heat-assisted magnetic recording. *IEEE Magnetics Letters*, 6:1–4, 2015.

[149] F. B. Hagedorn. Analysis of Exchange-Coupled Magnetic Thin Films. *Journal of Applied Physics*, 41(6):2491–2502, May 1970.

[150] O Muthsam, C Vogler, F Bruckner, and D Suess. Write head design for curvature reduction in heat-assisted magnetic recording by topology optimization. *Journal of Applied Physics*, 126(14):143906, 2019.

[151] Jian-Gang (Jimmy) Zhu and Hai Li. Write head field design for correcting transition curvature in heat assisted magnetic recording. *AIP Advances*, 7(5):056505, February 2017.

[152] Yuwei Qin, Hai Li, and Jian-Gang Zhu. Curvature-Eliminating Head Field and Track Edge Characteristics in Heat-Assisted Magnetic Recording. *IEEE Transactions on Magnetics*, 53(11):1–4, 2017.

[153] Sung-dong Suh, Young-hun Im, and Hae-Sung Kim. Heat-assisted magnetic recording head, October 2009.

[154] Myung-bok Lee and Jin-Seung Sohn. Heat assisted magnetic recording head, July 2007.

[155] Martin Philip Bendsoe and Ole Sigmund. *Topology Optimization: Theory, Methods, and Applications*. Springer Science & Business Media, April 2013. Google-Books-ID: ZCjsCAAAQBAJ.

[156] Florian Bruckner, Claas Abert, Gregor Wautischer, Christian Huber, Christoph Vogler, Michael Hinze, and Dieter Suess. Solving Large-Scale Inverse Magnetostatic Problems using the Adjoint Method. *Scientific Reports*, 7:40816, January 2017.

[157] CPO Treutler. Magnetic sensors for automotive applications. *Sensors and Actuators A: Physical*, 91(1-2):2–6, 2001.

[158] JMD Coey. Permanent magnet applications. *Journal of Magnetism and Magnetic Materials*, 248(3):441–456, 2002.

[159] Oliver Gutfleisch, Matthew A Willard, Ekkes Brück, Christina H Chen, SG Sankar, and J Ping Liu. Magnetic materials and devices for the 21st century: stronger, lighter, and more energy efficient. *Advanced materials*, 23(7):821–842, 2011.

[160] F Campelo, J Ramirez, and H Igarashi. A survey of topology optimization in electromagnetics: considerations and current trends. *Academia*, 46:2010, 2010.

[161] Pekka Neittaanmäki, Rudnicki Neittaanmaki, M Rudnicki, and A Savini. *Inverse problems and optimal design in electricity and magnetism*, volume 35. Oxford University Press, 1996.

[162] Jeonghoon Yoo and Noboru Kikuchi. Topology optimization in magnetic fields using the homogenization design method. *International Journal for Numerical Methods in Engineering*, 48(10):1463–1479, 2000.

[163] Hendrik Husstedt and Manfred Kaltenbacher. Detailed analysis of permanent magnets by means of free field measurements. *Journal of Applied Physics*, 115(17):17E302, 2014.

[164] Olivier Chadebec, J-L Coulomb, J-P Bongiraud, Gilles Cauffet, and Philippe Le Thiec. Recent improvements for solving inverse magnetostatic problem applied to thin shells. *IEEE transactions on magnetics*, 38(2):1005–1008, 2002.

[165] Christian Huber. *3D printed polymer-bonded NdFeB magnets for a tailored magnetic field*. PhD thesis, TU Wien, 2017.

[166] Todd Dupont, Johan Hoffman, Claus Johnson, Robert C. Kirby, Mats G. Larson, Anders Logg, and L. Ridgway Scott. *The fenics project*. Chalmers Finite Element Centre, Chalmers University of Technology, 2003.

[167] Martin S. Alna es, Jan Blechta, Johan Hake, August Johansson, Benjamin Kehlet, Anders Logg, Chris Richardson, Johannes Ring, Marie E. Rognes, and Garth N. Wells. The FEniCS project version 1.5. *Archive of Numerical Software*, 3(100):9–23, 2015.

[168] D Calvetti, S Morigi, L Reichel, and F Sgallari. Tikhonov regularization and the l-curve for large discrete ill-posed problems. *Journal of computational and applied mathematics*, 123(1-2):423–446, 2000.

[169] Michael Hinze, René Pinnau, Michael Ulbrich, and Stefan Ulbrich. *Optimization with PDE constraints*, volume 23. Springer Science & Business Media, 2008.

[170] Andrew M Bradley. Pde-constrained optimization and the adjoint method. 2010.

[171] S W Funke and P E Farrell. A framework for automated PDE-constrained optimisation. *ACM Transactions on Mathematical Software*, page 28.

[172] P. E. Farrell, D. A. Ham, S. W. Funke, and M. E. Rognes. Automated Derivation of the Adjoint of High-Level Transient Finite Element Programs. *SIAM Journal on Scientific Computing*, 35(4):C369–C393, January 2013.

[173] C. Huber, C. Abert, F. Bruckner, C. Pfaff, J. Kriwet, M. Groenefeld, I. Teliban, C. Vogler, and D. Suess. Topology optimized and 3d printed polymer-bonded permanent magnets for a predefined external field. *Journal of Applied Physics*, 122(5):053904, August 2017.

[174] Claas Abert, Christian Huber, Florian Bruckner, Christoph Vogler, Gregor Wautischer, and Dieter Suess. A fast finite-difference algorithm for topology optimization of permanent magnets. *Journal of Applied Physics*, 122(11):113904, 2017.

[175] Jae Seok Choi and Jeonghoon Yoo. Simultaneous structural topology optimization of electromagnetic sources and ferromagnetic materials. *Computer Methods in Applied Mechanics and Engineering*, 198(27-29):2111–2121, May 2009.

[176] Richard H. Byrd, Peihuang Lu, Jorge Nocedal, and Ciyou Zhu. A limited memory algorithm for bound constrained optimization. *SIAM Journal on Scientific Computing*, 16(5):1190–1208, 1995.

[177] Ciyou Zhu, Richard H. Byrd, Peihuang Lu, and Jorge Nocedal. Algorithm 778: L-BFGS-B: Fortran subroutines for large-scale bound-constrained optimization. *ACM Transactions on Mathematical Software (TOMS)*, 23(4):550–560, 1997.

[178] James A. Brug, Thomas C. Anthony, and Janice H. Nickel. Magnetic Recording Head Materials. *MRS Bulletin*, 21(09):23–27, September 1996.

[179] J. D. Kiely, P. M. Jones, H. Wang, R. Yang, W. Scholz, M. Benakli, J. L. Brand, and S. Gangopadhyay. Media Roughness and Head-Media Spacing in Heat-Assisted Magnetic Recording. *IEEE Transactions on Magnetics*, 50(3):132–136, March 2014.

[180] Claas Abert, Lukas Exl, Florian Bruckner, André Drews, and Dieter Suess. magnum.fe: A micromagnetic finite-element simulation code based on FEniCS. *Journal of Magnetism and Magnetic Materials*, 345:29–35, November 2013.

[181] Hendrik F Hamann, Prakash Kasiraj, Jeffrey S Lille, Yves C Martin, Chie Ching Poon, Neil Leslie Robertson, Jan-Ulrich Thiele, and Hemantha Kumar Wickramasinghe. Heating device and magnetic recording head for thermally-assisted recording, August 28 2007. US Patent 7,262,936.

[182] Pin-Wei Huang and Randall H Victora. Heat assisted magnetic recording: Grain size dependency, enhanced damping, and a simulation/experiment comparison. *Journal of Applied Physics*, 115(17):17B710, 2014.

[183] Hiroshi Kobayashi, Motoharu Tanaka, Hajime Machida, Takashi Yano, and Uee Myong Hwang. *Thermomagnetic recording*. Google Patents, August 1984.

[184] C. Mee and G. Fan. A proposed beam-addressable memory. *IEEE Transactions on Magnetics*, 3(1):72–76, 1967.

[185] G. W. Lewicki and others. *Thermomagnetic recording and magneto-optic playback system*. Google Patents, December 1971.

[186] Simon Greaves, Yoshihiro Jinbo, Yasushi Kanai, and Hiroaki Muraoka. Split-pole write head for thermally assisted magnetic recording. *IEEE Transactions on Magnetics*, 47(10):2375–2378, 2011.

[187] Simon John Greaves, R Itagaki, and Yasushi Kanai. A model for predicting transition curvature in heat-assisted magnetic recording. *IEEE Transactions on Magnetics*, 2019.

[188] DR Fredkin and TR Koehler. Hybrid method for computing demagnetizing fields. *IEEE Transactions on Magnetics*, 26(2):415–417, 1990.

[189] Martin P Bendsøe. *Topology optimization*. Springer, 2009.